

APPROCHE MULTI-ÉCHELLE DE LA
FORMATION ET L'ÉVOLUTION DES AMAS
D'ÉTOILE

Julien Dorval

A thesis submitted for the degree of Doctor of
Philosophy

May 2014

Objective and structure of this thesis

In this work, I present a new model for N-body simulations of young substructured star clusters, the Hubble-Lemaître fragmentation. This model is based on an adiabatic expansion and fragmentation of an homogeneous system, which spontaneously develop clumps from initial over-densities. I will show this model recovers characteristics from hydrodynamical simulations of star formation, which are much more computationally expansive. The structure of the Hubble-Lemaître model will be investigated, then applied to the study of the relaxation of young substructured clusters relaxation, as well as the evolution of binary populations in the same objects.

The thesis is organised as follow. An historical foreword recalls the intellectual and technological development that led to the current state of numerical astrophysics. An introduction presents the scientific context of the thesis, and the motivations for a new model.

The first part, subdivided in three chapter, introduces the Hubble-Lemaître model itself, first with an analytical approach, then from the numerical point of view. The structural aspects of the model are investigated and compared to hydrodynamical simulations. Then, the fragmented system is used as initial conditions to study the violent relaxation of substructured cluster, comparing it to the collapse of uniform cold models.

The second part, in two chapters, focuses on binary populations. A new binary detection algorithm is presented and its free parameter is calibrated. The spontaneous binaries arising during the Hubble-Lemaître expansion are characterised, then completed to resembles observed populations. We follow the evolution of the obtained population during the collapse of the fragmented system, assessing the effect of initial stellar density on binaries.

Finally, I present the various paths of research opened up by the Hubble-Lemaître model: anisotropic expansion, mock observation with dust extinction, coupling with galactic-scale simulations. I conclude the thesis by recalling the initial context and summarising the results.

Relevant material that is not necessary to follow the thesis is presented in various appendices.

Contents

Historical foreword: from Aristotle to GPU computing	1
1 Introduction	9
1.1 What is a star cluster ?	12
1.2 Some important dynamical concepts	14
1.2.1 Virial theorem	14
1.2.2 Dynamical timescales	15
1.2.3 Static models	16
1.3 The origin of star clusters	17
1.3.1 From gas to stars	17
1.3.2 Substructure and early dynamical evolution	19
1.3.3 Star formation efficiency and infant mortality	20
1.4 Simulating star clusters evolution	22
1.4.1 Hydrodynamical simulations	22
1.4.2 Artificial substructure	23
I The fragmented model and its evolution	27
2 The Hubble-Lemaître fragmented model: analytical approach	29
2.1 How to build a Hubble-Lemaître model	30
2.1.1 Initial state	30
2.1.2 Fragmentation	31
2.2 The growth of overdensities: analytical study	33
2.2.1 Working equations	33
2.2.2 Linear density perturbation	34
2.2.3 Consistent initial conditions	36
2.2.4 Segregation time-scale	37
2.2.5 Example with $N = 15000$	40
2.3 Concluding remarks	40
3 Nbody application	41
3.1 Numerical tools	41
3.1.1 Hénon units	41
3.1.2 NBODY6	43
3.1.3 StarFiddle, an N-body API	43
3.1.4 Clump finding algorithm	45
3.2 Clump mass function	48
3.2.1 Influence of H and N	48
3.2.2 Influence of stellar mass function	52
3.3 Clump contents	54
3.3.1 The velocity field	55

3.3.2	The stellar mass function in clumps	56
3.3.3	Mass segregation	59
3.4	Concluding remarks	60
4	Collapse and dynamical evolution	63
4.1	The simulations	63
4.1.1	Description of the models	63
4.1.2	Scaling to physical units	64
4.1.3	Removal of the ejected stars	65
4.2	Collapse and virialisation	66
4.3	Global mass segregation	68
4.4	Concluding remarks	72
II	Binary stars in substructured clusters	75
5	Introduction to binaries	77
5.1	What is a binary star ?	77
5.2	Multiplicity fraction	78
5.3	Observed population	79
5.4	Simulate binary populations in clusters	80
6	Detecting and injecting binaries	83
6.1	A new binary detection algorithm	83
6.1.1	Density comparison	83
6.1.2	Choosing a density ratio	84
6.2	The spontaneous binary population	86
6.2.1	Binary fraction vs primary mass	88
6.2.2	Spontaneous semi-major axis distribution	89
6.2.3	Completing the population	90
7	The evolution of the binary population	93
7.1	Results	94
7.1.1	Total binary fraction	94
7.1.2	Binary fraction vs primary mass	96
7.1.3	Semi-major axis distributions	98
7.1.4	Tidal shocks	100
7.2	Extreme tight- and wide binaries	101
7.2.1	Tight binaries	101
7.2.2	Wide binaries	104
III	Perspectives and conclusions	107
8	Perspectives	109
8.1	Tidal field	109
8.2	Stellar evolution	110
8.3	Anisotropic expansion	110

A	NBODY6	125
A.1	Block time-step	125
A.2	KS-regularization	125
A.3	Hermite integration scheme	127
A.4	Ahmad-Cohen neighbour scheme	128
B	Binary completion algorithm	131
B.1	”Theoretical” population	131
B.2	Injected and effective population	132
B.3	Stable spontaneous	133
B.4	Random pairing	134

Historical foreword: from Aristotle to GPU computing

Physics was not built in a day. In this foreword, I attempted a summary of the intellectual development that led us to our current state of knowledge. I did my best to honour the brilliant minds that made all of this possible. However, as everything in life, it should be taken with caution and a critical mind. I learned a lot researching for this, I'm sure you will too if you decide to dig further.

Motion

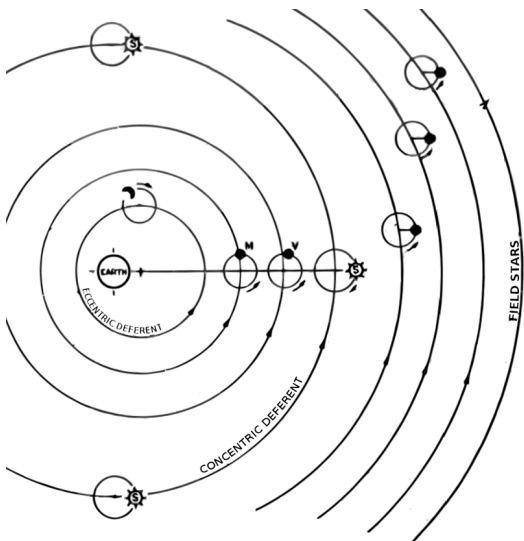
For two thousand years, Aristote physics dominated European philosophy. Rocks fell to the ground because they wanted to join their element, objects in the sky were attached to eternal rotating crystal spheres, and motion was either natural or violent, the latter needing a continuous force to exist. As the importance of projectiles grew in middle-age warfare, some improvement were made to explain trajectories, such as the impetus, a "contained source of motion" imprinted to a projectile by the thrower. Introduced by Philopon in the 6th century and relayed by Avicenne in the 11th century, it was properly formalized by Jean Buridan in the 14th century in his "Questions on Aristotle's Metaphysics". Buridan's impetus had a lot in common with momentum, in that it was proportionnal to mass and velocity. However, it could be circular, as shown by this description of celestial motion from Buridan ([Clagett, 1959](#)):

God, when He created the world, moved each of the celestial orbs as He pleased, and in moving them he impressed in them impetuses which moved them without his having to move them any more...And those impetuses which he impressed in the celestial bodies were not decreased or corrupted afterwards, because there was no inclination of the celestial bodies for other movements. Nor was there resistance which would be corruptive or repressive of that impetus.

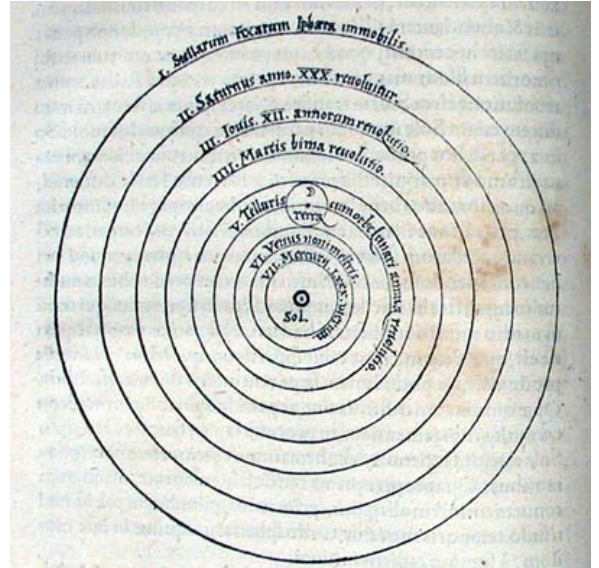
Despite the conceptual mistake of a circular momentum, Buridan, with this text, is the first to include the motion of celestial bodies in the same framework used for everyday, terrestrial motion. The impetus is not a good model, but it is a model for everything in the universe. No more eternal crystal spheres, everything in the universe must obey the same laws. Scientific revolutions do not happen in a vacuum: Buridan and others paved the way for the intellectual landslide of the 16th and 17th century.

Geocentrism and heliocentrism

While the concept of motion was slowly being refined, our vision of the universe was undergoing some faster changes. The dominant system in Europe since 150AD was the Ptolemaic geocentric model: the Sun and planets went around the Earth, following convoluted trajectories made of circles within circles called epicycles. Though complex, this system was consistent with Aristotle principles of celestial spheres and was accurate to a reasonable extent. Some alternate geocentric



(a) Ptolemy geocentric system



(b) Copernic heliocentric system

Figure 1: (a): depiction of the Ptolemaic geocentric system, the equant is not shown. (b): Copernicus illustration of his own heliocentric system, from *De revolutionibus*.

models were proposed by arab astronomers, such as Nasir ad-Din at-Tusi and Ibn al-Shatir, as well as rejected attempts to heliocentric models.

Nicolaus Copernicus studied astronomy in Cracow and Bologna, under the influence of harsh critics of the ptolemaic system. Strangely, this criticism was not fuelled by observations, but by astrology. Astronomy and astrology were closely intertwined, and the chaotic structure of the ptolemaic system made astrological considerations complicated (Barker et al., 2014). In a quest for consistency and simplicity, Copernicus proposed his heliocentric system, published in *De revolutionibus orbium coelestium* in 1543, the year of his death, in which all planets went around the sun, in the correct order. However, clinging to circular orbits, Copernicus had to preserve ptolemaic workarounds such as epicycles (not shown on Fig 1b).

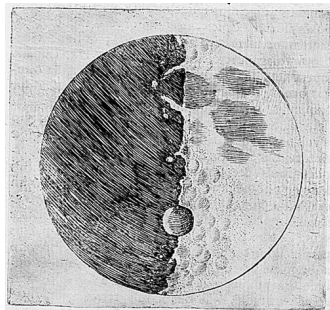
The astronomical evidence was, at the time, paradoxically against him. The apparent size changes of planets could not be measured yet, as well as stellar parallaxes, contradicting heliocentrism. The idea of a moving Earth implied some effect on falling bodies (known today as Coriolis effect) which were also not measurable at the time. Building on this apparent counter-evidence and on the work of indian astronomer Nilakantha Somayaji, Tycho Brahe, the most renowned astronomer of his time, proposed an alternative model known as the Tychonic system in the late 16th century (Ramasubramanian, 1998). Brahe maintained the Earth as the center of the universe, circled by the sun, itself orbited by all other planets. The system was very efficient and was quickly adopted by the Church and considered in compliance with the Holy Scriptures.

However, the seed of heliocentrism was planted in European scientific minds. The idea exalted the impetuous and visionary Giordano Bruno, who pushed the decentralization of Earth to the extreme, claiming stars were other suns, harbouring other planets, which themselves could sustain intelligent life. For this, his rejection of catholic dogma and his vehement refusal of retraction, Bruno was burned at the stake on the Campo de Fiori in 1600. Bruno, the fiery dialectist, despised geometry and believed the mind alone could unravel any mystery.

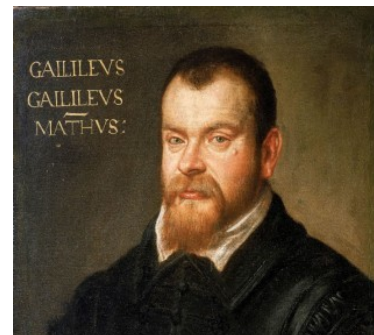
Johanes Kepler believed in geometry, in consistency and in observations. Ardent supporter of copernicism, he convinced Tycho Brahe to grant him access to his astronomical data, unsurpassed at the time. Focusing on the motion of Mars, Kepler, through trial and error, found out the planet was moving around the Sun following an ellipse. He formulated his first two laws of planetary motions. Further exploration led him to the third law. The three laws of Kepler of

20. Febr.	1610
marth. 12	O **
30. mone	** O *
2. xbn:	O *** *
3. mone	O * *
3. Ho. r.	* O *
4. mone	* O **

(a) Jupiter satellites



(b) Half-moon



(c) Galileo (1605)

Figure 2: (a) and (b): drawings by the hand of Galileo of his astronomical observations.

planetary motion were formulated, initiating the mathematisation of astronomy. They are:

Law I : All planets orbits are ellipses, with the Sun at one focus.

Law II: The line connecting a planet and the Sun sweeps out equal areas in equal amounts of times as the planet follow its orbit.

Law III: The squared orbital period of a planet is proportional to the cubed semi-major axis of its orbit.

The Starry Messenger

The father of modern astronomy, and precursor of modern science, Galileo Galilei was born in Pisa in 1564. For the first part of his scientific career, Galileo got famous for his lectures on mechanics and motion. Building on Buridan and Oresme's ideas, he expressed the mathematical form of free fall motion $d = \frac{gt^2}{2}$. Galileo also formulated what was essentially the future first law of motion from Newton.

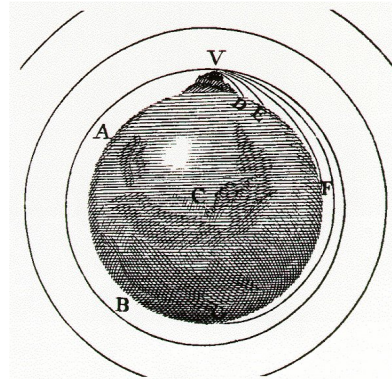
In 1609, his passion for scientific instruments led Galileo to build his own "dutch perspective glass", or telescope, a pioneering optical device from the Netherlands. Once pointed at the sky, the device triggered an avalanche of observations which would forever bury the aristotelian view of perfect and unchanged heavens. Moving Jupiter satellites, Moon craters and mountains, millions of stars in the Milky Way, these were consigned into *Sidereus Nuncius* (Starry messenger), the first scientific publication of astronomical observations ([Galileo, 1610](#)).

Strong advocate of copernic平, but lacking proper evidence, Galileo caused a large controversy with his *Dialogue Concerning the Two Chief World Systems* published in 1632, a pamphlet against the ptolemaic system, presenting (arguably unintentionally) one of its advocates as a simpleton. Despite his friendship with the pope, he had to retract his work and reject copernicism. Galileo spent the rest of his life under house arrest. Observational evidence at the time was still on the side of geocentrism. However, the extent of the backslash against Galileo showed the agitation of a Church having absorbed Ptolemy and Aristotle principles into its doctrine, in a time seeing the debate shift from theology to physics and observations.

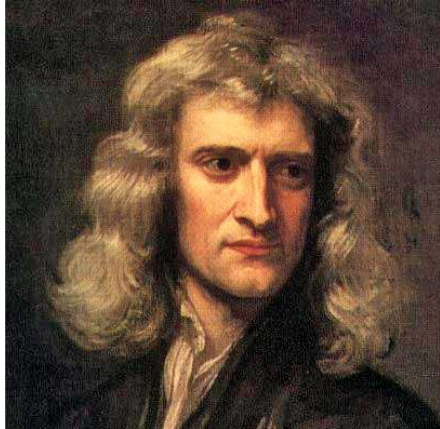
The relativity of motion is often attributed to Galileo, as he includes it in his controversial pamphlet, stating that a traveller inside a ship sailing smoothly would not be able to tell he's moving. Thus, people could be standing on a moving Earth without feeling it. However, this thought experiment was nothing new at the time and had been a recurring theme of mechanical philosophy since Buridan. Oresme, Copernicus and Bruno had been building on the idea, expanding and improving it, developing over the centuries an implicit understanding of inertia, until Bruno actually gives it a name: *virtù*. Galileo may have met Bruno himself, and had surely been influenced by his writings ([De Angelis & Santo, 2015](#)). Galileo's formulation was clearer,



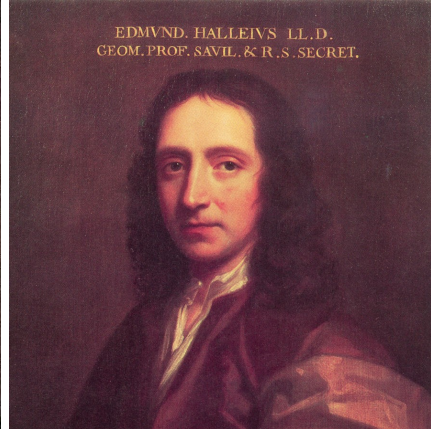
(a) "Not quite Newton's tree"



(b) Drawing from the *Principia*



(c) Isaac Newton (1689)



(d) Edmund Halley (1686)

Figure 3: (a) a supposedly descendant from Newton's apple tree in Cambridge. The drawing in (b) illustrates the common mechanics of cannonballs and satellites.

and part of a larger understanding of motion, introducing the concept of reference frame. After Copernicus decentralized the Earth, Galileo decentralized human subjectivity itself, setting the scene for the revolution to come.

On the shoulders of giants

Isaac Newton is without a doubt the father of modern mathematical science. Admitted in Cambridge in 1661, Newton supplemented the -still- official aristotelian teaching with more modern authors: Copernicus, Galileo, Kepler, and most of all, Descartes. The french philosopher had a profound impact on the young student, rooting his love for mathematics and deductive reasoning. However, while Descartes showed disdain for experimentation, Newton was an acute observer of the natural world.

In 1666, while in his mother's farm, having been forced out of Cambridge by the Plague, Newton began his reflection on the motion of celestial bodies. He derived from Kepler's law that the Sun had to exert an inverse squared distance attraction on the planets. Extending the concept to the Earth, moon, and a famous apple, Newton found a way to verify his hypothesis, using data from Galileo mechanical studies on the strength of Earth attraction. The wrong estimate of Earth radius he used at the time introduced a discrepancy which put the young man off his *gravitas* studies for 18 years.

Edmund Halley, astronomer and friend of Newton, having heard of Newton inverse squared law, urged him in 1684 to communicate his work to the Royal Society. With a new accurate measure of Earth radius and confronted to a concurrent claim to his law from Robert Hooke

(Kramer, 1982), Newton capitulated to Halley's eager enthusiasm and communicated his work in the famous *Philosophi Naturalis Principia Mathematica* (Newton, 1687). Published at Halley's own expense, the Principia shook all of Europe. Newton had invented Calculus (in parallel of Leibniz) and applied it to derive the universal law of Gravitation.

$$F = G \frac{m_1 \cdot m_2}{r^2} \quad (1)$$

Where:

- F Gravitational attraction between object 1 and object 2
- G Gravitational constant, $6.67408 \cdot 10^{-11} m^3 kg^{-1} s^{-2}$ (Pavese, 2015)
- m_i Masses of object 1 and 2
- r Distance between object 1 and 2

Though Newton was part of continuous line of geniuses and innovative minds building from each others, as he puts it "If I have seen further it is by standing on the shoulders of giants" (Maury, 1992), his input was truly revolutionary. He made large advances in optics and mathematics, and created a consistent mathematical framework to compute motions, essentially founding modern science and sowing the seeds of the industrial revolution. This framework is summed up by Newton's three laws of motion (from recent translation Cohen I. B. 1999):

Law I : Every body persists in its state of being at rest or of moving uniformly straight forward, except insofar as it is compelled to change its state by force impressed.

Law II: The alteration of motion is ever proportional to the motive force impress'd; and is made in the direction of the right line in which that force is impress'd.

Law III: To every action there is always opposed an equal reaction: or the mutual actions of two bodies upon each other are always equal, and directed to contrary parts.

The second law can be mathematically formulated in more modern terms:

$$\sum \mathbf{F} = \frac{d\mathbf{p}}{dt} \quad (2)$$

Meaning the sum of all forces \mathbf{F} applied to an object is equal to the time derivative of its momentum $\mathbf{p} = m \cdot \mathbf{v}$.

The N=3 body problem

As the Enlightenment brought a scientific revolution in many fields, I will now limit the discussion to the development of celestial mechanics, while acknowledging input from other fields.

While the two-body problem had been solved by Newton and expanded by Bernoulli in 1710 (Barrow-Green, 1997), in the 18th century the three-body problem remained the object of much investigation and development. A general solution for the Earth-Moon-Sun system would have had applications on nautical astronomy and trans-continental navigation. Extended analytical work by d'Alembert, Clairaut, Euler and Lagrange led to the development of early families of approximate solutions or exact solutions to special cases.

From 1773 to 1793, Joseph-Louis Lagrange, helped by his invention of Lagrangian mechanics, would make a lot of advances on the three-body problem. He introduced the concept of potential and discovered libration points (later known as Lagrange points). In the same time, Pierre-Simon de Laplace proved the stability of the solar system using a newly developed perturbation theory. The solar system dynamics were being unraveled, with finely tuned perturbation computation, but the general three-body problem remained unsolved.



(a) Charles Messier (1770)



(b) Henri Poincaré (1887)

Figure 4: The observer and the theorist, a century apart.

In 1888, Henri Poincaré, a renowned mathematician, submitted an entry to a contest sponsored by the King of Sweden Oskar II. The goal was to determine a usable solution to the N-body problem, for any given N. While Poincaré does not submit a complete solution, he wins the contest by presenting an in-depth exploration of the phase-space of the restricted three-body problem, which would later give rise to Chaos theory, see [Yoccoz \(2010\)](#). Poincaré managed to prove that the three-body problem had no solution involving simple functions.

Contrary to popular belief, the three-body problem *has* a solution, it was derived by Karl F. Sundman in 1912 ([Sundman, 1912](#)). However, any attempt to obtain accurate trajectory predictions would face an enormous convergence time, making the solution unusable in practice ([Belorizky, 1930](#)).

It is interesting to note that Elis Strömgren performed by-hand calculation of a three-body system, see [Aarseth \(2003b\)](#); [Strömgren \(1909\)](#), prefiguring the advent of numerical orbit computation.

The $N > 3$ body problem

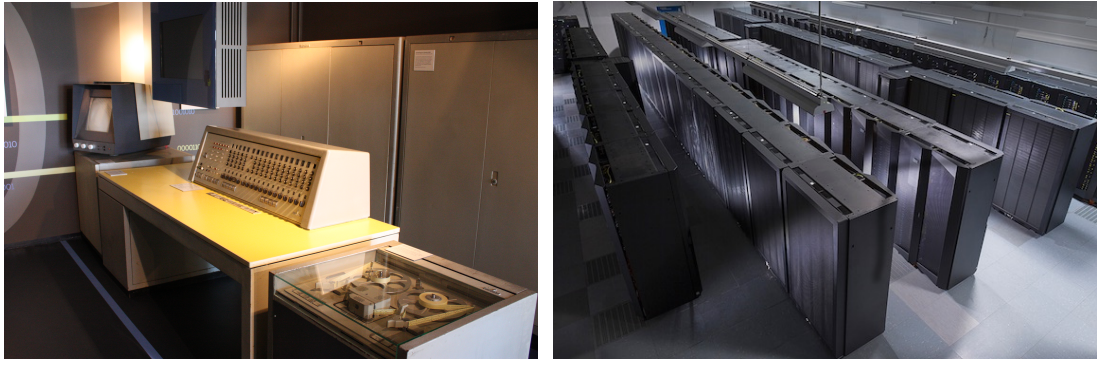
”The Sun attracts Jupiter and the other planets, Jupiter attracts its satellites and similarly the satellites act on one another.”

By this sentence from the *Principia*, Newton formulates the N-body gravitational problem, an arbitrary number of massive bodies all interacting gravitationally, for the solar system. The “ $N > 3$ -body” problem didn’t receive a lot of attention at first, as the unruly three-body problem was on everyone’s mind, and a higher-N problem seemed abstract, the solar system example being appropriately dealt in approximations.

In 1764, Charles Messier resolved individual stars in Messier 4, a globular cluster, hundreds of thousands of stars grouped together. Many new clusters were to be found afterwards, extending the catalog of real-life N-body systems. However, nothing was known of their kinematics, the stars were, in a sense, suspended motionless in the sky. This was the case until the advent of Doppler spectroscopy, which allowed astronomer to measure stars velocities ([Doppler, 1842](#)). Stellar dynamics had begun.

The $N > 3$ -body problem was still inaccessible, so scientists like James Jeans and Arthur Eddington decided to take the problem from the other hand, and took advantage of the large number of stars. Inspired by [Poincaré \(1906\)](#), both astronomers applied the statistical theory of gas to stellar systems, founding the field of stellar dynamics ([Jeans, 1916](#); [Eddington, 1916](#)).

An interesting experiment was conducted by [Holmberg \(1941\)](#) to understand the collision of two stellar systems (galaxies). With too few points to warrant a statistical approach, and before



(a) Siemens 2002

(b) Hydra supercomputer

Figure 5: The Siemens 2002, seen here on (a) at the computer museum in Kiel, could perform 2000 operations a second. The Hydra cluster, on (b), at the Max Planck Computing & Data Facility in Garching is made of 83,000 cores and 676 GPUs for a total of 10^{15} operations per seconds, a billion millions.

the rise of numerical integration, Holmberg modelled two galaxies with dozens of lightbulbs and photocells, measuring the attractive force with the amount of light received in each direction, taking advantage of the inverse squared fall of luminosity with distance, akin to gravity.

The numerical age

The first numerical N-body computations were performed by Sebastian Von Hoerner in 1959 when visiting the University of Tübingen, on a Siemens 2002, a cutting edge calculator at the time (Fig 5a). The very first had $N=4$. Then, Von Hoerner, back in Heidelberg, worked his way up to 16 stars, then 25, programming and debugging on punch cards. This story was told by Von Hoerner himself in [von Hoerner \(2001\)](#). He very quickly realized the importance of binary stars and their impact on computations. He was also able to confirm some theoretical prediction on cluster dynamics, and found a cuspy radial density profile([von Hoerner, 1960, 1963](#)).

There were two ways to increase the number of stars in simulations: buy a better computer or improve the algorithm. Sverre Johannes Aarseth got invested in the second path, which would take over his scientific life. Aarseth pioneered the use of individual time-step, changing the rate of particle positions update, gravitational softening (allowing convergence for close approaches), and polynomial predictions for force calculations ([Aarseth & Hoyle, 1964](#)). As power and optimization grew, investigations expanded, such as the interaction star-gas ([van Albada, 1968b](#)) and binary formation ([van Albada, 1968a](#)).

The 1970s brought two new important optimisation methods: KS regularization of close pairs ([Aarseth, 1972](#)) or 3-body systems ([Aarseth & Zare, 1974](#)) and Ahmad-Cohen neighbour scheme ([Ahmad & Cohen, 1973](#)). The number of stars in simulations kept growing, reaching 1000 with [Terlevich \(1980\)](#) and materializing into the *NBODY5* integrator. At this point various methods departing from a pure collisional calculation began to emerge, such as the simplified distant interaction with the [Barnes & Hut \(1986\)](#) tree algorithm.

To go beyond the regular improvement of computing power with time, a group of Japanese researchers, among whom Junichiro Makino, designed and built special purpose hardware for many-body problems: GRAPE ([Ebisuzaki et al., 1990; Ito et al., 1991](#)). These cards vastly improved the speed of N-body simulations and were a milestone on the road to the parallelization of computing. With the force calculation directly implemented in the hardware, GRAPE dominated the field for 15 years.

The latest technological leap in N-body simulations came from graphic cards, see [Bédorf & Portegies Zwart \(2012\)](#) for a more detailed historical perspective. Graphical Processing Units, or

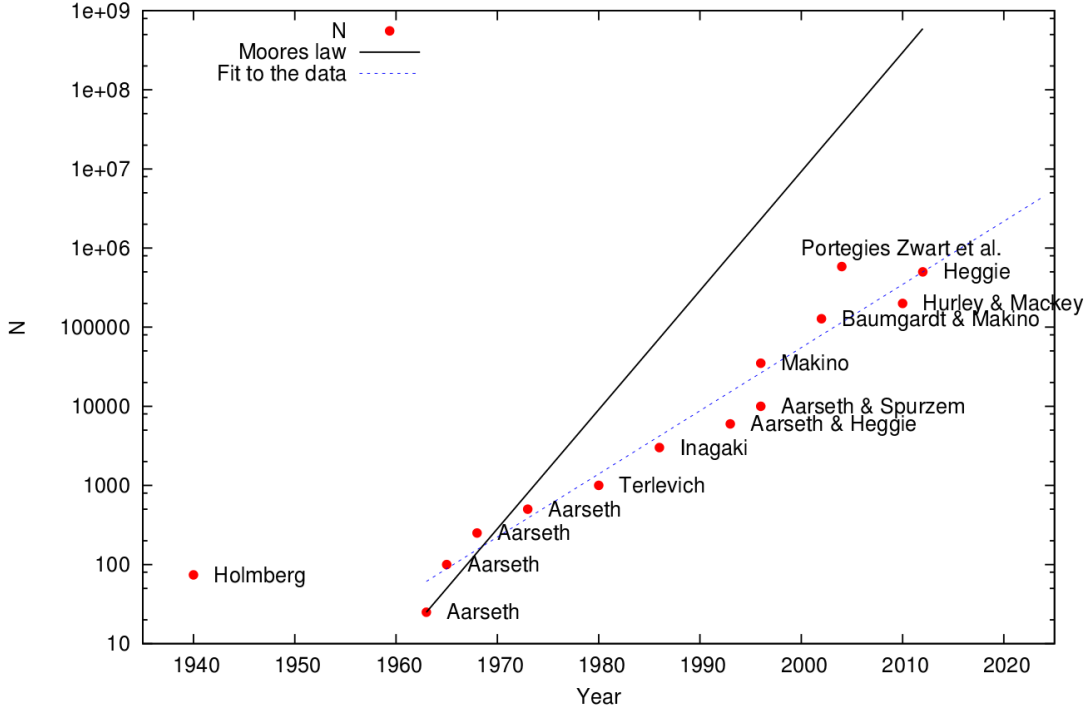


Figure 6: The evolution of the number of particles in N-body simulations. Solid line shows the Moore law. The figure was taken from [Bédorf & Portegies Zwart \(2012\)](#).

GPU, were originally designed for computer games visual rendering, applying the same transformations to a lot of pixels at the same time. These made them very efficient parallel computing machines for physics. Interest in GPU computing started to grow in the 2000s ([Nyland, Harris & Prins, 2004](#); [Elsen et al., 2006](#); [Portegies Zwart, Belleman & Geldof, 2007](#)) until the advent of usable GPU programming languages, like CUDA, in the late 2000s. At this point GPU were more efficient than GRAPE hardware for force calculation. Keigo Nitadori and Sverre Aarseth developed a GPU-accelerated version of NBODY6 in 2012 ([Nitadori & Aarseth, 2012](#)). A new iteration of the NBODY family, NBODY7, was also developed to include post-newtonian effects from General Relativity ([Aarseth, 2012](#)).

This year, 330 years after the publication of the *Principia*, [Wang et al. \(2016\)](#) performed several collisional nbody simulations of one million stars with a modified version of NBODY6 running on GPUs, on the Hydra supercomputer (Fig 5b). Computers have made it possible for humans to study systems of incredible scales in space and time, only using the universal law of gravitation. N-body numerical integrators are the culmination of centuries of scientific development on the motion of massive bodies.

CHAPTER 1

Introduction

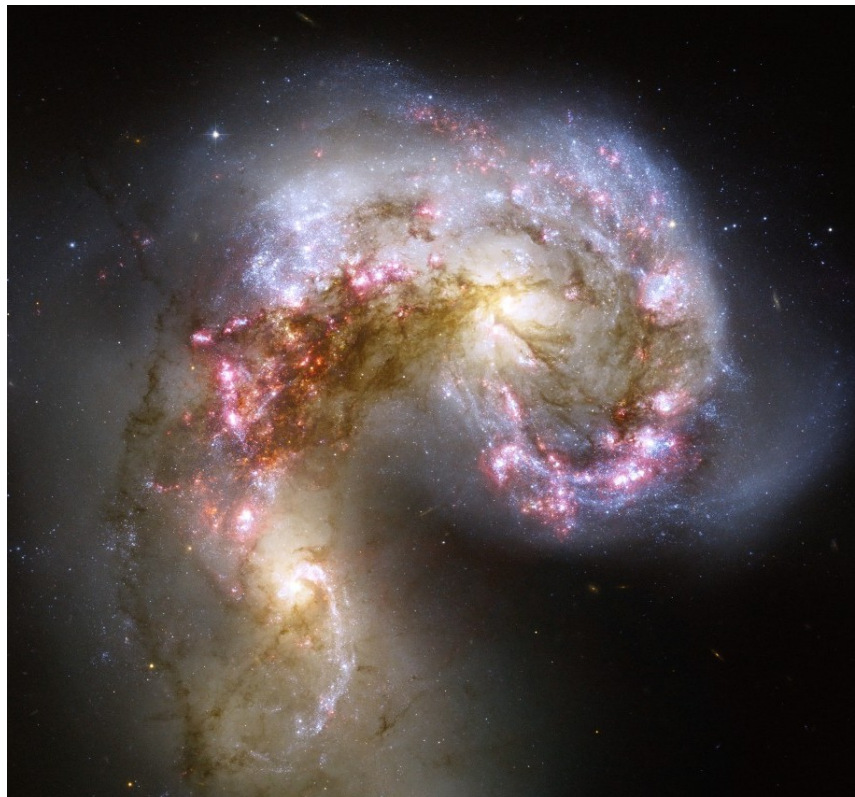


Figure 1.1: Composite picture (visible and infrared) of the merging Antennae galaxies (NGC 4038 and 4039). Very active star forming regions are seen in infrared as the gas is heated by newborn stars. Bright blue points are the hot OB stars found in the numerous Young Massive Clusters (**YMCs**) in the system. *Credits: NASA, ESA, and B. Whitmore (STScI).*

Globular Clusters(**GCs**) have long been and still are considered invaluable witnesses of galaxy formation, given their old age and bond with their host galaxies. Observations of the GC specific frequency, the amount of GCs per galactic luminosity, showed elliptical galaxies harboured proportionally more globular clusters than spirals, see the review by [Harris \(1991\)](#). As elliptical are spiral-merger products, this pointed at merger events triggering episodes of globular cluster formations ([Ashman & Zepf, 1992](#)).

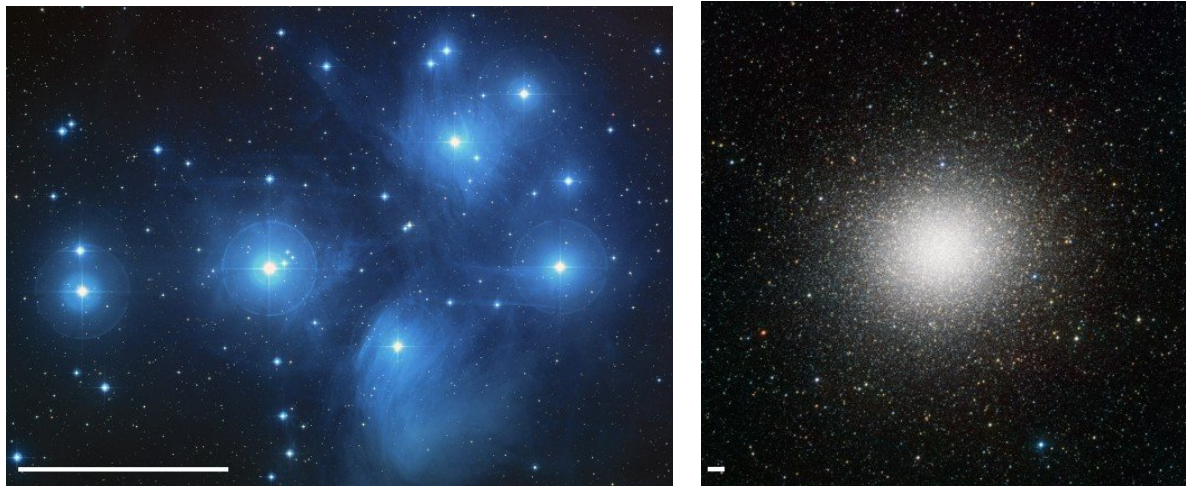
The relation between GC populations and galaxy formation history was strengthened and made more complex by the wealth of new observations brought by the advent of the Hubble Telescope. First, Young Massive Clusters, considered to be young globular clusters, were found in merging galaxies such as the Antennas ([Whitmore & Schweizer, 1995](#)). Then, cluster population around galaxies were observed to be bimodal: an extended, metal-poor blue population and a more concentrated, metal-rich red population ([Zepf & Ashman, 1993](#); [Geisler, Lee & Kim, 1996](#)). These clearly had different chemical and dynamical origins. Several hypothesis have been put forward to explain this puzzling observation: some advocated for the red population being created in merger events, others put forward the collection of blue clusters through accretion of dwarf galaxies, and others defended two distinct in-situ formation events in the galaxy, see the review by [Brodie & Strader \(2006\)](#).

While this question remains unsettled, it is clear that understanding the formation of globular clusters is key to understand their link with the galaxy formation history. 10 years ago, a new observation brought even more complexity to our picture of cluster formation. Globular clusters had long been thought to be homogeneous single-age, single-metallicities, stellar populations. Yet, a study by [Piotto et al. \(2007\)](#) showed the globular cluster NGC 2808 contained at least three different stellar sequences. Many other GCs has been shown to contain multiple populations. As this cannot be explained by the natural age spread arising from a continuous star formation at the birth clusters, such observations have far-reaching implications on their formation scenario.

A possible explanation is that globular clusters formed through the merging of smaller sub-clusters. These subclusters could have different metallicities, or possibly different ages, as a chain of successive, sequentially triggered star formation events could end up in the same cluster through merging. This picture is backed up by the most recent observations of star-forming regions in the Milky Way, showing a deeply substructured Inter-Stellar Medium (**ISM**) and star formation. That massive clusters form from merging of smaller fragmented have a strong influence of their survival rate to gas expulsion and their degree of primordial mass segregation. This in turn can affect our understanding of the ties between GC formation and galactic mergers, as the mass estimates of Young Massive Clusters in the Antennas hinge on their possible primordial mass segregation ([McCrady, Graham & Vacca, 2005](#)).

The dynamics of sub-clusters merging to form more massive systems emerged as a crucial aspect of cluster formation, and consequentially of our understanding of galaxy formation history. Hydrodynamical simulations of star cluster formation are computationally limited and can only address this issue at small scales. This work aims at circumventing this limitation through the creation of large-scale, dynamically consistent substructured initial conditions for cluster simulations, unveiling the dynamical behaviour of these massive merging systems.

In this introduction, we first define star clusters and important dynamical concepts such as relaxation time and virial state. We then develop the current state of theory, observations and simulation on cluster formation, substructure and early dynamical evolution. Finally, we look at alternative ways to investigate substructured dynamical evolution.



(a) The Pleiades, open cluster

(b) ω Centauri, globular cluster

Figure 1.2: Examples of various types of cluster. White bars at the lower left of each pictures show 1 parsec length scale. The dust present in the young Pleiades open cluster scatters starlight, producing this blue haze. The globular cluster ω Centauri contains one million stars and is the largest known star cluster in the Milky Way.

Credits: NASA, ESA, AURA/Caltech; ESO/INAF-VST/OmegaCAM

1.1 What is a star cluster ?

What is a star cluster ? A direct, almost tautological, definition is "a group of stars". However, this includes galaxies and random line-of-sight groups. We are interested in physical objects, smaller than galaxies, in which stars are, if not bound together, at least under direct mutual gravitational influence. Such objects include open clusters, globular clusters or associations. [Lada & Lada \(2003\)](#) adopted the following definition: a cluster is a stellar system with $N > 35$ and a density $\rho > 1 \text{ M}_\odot/\text{pc}^3$. These objects can either dissolve in less than a million year or remain bound for billions of years. In the last century, thanks to the improvement of observational technology, many clusters have been discovered and their origins are progressively being unravelled.

Clusters are the result of bursts of star formation in Giant Molecular Clouds (**GMCs**). All stars within a cluster were born approximately at the same time, which explains the sustained interest of the community for star clusters: they are the best available stellar physics laboratories, a large population of stars sharing the same age and distance to Earth. The age of the cluster can be derived from the most massive surviving stars in the population, as stars have lifetimes inversely correlated with their mass. Overall, integrated spectral features from all members of a star cluster can provide a wealth of information.

As we will see, clusters are also crucial to understand stellar formation. They harbour the most massive and young stars, which cause large-scale ionisation, winds and shockwaves from their explosive death in supernovae. Massive stars caused the re-ionization of the entire observable Universe 400 Myr after the Big Bang. To understand massive stars is to understand star formation, and to understand star formation is to understand star clusters.

Star clusters are historically divided into two "classical" categories: globular clusters and open clusters. As observational technology improved, categories tended to blend into a spectrum of size, age, and dynamical state, with Young Massive Clusters, embedded clusters and OB associations. Several of these categories have significant overlap, but each one emphasizes a particular characteristic of star cluster, thus these are useful for a comprehensive discussion.

Globular clusters are old and massive stellar systems, found orbiting most galaxies. Most of



(a) R136, Young Massive Cluster

(b) NGC 1333, embedded cluster

Figure 1.3: Examples of various types of cluster. White bars show 1pc. The young massive cluster R136 is surrounded by its primordial nebula while the embedded cluster NGC 1333 is still inside it. (b) is a composite of visible and infra-red light. *Credits: NASA, ESA, F. Paresce; T. Rector(U.Alaska Anchorage), H. Schweiker*

them are older than 10 Gyr and more massive than $10^4 M_{\odot}$. The most massive known Globular cluster in the Milky Way is ω Centauri, with $4 \cdot 10^6 M_{\odot}$ ([D'Souza & Rix, 2013](#)), see Fig 1.2b. They only contain stars, without any dust or gas. The 150 known globular clusters in the Milky way are scattered in the disk and the halo, with a higher concentration near the bulge ([Harris, 1996](#)).

Open Clusters are lighter objects, rarely more massive than $10^3 M_{\odot}$. They are also younger, with ages ranging from a few Myr to a few Gyr ([Dias et al., 2002](#)). Their small mass and lower density make them vulnerable to tidal disruption from passing massive clouds on nearby orbits. The pleiades are a famous example, see Fig 1.2a

OB associations contain even less stars than open clusters, a few dozens in average, among which very massive luminous O and B type stars, sometimes more massive than $50 M_{\odot}$. Such stars do not survive more than a few million years, OB association are thus young objects located in active star forming regions. They are often found near other associations, in a hierarchical structure. Their density is much lower than a typical cluster, about $0.1 M_{\odot} pc^{-3}$ ([Wright et al., 2014](#); [Garcia et al., 2010](#)), in fact most are unbound and dissolving objects.

Embedded clusters are the youngest star clusters in the sky. Most of the stars, protostars and cores are still inside their primordial cloud, dust obscuring their optical light. The development of infrared astronomy unveiled the internal structure of these objects. Embedded clusters are young (<10Myr) and observed to be substructured ([Kuhn, Getman & Feigelson, 2015](#)). Some have ongoing star formation, like NGC 1333, a very young embedded cluster with both proto-stars and stars, see [Foster et al. \(2015\)](#) and Fig 1.3b.

Young Massive Clusters, or YMCs, are considered to be globular cluster progenitors. The review by [Portegies Zwart, McMillan & Gieles \(2010\)](#) provides a definition of YMCs: bound systems more massive than $10^4 M_{\odot}$ and younger than 100 Myr. Only a handful of such systems are known in the milky way (see Fig 1.4). The most studied YMC of the galactic neighborhood is R136, with a mass $\sim 10^5 M_{\odot}$ ([Andersen et al., 2009](#)), see Fig 1.3b. It is

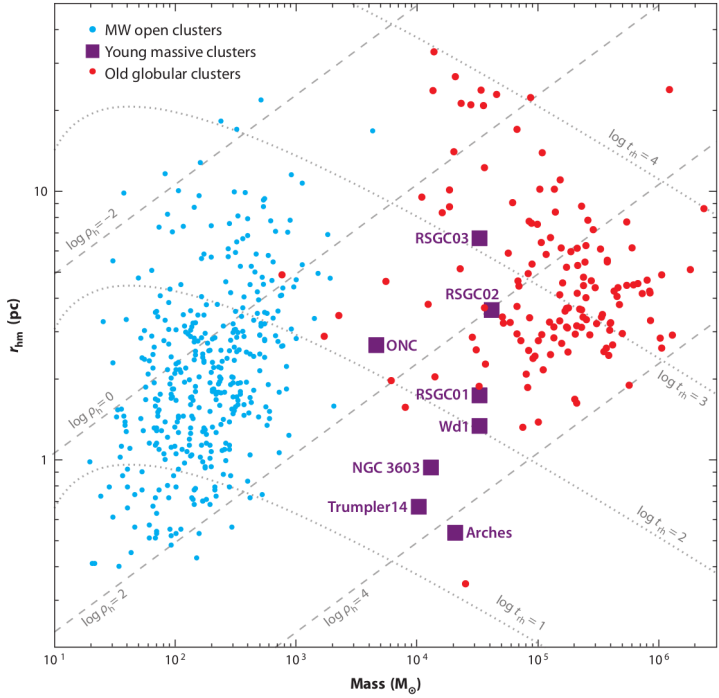


Figure 1.4: Radius-Mass Diagram for Milky Way clusters. Blue dots are open clusters, red dots Globular clusters and purple squares show Young Massive Clusters. Dashed lines show constant density within half-mass radius $\rho_h = 3M/8\pi r_{hm}^3$ and dotted lines show constant half-mass relaxation time. The plot was taken from the review [Portegies Zwart, McMillan & Gieles \(2010\)](#).

located in the Tarentula nebula, the most active known star forming region in the local group, inside in the Large Magellanic Cloud ¹. YMCs are found in large number in intense star forming environment such as starburst galaxies and galaxy mergers like the Antenna galaxies ([Whitmore et al., 2010](#)).

”All stars form in clusters” is a recurring statement in the field of stellar and cluster formation. Near Infra-Red (NIR) studies of star forming region yielded a star formation rate from embedded clusters of $\sim 3 \cdot 10^3 M_\odot \text{ Myr}^{-1} \text{ kpc}^2$ ([Lada & Lada, 2003](#)) while the same estimation for field stars in the milky way gives $\sim 3 - 7 \cdot 10^3 M_\odot \text{ Myr}^{-1} \text{ kpc}^2$ ([Miller & Scalo, 1979](#)). Another clue at the clustered nature of star formation is that high-mass O stars are for the vast majority, clustered, see [de Wit et al. \(2005\)](#). Due to their short life, O stars are often observed at the very location of their birth, or not very far. However, recent observations by, e.g, [Gutermuth et al. \(2011\)](#) shows a spatially hierarchical star formation. The spherical, concentrated clusters we observe are then the outcome of a merging process from subclusters.

1.2 Some important dynamical concepts

Before going into details about cluster formation and subsequent dynamical evolution, it is necessary to define some crucial dynamical concepts.

1.2.1 Virial theorem

A self-gravitating system is a system bound by its own gravity. This applies to a star, a molecular cloud, a star cluster or a galaxy. In all cases, gravity is set against a counteracting source of

¹A dwarf irregular galaxy orbiting the milky way.

energy that prevents the total collapse of matter into a single point. This source can be pressure for stars and clouds, but for stellar systems such as clusters and galaxies, it is the agitation of its components, the kinetic energy of the stars. Other energy sources include magnetic pressure or tidal fields.

The exchange between the gravitational potential energy and the internal energy follows the virial theorem, written in the general form (McKee & Ostriker, 2007; Binney & Tremaine, 2008):

$$\frac{1}{2} \frac{d^2 I}{dt^2} = 2(E_k - E_{k,s}) + E_p + E_{tides} + E_m \quad (1.1)$$

with I the moment of inertia, E_k the kinetic energy, E_p the potential energy. $E_{k,s}$ a thermal pressure surface term, E_{tides} the energy injected by a tidal field and E_m the magnetic pressure. For a stationary system, $\frac{1}{2} \frac{d^2 I}{dt^2} = 0$, and in a purely gravitational system with N particles, there is no thermal or magnetic pressure. Finally, if we consider an isolated system, $E_{tides} = 0$ and the virial theorem can be written in its more common form:

$$2E_k + E_p = 0 \quad (1.2)$$

with :

$$E_k = \sum_{i=1}^N m_i v_i^2 \quad \text{and} \quad E_p = - \sum_{i=1}^N \sum_{j>i}^N \frac{G m_i m_j}{\|\mathbf{r}_i - \mathbf{r}_j\|}. \quad (1.3)$$

We define the virial parameter Q as:

$$Q = -\frac{E_k}{E_p}, \quad (1.4)$$

$Q = 0.5$ is a system in virial equilibrium. If the amplitude of the velocities is not sufficient to counteract the current value of potential energy, $Q < 0.5$, the system is said to be dynamically cold, or *subvirial*. While if the stars are too close together compared to their velocities, $Q > 0.5$, the system is hot and *survirial*. If $Q > 1$, the total energy is positive and the system is unbound.

1.2.2 Dynamical timescales

Dynamical systems, like star clusters, tend to virial equilibrium. In such self-gravitating systems, it is useful to define a few dynamical time scales. The most simple one is the **crossing time**, defined as the time for a typical particle to cross the system. Following standard definitions (Meylan & Heggie, 1997; Fleck et al., 2006), it is expressed as

$$t_{cr} = \frac{2R_h}{\sigma} = \frac{2R_h}{\sqrt{GM/R_g}}, \quad (1.5)$$

where R_h is the half-mass radius, σ the three-dimensional velocity dispersion, M the mass of the system of gravitational radius R_g given by $GM/R_g = \sigma^2$.

Another crucial timescale in stellar dynamics is the **relaxation time**, which can be defined as (Heggie & Hut, 2003):

$$\frac{t_{rel}}{t_{cr}} = \frac{0.138}{2} \left(\frac{R_h}{R_g} \right)^{1/2} \frac{N}{\ln 0.4N} \quad (1.6)$$

In a self-gravitating system, stars have orbits. If N is large enough, the potential inside the system is smooth and stars have stationary orbits. The relaxation time is the timescale at which the impact of numerous encounters a star endures is comparable to the motion of its initial orbit. In other words, the initial conditions of a system are dynamically erased by collisional evolution after a relaxation time.

In a relaxed cluster, the core is dense with a high velocity dispersion, whereas the outskirts, the halo, is less dense and stars are slower. The definition from equation (1.5) and (1.6) imply the relaxation time changes with distance to the center. It is therefore useful to define a global timescale for the whole system, the **half-mass relaxation time** defined by [Heggie & Hut \(2003\)](#):

$$t_{rh} \simeq \frac{0.138}{\ln(0.4N)} \sqrt{\frac{N}{Gm}} R_h^{\frac{3}{2}} \quad (1.7)$$

with m the mass of a star and R_h the half-mass radius. Let us compute two examples, taking G in appropriate units:

$$G \simeq 4.48 \times 10^{-3} \text{ pc}^3 \text{ Myr}^{-2} \text{ M}_\odot^{-1}. \quad (1.8)$$

A cluster with 1000 stars of 0.5M_\odot and $R_h = 1$ pc has $t_{rh} = 13$ Myr, while a cluster with 10^6 stars of the same mass and a $R_h = 6$ pc has $t_{rh} = 3.1$ Gyr.

Equations (1.6) and (1.7) assume identical stellar masses in the system. In a real cluster, stars have different masses, differently affected by collisional evolution. The most massive stars cause gravitational focusing and exchange energy with other stars at a higher rate. They lose their energy to lighter stars, progressively sinking at the center. [Heggie & Hut \(2003\)](#) give an estimation of the segregation timescale $t_{ms}(m_1)$ of a mass m_1 :

$$t_{ms}(m_1) = \frac{m_1}{\langle m \rangle} t_{rh} \quad (1.9)$$

so a 30 M_\odot star in the previous 1000 star cluster will have a much shorter relaxation time of $\frac{0.5}{30} 13 = 0.21$ Myr = 210,000 years. A mass spread in a system speeds up considerably its collisional evolution.

A more general expression than (1.9) can be obtained to quantify the global segregation timescale. From [Fleck et al. \(2006\)](#), the mass-segregation timescale writes:

$$\frac{t_{ms}}{t_{rel}} \equiv \frac{\pi}{3} \frac{\langle m_\star \rangle}{\max\{m_\star\}} \frac{\bar{\rho}_h}{\rho_g} \left(\frac{R_h}{R_g} \right)^{3/2}, \quad (1.10)$$

where $\bar{\rho}_h = M/(4\pi/3)R_h^3$ is the mean density within radius R_h , and ρ_g the mean density inside a sphere of radius R_g .

1.2.3 Static models

It is useful to have a static reference model for a self-gravitating system at equilibrium. Considering a relaxed system with enough particles, one can use a statistical description to model its evolution, namely the "collisionless Boltzmann equation":

$$\frac{\partial f}{\partial t} + \mathbf{v} \cdot \nabla_r f - \nabla \Phi \cdot \nabla_v f = 0 \quad (1.11)$$

with $f(\mathbf{r}, \mathbf{v}, t)$ the phase space distribution and Φ the gravitational potential. There are several solutions to this equations, these are "static" models for star clusters as they are considered in equilibrium. Of course, the collisional equation can never be fully neglected and these models are approximations. We present here two models: Plummer and King. Both have a constant density in the center, the core, but they differ by their general behaviours.

The **Plummer model** is a simple model with a null potential at infinity. It is defined by its potential as a function of radius ([Binney & Tremaine, 2008](#)):

$$\Phi(r) = -\frac{GM}{\sqrt{r^2 + b^2}} \quad (1.12)$$

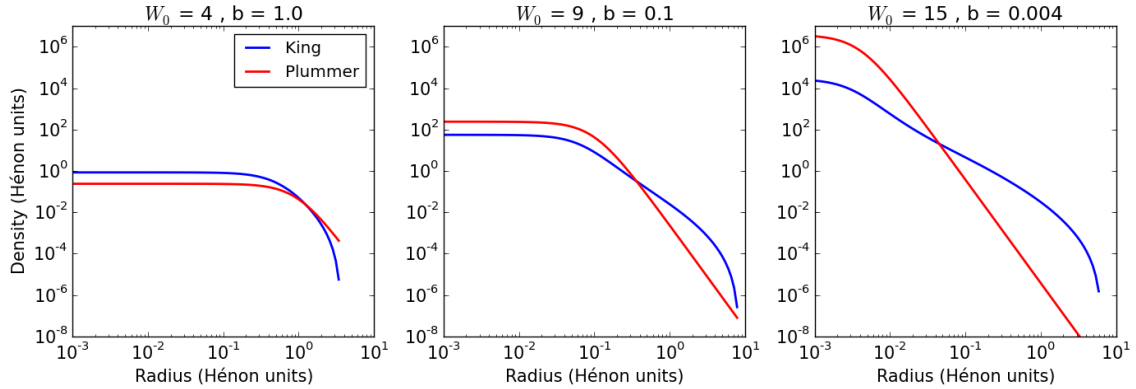


Figure 1.5: Comparison of King and Plummer models density as a function of radius, for similar core radii.

with b the Plummer parameter, setting the depth of the central potential and the core radius. From this expression, one can derive the radial density distribution:

$$\rho(r) = \frac{3M}{4\pi b^3} \left(1 + \frac{r^2}{b^2}\right)^{-\frac{5}{2}} \quad (1.13)$$

Equation (1.13) makes the computational generation of a cluster straightforward, which is why the Plummer model has been widely used in numerical simulations of star clusters. However, a Plummer model theoretically extends to infinity, and is not consistent with many globular cluster observations. Another, more complex, model has the observers on his side. The **King model** has been successfully used to fit light-profiles of globular clusters (King, 1981). It is defined as a distribution in energy:

$$f_k(E) = \begin{cases} f_0 \left(e^{-2j^2 E} - e^{-2j^2 E_0} \right), & \text{if } E < E_0. \\ 0, & \text{otherwise.} \end{cases} \quad (1.14)$$

with j a free parameter. The core radius can be tuned through a parameter $W_0 = 2j^2(E_0 - E_c)$ with E_c the rest energy at the center.

The main difference with the Plummer model can be seen in Fig 1.5: for a given core radius, King's density decreases slower than Plummer, but does fall to zero at a given radius contrary to Plummer that continues to infinity.

1.3 The origin of star clusters

In this section, we describe the current understanding of star formation and its substructured spatial distribution in relation to that of the ISM. We then describe the dynamical evolution brought by this distribution and how it relates to the expulsion of the primordial gas by the young stars.

1.3.1 From gas to stars

The interstellar medium, or ISM, is made of dust and gas in various phases, densities and temperatures, ranging from a hot ionized medium ($T > 10^5$ K and $n < 0.01 \text{ cm}^{-3}$) to a cold neutral medium ($T < 100$ K and $n > 10 \text{ cm}^{-3}$), see Field, Goldsmith & Habing (1969). Finally, in colder denser regions, $T \sim 10$ K and $n > 30 \text{ cm}^{-3}$, the hydrogen takes molecular form H_2 in what is called molecular clouds. The dust contained in these regions makes them optically thick, obscuring background stars. These "holes in the sky", as William Herschel exclaimed upon the

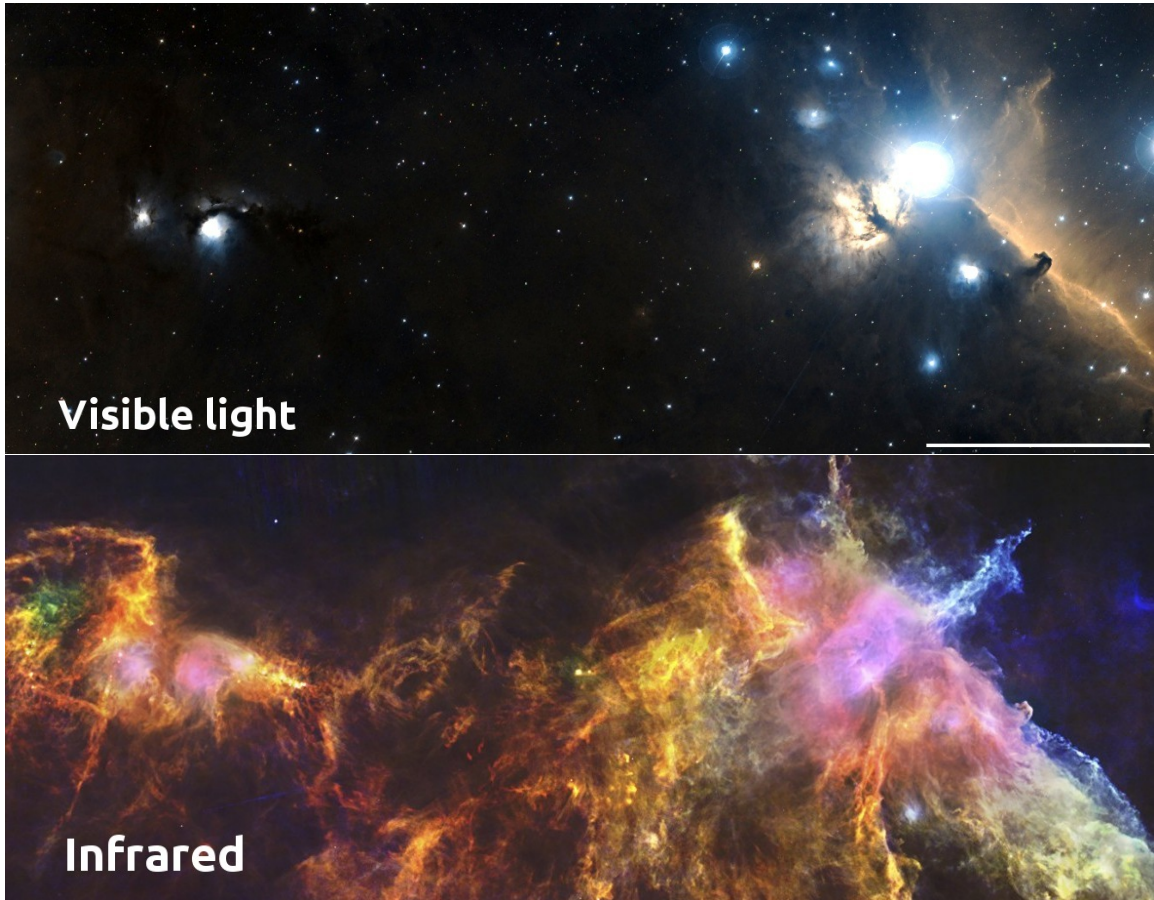


Figure 1.6: Visible light and infrared view of a part of the Orion star forming complex. Horshead nebula is visible on the right, as well as the very bright star Alnitak, part of the Orion belt. NGC 2071 and 2068 are visible on the left. Pink infrared coloring shows radiation from very bright young massive stars forming in the cloud. Colder filaments are visible all around. White bar on lower right of visible shows 1 parsec. *Credits: Digitized Sky Survey; ESA/Herschel/PACS.*

Dark Ophiucus Nebula ([Houghton, 1942](#)), come in different sizes, from the Bok globules to Giant Molecular Clouds (GMCs). The interstellar dust absorbs the light in the visible and re-emits it in the infrared, thus the advent of infrared astronomy unveiled the interior of molecular clouds. In particular, recent observations with the Herschel Space Observatory showed a prevalence of filaments in clouds, see [André et al. \(2010\)](#) and Fig 1.6.

Star formation occurs in the higher density clumps or filaments inside the clouds. The origin of these overdensities has been the object of extensive theoretical development for 60 years. Turbulent motion was very early on designated as the main cause of overdensity. Turbulence is the transfer of energy from large scales to small scales, creating motions on small scales from a large energy driver. The well known Kolmogorov incompressible turbulence is hardly applicable to the ISM, as it is highly compressible ([Scalo et al., 1998](#)), instead, molecular clouds are subject to supersonic turbulence, or Burgers turbulence ([Frisch, Bec & Villone, 2001](#)). Nearby supernovas or tidal perturbation feed energy into the cloud, which is transferred through turbulence to smaller scales as supersonic internal motions, shocks forming overdense sheets. [McKee & Ostriker \(2007\)](#) argue that filaments originate both from the intersection of such sheets and the primordial morphology of the cloud, as self-gravitating matter tends to condense as filaments ([Springel et al., 2005](#)).

Individual condensates of matter called cores form in clumps and filaments, these are stellar seeds (Fig 1.7a). They collapse when their self-gravity overcome their magnetic and thermal

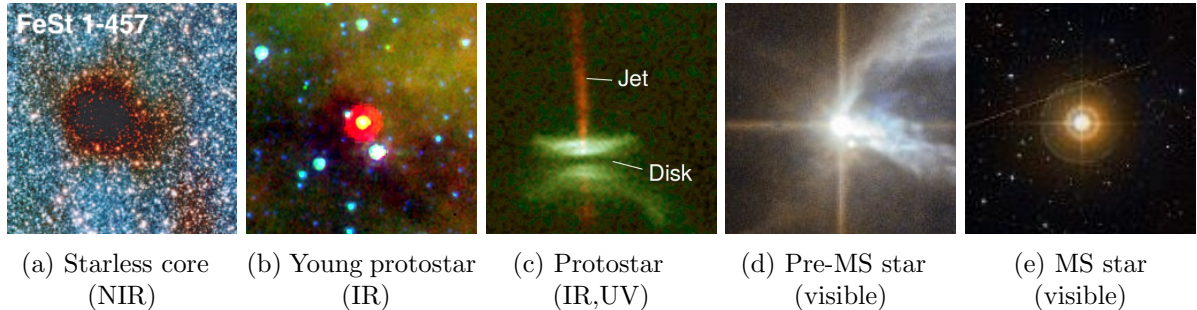


Figure 1.7: Stages of stellar birth. (a) is just cold molecular gas and contains no central source yet. (b) is more advanced, though hidden in visible light, its central protostar shines in infrared. The protostar in (c) is actively accreting its disk and produces jets. (d) is a pre main-sequence star, free from its envelope and surrounded by primordial gas. (e) is the mature stellar stage: the main sequence. *Credits: Kandori et al. (2005); NASA/JPL-Caltech/Evans,N; Burrows,C/HST-NASA; ESA/Hubble & NASA; DSS*

pressure and internal turbulence. When the central temperature increases and all molecular hydrogen has been dissociated, the collapse stops and the protostar is born (Fig 1.7b). It starts accreting its gaseous envelope. Angular momentum from the original cloud shapes the envelope into a disk around the protostar, and magnetic activity starts creating jets (Fig 1.7c). After about a Myr, accretion stops and the object becomes a Pre-Main Sequence (PMS) star (Fig 1.7d). It slowly contracts, following the [Hayashi \(1961\)](#) track, to finally reach 10^6K in its core and start fusing hydrogen into Helium. The object enters the Main Sequence and begin its life as a "proper" star (Fig 1.7e). See [Larson \(1969\)](#) for a theoretical overview of the principles of collapse and protostellar formation.

1.3.2 Substructure and early dynamical evolution

These stars emerges from molecular clouds, which are observed to be heavily substructured (see e.g. [Cambrésy 1999](#)). This substructure can be seen as a fractal distribution ([Elmegreen & Falgarone, 1996](#)) or a network of filaments ([André et al., 2010](#)), both consistent with compressible turbulence ([McKee & Ostriker, 2007](#)). Cores and protostars inherit this hierarchical structure as many observational studies of star forming regions, or substructured young clusters, show ([Schneider & Elmegreen, 1979](#); [Hartmann, 2002](#); [Bressert et al., 2010](#)). See for example the distribution of Young Stellar Objects in the Carina Nebula on Fig 1.8. Examples of substructured young clusters include the Taurus Ariga region, ρ -Ophiucus and Aquila, details and other examples can be found in both volumes of *The handbook of star forming region* [Reipurth \(2008\)](#).

However, other young clusters do not display such fractal, clumpy or filamentary structure. Instead, they are smooth, centrally condensed systems. The most known example is the Orion Nebula Cluster, or ONC. Located in the heart of the Orion complex, the largest and most active star forming region in the solar neighborhood, the age of the ONC is estimated to a few Myr. [Hillenbrand & Hartmann \(1998\)](#) found no clumps or filaments in the stellar distribution of the cluster, but a smooth distribution with a high density core formed by the Trapezium, a dense system of massive stars. This mass segregation, if not fully primordial, implies that some amount of dynamical evolution took place in the ONC since the formation of the stars. This dynamical evolution could have erased the initial substructures.

This is consistent with observations by [André et al. \(2007\)](#) who found clumps of prestellar objects to have a very low velocity dispersion in Ophiucus, meaning these clumps are more likely to merge and interact than diverge and disperse in the field.

These observations point at a rough picture of substructured stellar formation and early evolution: when the newly born stars emerges in clumps, if the background tidal field is weak and

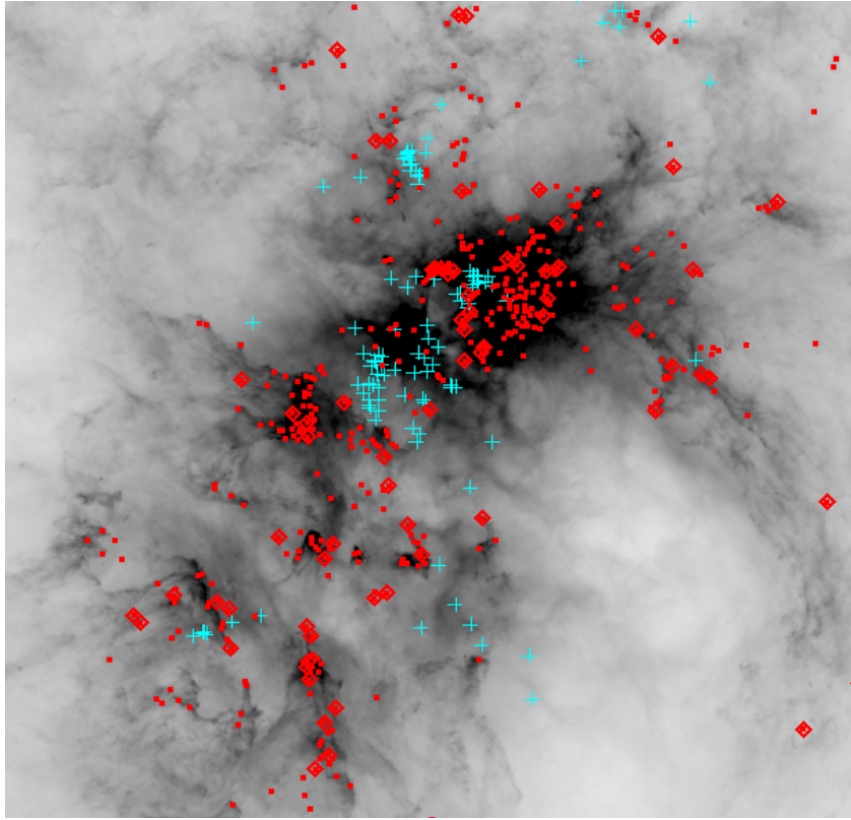


Figure 1.8: Herschel IR 70m observations of the Carina Nebula, with YSOs as red points and diamonds. Cyan crosses show OB stars. Both the gas and prestellar objects follow a substructured distribution. The figure was extracted from [Gaczkowski et al. \(2013\)](#).

the star forming region sits well inside its Roche radius, the clumps then progressively merge and converge to the system barycentre to form a unique, relaxed self-bound association over a course of a few crossing time. This picture is backed up to some extent by hydrodynamical simulations of fragmentation modes in the turbulent ISM ([Klessen & Burkert, 2000](#); [Bate, Bonnell & Bromm, 2003](#); [Mac Low & Klessen, 2004](#); [Offner, Hansen & Krumholz, 2009](#); [Maschberger et al., 2010](#)) and by recent observational clues that subclusters show dynamical traces of mergers ([Kuhn et al., 2015](#)).

1.3.3 Star formation efficiency and infant mortality

Though stars form in a hierarchical clumpy structure, star forming regions are vulnerable to gas expulsion and dispersion.

In their seminal paper on embedded clusters, [Lada & Lada \(2003\)](#) coined the term "infant mortality" for young star clusters. Comparing the populations of embedded clusters and older open clusters, the authors concluded clusters had a 90% mortality rate before 10 Myr. This is explained by the traditionnal picture of gas expulsion in clusters: a portion of the gas in a molecular clouds form a group of protostars, which quickly accrete their envelope, then start nuclear burning. This portion is expressed as the star formation efficiency:

$$\epsilon = \frac{M_*}{M_* + M_{gas}} \quad (1.15)$$

with M_{gas} the remaining gas after star formation. This gas is thought to be ejected from the young cluster through photo-ionization (the UV radiation from massive stars ionize the neutral

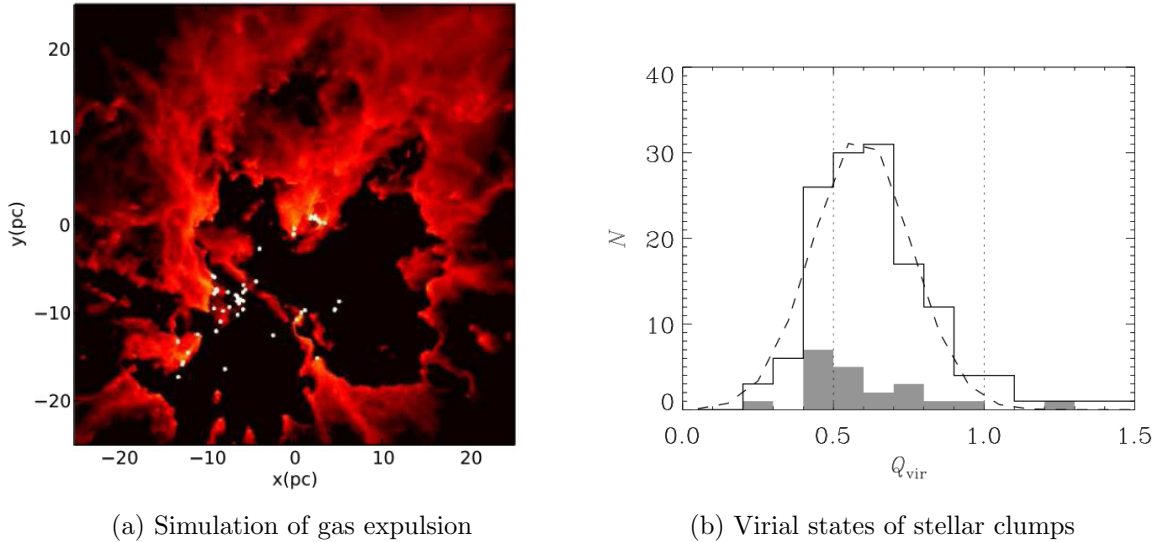
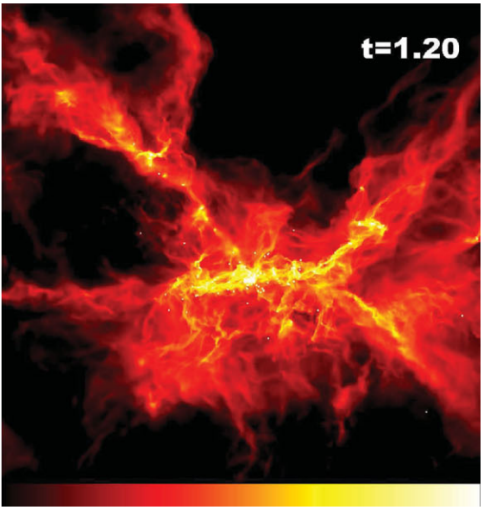


Figure 1.9: (a): hydrodynamical simulation of wind-induced gas expulsion around a small cluster, the figure was extracted from [Dale et al. \(2013\)](#). (b) virial parameter of stellar clumps in a star forming hydrodynamical simulation, ignoring the potential of the gas to predict their post-expulsion fate. The solid line is the cumulated distribution of clumps over all snapshots; the shaded histogram shows the final distribution. The figure was extracted from [Kruijssen et al. \(2012\)](#).

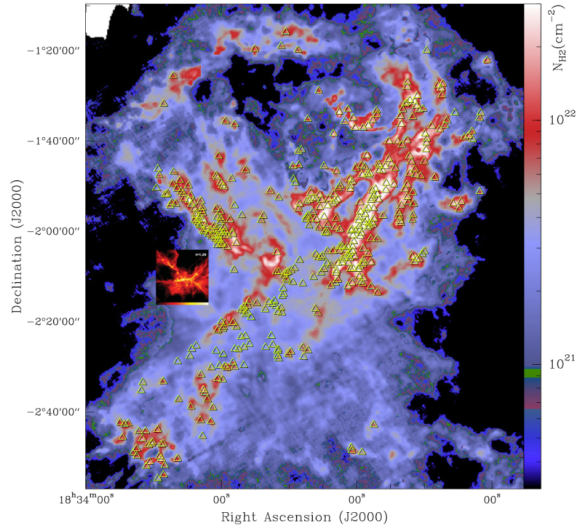
gas which heats up and expands), jets and outflows (young stars ejecting matter during accretion), winds (ejection of matter from stars surfaces at high speeds), and supernovae (shockwave from the explosive death of a massive star). The gas expulsion occurs on a crossing timescale, see [Krause et al. \(2016\)](#). Considering a young cluster in dynamical equilibrium, the loss of the mass of the gas on such a short timescale can unbind the system, as the stars velocities are now too high for the new potential well. The young cluster then dissolves following the gas expulsion. This picture is backed up by observations of young dissolving clusters ([Bastian & Goodwin, 2006](#)) consistent with corresponding numerical models ([Goodwin & Bastian, 2006](#)). Extensive analytical and numerical work have explored this process, e.g. [Tutukov \(1978\)](#); [Hills \(1980\)](#); [Lada, Margulis & Dearborn \(1984\)](#); [Adams \(2000\)](#); [Boily & Kroupa \(2003a,b\)](#), with an estimated minimum star formation efficiency of 30% to remain bound after gas expulsion.

However, the picture is more complicated than it seems. The interaction between types of stellar feedback, such as winds, photoionisation and supernovae, is not well understood ([Dale & Bonnell, 2011](#); [Dale et al., 2013](#)), and their exact timescales can have a large influence on cluster survival ([Pelupessy & Portegies Zwart, 2012](#)). Another serious issue with the classical picture of gas expulsion is that star formation is substructured and clusters undergo dynamical evolution while the gas is being evacuated, making survival heavily dependant on the clumpy structure, as shown by [Farias et al. \(2015\)](#). Hydrodynamical simulations and recent observations show stellar clumps can be resistant to gas expulsion even before global dynamical relaxation ([Kruijssen et al., 2012](#); [Kuhn et al., 2015](#)), see Fig 1.9b which shows the distribution of virial parameter Q of stellar clumps in a simulation, ignoring the gas potential. The vast majority have $Q < 1$ and are expected to stay bound after expulsion.

Substructure and dynamical evolution have a prominent place in the issue of cluster survival. In this work, we study this phenomenon without a hydrodynamical treatment of the gas to isolate purely dynamical effects.



(a) Observed distribution of gas and protostars



(b) Hydrodynamical simulation

Figure 1.10: Comparison of star formation hydrodynamical simulation from [Bate \(2012\)](#) (a) and Herschel infrared observations of the Aquila star forming complex, extracted from [Könyves et al. \(2010\)](#) (b). Gas column density is shown as levels of red and yellow on the left and as levels of blue and red on the right. The simulation spans 0.6 parsecs while the observations, with the distance estimate from the authors, span 7 parsecs. We inserted the simulation into the observation to compare the scales.

1.4 Simulating star clusters evolution

In this section, we describe the general characteristics of the hydrodynamical simulations invoked earlier in this introduction. We emphasize their qualities and shortcomings, of which their limited system size. We then turn to alternative methods to numerically reproduce the early dynamical evolution of star clusters.

1.4.1 Hydrodynamical simulations

To model the formation of a star cluster from a core-less molecular cloud is no easy task. The model has to reproduce turbulence, core condensation, gravitational collapse, accretion, and for the most realistic ones, stellar feedback, magnetic effect and dust chemistry. Two numerical paths have been explored in the past: AMR and SPH.

Adaptive Mesh Refinement, AMR, is an Eulerian approach. The hydrodynamical equations (conservation of mass, momentum, the equation of state) are discretized and solved on a grid of cells following the finite volumes methods (see the RAMSES code, [Teyssier 2002](#)). Smoothed Particle Hydrodynamics, SPH, is a Lagrangian approach: instead of looking at inputs and outputs of matter in a cell, the gas is subdivided in particles free to move in the system. They are attributed a density, temperature and pressure. This method is akin the N-body integrator, and many SPH codes can work as purely gravitational integrators. Even if these codes can handle high density contrast, the collapse and formation of a protostar can still bring the numerical computation to a standstill. The usual workaround is the use of sink-particles: passed a given density threshold, several gas particles are merged into a single point-like object able to accrete any infalling matter. This works well though it suppresses any physical process below this accretion limit, usually a few to a hundred AU. ([Bate & Burkert, 1997](#)).

The precision, size and complexity of cluster formation simulations have been steadily improving for 20 years (see [Turner et al. 1995](#); [Klessen & Burkert 2000](#); [Bate, Bonnell & Bromm](#)

2003; Offner, Hansen & Krumholz 2009; Myers et al. 2014 and references). Nevertheless, no simulation to date include realistic cooling processes, radiative and wind feedback, magnetic fields and dust chemistry, all at the same time. All these are crucial to achieve precise and realistic simulation of the star formation process. Moreover, one of the most detailed star formation simulations to date, e.g [Bate \(2012\)](#), only form a few hundred stars in a volume spanning less than 1 pc and evolved them for less than 0.2 Myr with a simulation run time of several months. In fact, while looking at a typical star forming region, hydrodynamical simulations often reproduce a single fragment, see Fig 1.10b.

However, good results are already being achieved, see the short review by [Clarke \(2012\)](#). Stellar properties and general structure agree with observations and interesting results are being obtained. [Maschberger & Clarke \(2011\)](#) and [Moeckel & Clarke \(2011\)](#) have noted that massive stars tend to sit at the heart of gas clumps in hydrodynamical simulations, some as the result of merger events with low-mass proto-stars. The hydrodynamical treatment allows the formation of gaseous disks around protostars that can influence the dynamics on small scales.

In summary, though hydrodynamical simulations are not yet fully realistic, they provide a good approximation of reality for small clusters and allow exploration of early dynamical processes. However, they cannot model the dynamical interactions between stellar sub-clusters and their consequences on a more massive final system.

1.4.2 Artificial substructure

There is a persistent difficulty to bridge over self-consistently from the star formation phase, to the equilibrium configuration of bound clusters. Hydrodynamical calculations of star forming regions evolve for up to a few 10^5 years, when a stable configuration would require several 10^6 years at typical cluster densities of 10^4 to 10^5 stars per cubic parsec. A way to overcome this issue is to switch to purely gravitational N-body simulations once the stars formed and most of the gas has been either accreted or expulsed. It is computationally less expensive and allows for longer integration of larger systems.

It is then essential to obtain a good model of the stars phase-space distribution at the end of a hydrodynamical simulation. While King and Plummer model have a known distribution one can sample from, no such thing exist for the clumps and filamentary structure of the newborn stellar objects in star-forming regions. Several methods have been explored to solve this.

Sink particle distribution is the most straightforward solution. [Moeckel & Bate \(2010\)](#) took the distribution of sink particles formed in the hydrodynamical simulation by [Bate \(2009\)](#) and directly converted it as a stellar distribution, preserving the masses, positions and velocities of the "stellar seeds". This is probably the best initial conditions for nbody simulations of young clusters that can be achieved, at the cost of speed, sampling and size. The initial hydrodynamical simulation took months to complete, making it hard to run it again and impossible to run it multiple times to obtain a good statistical sampling of the model. The size of the cluster achieved cannot exceed 1000 stars given the current state of hydrodynamical simulations.

Stellar spawning from hydrodynamics is a variant of the previous method. [Fujii & Portegies Zwart \(2016\)](#) started from hydrodynamical simulations of massive molecular clouds and stopped the integration once the main structures had formed but before local gravitational collapse had set in. Stars were then spawned in space following the distribution of gas. This enables larger clusters and quicker initial conditions of structures. However, the velocity distribution of these new stars is artificial, as it can at best inherit the gas velocity, without including the impact of the early collisional evolution that occurs between protostars in the clumps.

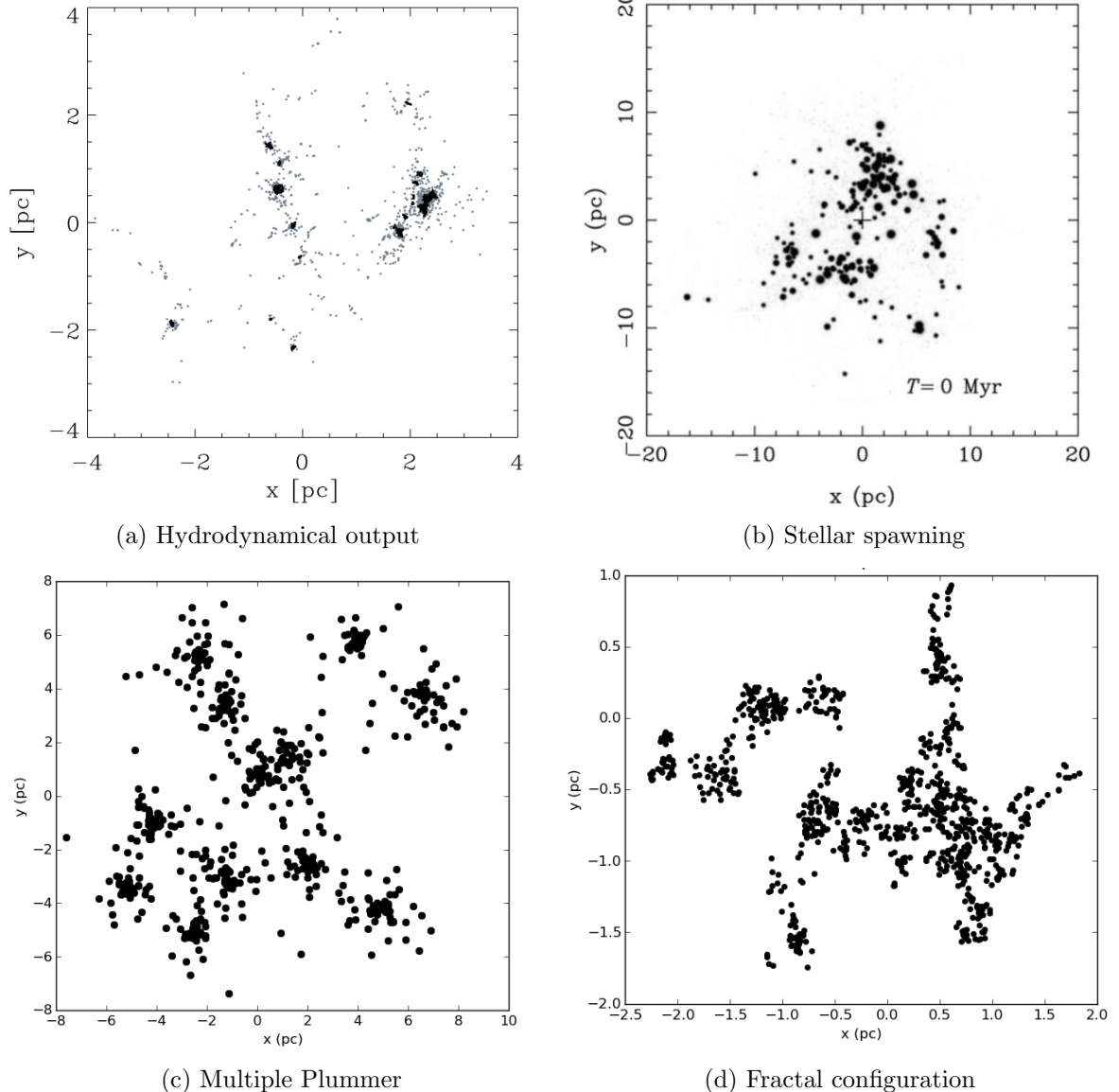


Figure 1.11: Representation of four methods to generate substructures. (a) is extracted from Kruijssen et al. (2012), constructed with data from Bonnell, Bate & Vine (2003), (b) is extracted from Fujii (2015). (c) and (d) were generated for this work.

Scattered Plummer spheres is an analytic answer to the substructure problem. [McMillan, Vesperini & Portegies Zwart \(2007\)](#) created a clumpy model for a young star cluster by spawning several Plummer spheres randomly in space. This is almost immediate and is a good approximation. The authors obtained interesting results on the inheritance of mass segregation during mergers. However, clumps within a young star clusters have no reason to follow a Plummer profile, this places a constraint on the clumps internal dynamics which bias the dynamical evolution.

Fractal models were introduced by [Goodwin & Whitworth \(2004\)](#) and has been used in numerous studies ever since, e.g. [Allison et al. \(2009b\)](#); [Kouwenhoven et al. \(2010\)](#); [Parker & Wright \(2016\)](#). The idea is to grow a 3D pseudo-fractal tree with probabilistic branching, up to a given level, turning the final leaves into stars. The method is fast and the result is spatially realistic, fitting the observation that finds a fractal structure in the molecular clouds and star forming regions. However, the velocity distribution is artificial, drawn from successive gaussians at each levels. The clumps will relax when integration starts, shaking the whole system right off the bat.

It seems the generation of substructure has to balance realism and computational cost. The most realistic method is too costly, and most of the quicker alternatives are disconnected from the dynamical effect arising from the collisional effects young stars undergo inside a clumpy configuration. There is a need for an computationally efficient method to produce dynamically consistent initial conditions to model young star clusters and study their evolution, which is what we introduce in the next section.

Part I

The fragmented model and its evolution

CHAPTER 2

The Hubble-Lemaître fragmented model: analytical approach

In this chapter we introduce a new way to obtain substructured initial conditions: the Hubble-Lemaître model. We derive the equations governing the expansion and perform a perturbation analysis to investigate the growth of idealized overdensities.

Contents

2.1 How to build a Hubble-Lemaître model	30
2.1.1 Initial state	30
2.1.2 Fragmentation	31
2.2 The growth of overdensities: analytical study	33
2.2.1 Working equations	33
2.2.2 Linear density perturbation	34
2.2.3 Consistent initial conditions	36
2.2.4 Segregation time-scale	37
2.2.5 Example with $N = 15000$	40
2.3 Concluding remarks	40

For decades, cosmologists studied the development of substructures in the early universe. In an expanding universe, each point in space sees others moving away, with a velocity proportional to their distances, thus a smooth universe should stay smooth, no structure should develop. However, when the matter distribution is not perfectly smooth, the density fluctuations will grow through gravity, accreting nearby matter, against the cosmological flow. These overdensities turn into galaxies, that then clump together to form galaxy clusters, building up a hierarchical density distribution, see [White & Rees \(1978\)](#); [Aarseth, Turner & Gott \(1979\)](#). This is the general picture for galaxy formation.

We apply this process to star clusters to obtain hierarchical substructures. We set up relatively smooth initial conditions by spawning stars in a uniform sphere, to which we attribute radial velocities akin to the well-known Hubble velocity field of nearby galaxies. When left to evolve, the model expands, reproducing the cosmological expansion, and overdensities grow, stars clump together, spontaneously forming substructures. We name this method the Hubble-Lemaître fragmentation. The name of Georges Lemaître was added for historical accuracy. It has now been shown that the astronomical observations of redshifted galaxies and its interpretation as the consequence of an expanding universe predated Hubble's paper ([Hubble, 1929](#)). Georges Lemaître had published his conclusion on an expanding universe two years earlier ([Lemaître, 1927](#)). The account of this can be found in [Kragh & Smith \(2003\)](#); [van den Bergh \(2011\)](#) and [Freeman et al. \(2015\)](#).

As the model is analog to the cosmological model of an expanding universe, we adopt the usual notations in the present chapter. However, important differences should be noted:

- our model is not periodic but isolated and can be inserted in any environment;
- our particles follow a stellar mass function, at odds with the single-mass cosmological simulations;
- we use a collisional integrator to perform the expansion and monitor close particles interactions;
- the expansion of our model slows down over time, as there is no internal energy source akin to the cosmological Dark Energy;
- the density fluctuations are not inserted from a known power spectrum but arise naturally from spatial Poisson noise and the stellar mass function.

Our view is that by following through with a full stellar IMF, the massive stars will define a radius of influence around themselves and sit preferentially, but not systematically, at the heart of sub-structures, retrieving a feature seen in star formation calculations ([Moeckel & Clarke, 2011](#); [Maschberger et al., 2010](#)), while short-cutting costly computer calculations. The configuration that is sought here is not unlike the situation found in the formation of galaxy clusters in cosmology, as massive galaxies tend to drag in less massive ones and sit at the heart of clusters.

2.1 How to build a Hubble-Lemaître model

2.1.1 Initial state

The first step to obtain a HL-fragmented model is to build an uniform sphere model. The N stars, depending on the required membership, have to be distributed randomly in space inside a certain radius, producing an uniform density. This can be achieved by sampling separately the distance to the center and the angular position of each star, in a method analog as used in [Aarseth, Hénon & Wielen \(1974\)](#) for a Plummer model. The distance to the center should be sampled from the function:

$$f_R(X) = R_0 X^2 \quad (2.1)$$

With R_0 the bouding radius and X a random variable following a uniform probability law between 0 and 1. A direct uniform law for the radius would overpopulate the outer regions. The angles ϕ and θ , respectively azimuthal and polar angle in the physics convention, should be sampled from:

$$f_\phi(X_1) = 2\pi X_1 \quad (2.2)$$

$$f_\theta(X_2) = \arccos(X_2) \quad (2.3)$$

With X_1 following a uniform probability law between 0 and 1 and X_2 between -1 and 1. The cartesian coordinates are then found:

$$x = R \sin \theta \cos \phi \quad (2.4)$$

$$y = R \sin \theta \sin \phi \quad (2.5)$$

$$z = R \cos \theta \quad (2.6)$$

$$(2.7)$$

The N particles are then homogeneously distributed in space in a sphere of radius R_0 . The next step is to attribute velocities. Unlike other models like the Plummer model, the velocities are here straightforward. We use the Hubble-Lemaître velocity field of neighbouring galaxies: velocities are radial from the Milky Way, larger with increasing distances, taking the form:

$$\mathbf{v} = H_0 \mathbf{r}, \quad (2.8)$$

with H_0 being an equivalent of the well-known Hubble parameter. An appropriate H_0 to obtain a fragmented subvirial model has to be inferior to $\sqrt{2}$ (see next section). The model obtained from this is then evolved through a nbody integrator, which in this case is NBODY6.

2.1.2 Fragmentation

The cluster expands, driven by the initial Hubble-Lemaître velocity field. During this expansion, poissonian fluctuation in density from the uniform model starts to grow: parts of the cluster with more mass initially attract more stars, forming clumps, clumps merge, spontaneously building substructure. These clumps will be analyzed in another section. If the system is bound, the expansion stops at some point, the apex, at which the initial kinetic energy has been spent and converted to potential energy: the cluster is now larger, substructured and subvirial, about to collapse. The apex time t_a of the end of the expansion and the critical value of H_0 can be derived from Newton's second law applied to an expanding spherical shell of matter.

We start from a uniform sphere of radius R_0 , total mass M . We consider spherical shells as mass elements, situated at distance r from the origin. As previously said, they are attributed a radial velocity following (for the shell at $r = R_0$) $\mathbf{v}_0 = H_0 \mathbf{R}_0 = H_0 R_0 \mathbf{u}_r$. We want to follow the radial motion of the last shell of mass m , situated at R from the origin. Newton's second law gives:

$$m \frac{dv}{dt} = -\frac{GMm}{R^2} \quad (2.9)$$

By multiplying on both sides by v and integrating between a given time and $t = 0$, one finds

$$v^2(t) - v_0^2 = 2GM \left(\frac{1}{R} - \frac{1}{R_0} \right). \quad (2.10)$$

We take $\nu = v/v_0$, $x = R/R_0$ and define:

$$E_* = \frac{2GM}{R_0 v_0^2} \quad (2.11)$$

which is a dimensionless measure of the total energy of the system. It comes

$$\nu^2 = 1 + E_* \left(\frac{1}{x} - 1 \right). \quad (2.12)$$

The evolution of the system has 3 outcomes, depending on the value of E_* :

- $E_* < 1$ The velocity is always strictly positive as the system expands ($x- > \infty$). The system is unbound.
- $E_* = 1$ The velocity approaches zero as the system expands. The expansion "stops at an infinite radius". The system is marginally bound.
- $E_* > 1$ The velocity reaches zero for a finite radius, the system is bound and will collapses back on itself once the expansion stops.

Using Hénon units, $G = 1$ and $M = 1$, and we choose $R_0=1$. Which gives a critical value E_* to have a bound system: $E_* = \frac{2}{H_0^2} < 1$. This means to have a bound system, which stops expanding at some point, one must have $H_0 < \sqrt{2}$. We only consider in the following the case in which $E_* < 1$. We have the expression

$$\nu = \sqrt{1 + E_* \left(\frac{1}{x} - 1 \right)} \quad (2.13)$$

which, when derived over time gives

$$\frac{d\nu}{dt} = -\frac{E_*}{2x^2} \left[1 + E_* \left(\frac{1}{x} - 1 \right) \right]^{-\frac{1}{2}} \frac{dx}{dt}. \quad (2.14)$$

Combining this with (2.9), one obtains

$$\frac{dx}{dt} = H_0 \sqrt{1 + E_* \left(\frac{1}{x} - 1 \right)} \quad (2.15)$$

which can be rewritten, using $\tilde{H}_0 = H_0\sqrt{E_* - 1}$ and $x_t = \frac{E_*}{E_* - 1}$,

$$\frac{dx}{dt} = \tilde{H}_0 \sqrt{\frac{x_t}{x} - 1}, \quad (2.16)$$

x_a being the extent of the maximum expansion as we assumed a bound system. The subscript a is for apex. If we choose the notation $u = \frac{x}{x_a}$:

$$\sqrt{\frac{u}{u-1}} \frac{du}{dt} = \frac{\tilde{H}_0}{x_a} \quad (2.17)$$

We know that x varies from 1 to x_a , thus u varies from $1/x_a$ to 1. We can then make the change of variable $u = \sin^2 \theta$ and separate the variables to get

$$\sqrt{\frac{\sin^2 \theta}{1 - \sin^2 \theta}} 2 \sin \theta \cos \theta d\theta = \frac{\tilde{H}_0}{x_a} dt \quad (2.18)$$

which becomes after simplifications

$$[1 - \cos(2\theta)] d\theta = \frac{\tilde{H}_0}{x_a} dt. \quad (2.19)$$

We now integrate the expression from $t = 0$ to t , the time at which the expansion stops and x reaches x_a (wich implies $u_a = 1$ and $\theta_a = \pi/2$):

$$\int_{\theta_0}^{\pi/2} [1 - \cos(2\theta)] d\theta = \int_0^t \frac{\tilde{H}_0}{x_a} dt \quad (2.20)$$

$$\frac{\pi}{2} - \theta_0 + \frac{\sin(2\theta_0)}{2} = \frac{\tilde{H}_0}{x_a} t \quad (2.21)$$

$$\pi - 2\theta_0 + \frac{2}{\sqrt{x_a}} \sqrt{1 - \frac{1}{x_a}} = 2 \frac{\tilde{H}_0}{x_a} t \quad (2.22)$$

which boils down to the expression of the time at which the expansion stops:

$$t_a = \frac{E_* \left(\frac{\pi}{2} - \theta_0 \right) + \sqrt{E_* - 1}}{H_0(E_* - 1)^{-\frac{3}{2}}}. \quad (2.23)$$

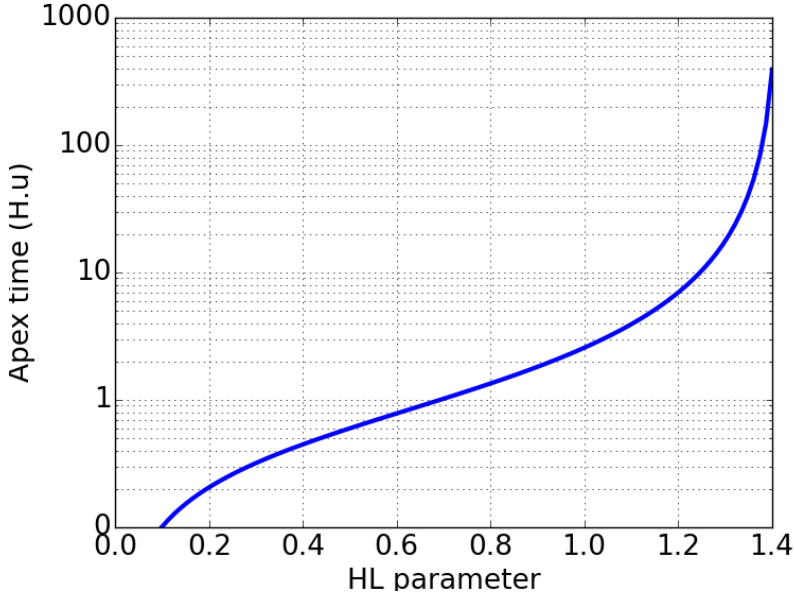


Figure 2.1: Theoretical values of the apex time, at which the system stops expanding, as a function of initial HL parameter, which tunes the strength of the initial expansion.

Recalling the quantities:

$$E_* = \frac{2GM}{R_0 v_0^2}; \quad x_a = \frac{E_*}{E_* - 1}, \quad \theta_0 = \sin^{-1} \left(\frac{1}{\sqrt{x_a}} \right) \quad (2.24)$$

See figure 2.1 for the value of t_a as a function of H_0

2.2 The growth of overdensities: analytical study

2.2.1 Working equations

During the expansion and in the mean-field approximation, the mass inside any shell of radius $r(t)$ is conserved as they move outwards. The position of a mass element is known in parametric form from a rescaling of its initial coordinates and we may write

$$\mathbf{r}(t) = a(t)\mathbf{x} \quad (2.25)$$

$$\mathbf{v}(t) = \dot{a}\mathbf{x} + a\dot{\mathbf{x}} = H(t)\mathbf{r} \quad (2.26)$$

where \mathbf{x} is a co-moving coordinate of position, and $a(t)$ is a dimensionless function of time. The flow is homological and no shell-crossing takes place. It is convenient to introduce a dimensionless time τ such that

$$t = \frac{\tau}{H_0}. \quad (2.27)$$

We then have from equation (2.19):

$$\left[\frac{E_*}{E_* - 1} \right]^{\frac{3}{2}} [2\theta - \sin 2\theta] \Big|_{\theta_0}^{\theta} = 2\sqrt{E_*}\tau \quad (2.28)$$

Table 2.1: Summary of main variables.

E	Total system energy
E_*	Dimensionless total energy
W	Total potential energy
E_k	Total kinetic energy
\mathcal{M}	Total system mass
R_o	Initial bouding radius
H_0	Initial Hubble parameter
v_o	Initial velocity at bounding radius
H	Variable Hubble parameter
τ	Dimensionless time
x	Comoving spatial coordinate
$a(t)$	Rescaling function
θ	Calculation angle
$\nu(\tau)$	Dimensionless velocity $1 + E_*(1/a(\tau) - 1)$
ξ	Radial displacement from comoving
$\delta\rho, \delta M, \delta\rho$	Perturbed quantities
$\mu(\tau)$	Central point mass
η	Peculiar velocity $d\xi/dt$

with

$$a(t) \equiv \frac{\sin^2 \theta(\tau)}{\sin^2 \theta_o} \quad (2.29)$$

The dimensionless energy parameter E_* satisfies $E_* > 1$ for bound systems. The origin of time $\tau = 0$ coincides with the angle θ_o found from solving $\sin^2 \theta_o = (E_* - 1)/E_*$. The solution (2.28) provides the time-sequence for the position and velocity of any shell $0 < x < R_o$ as parametric functions of τ :

$$v(t) = H_0 x \sqrt{1 + E_* \left(\frac{1}{a(\tau)} - 1 \right)} = H_0 x \nu(\tau) \quad (2.30a)$$

$$H(t) = H_0 \frac{\nu(\tau)}{a(\tau)} \quad (2.30b)$$

$$\rho(t) = \frac{3\mathcal{M}}{4\pi R_o^3} \frac{1}{a^3(\tau)} . \quad (2.30c)$$

2.2.2 Linear density perturbation

An actual Hubble-Lemaître model will develop 3-dimensional clumps during the expansion, but to get an analytic view of this process, it is necessary to fall back on one dimension. This will shed light on the growth of clumps and help understand general trends in the system.

We follow radial density perturbations in the expanding uniform sphere described by equations (2.28) and (2.29), as the local density increase also gauges the rise in velocity dispersion. A simplified calculation for radial modes of perturbation in the linear approximation will be derived here, with the goal to determine when the clumps become mostly self-gravitating. A more detailed analysis can be found in the classic work by [Friedman & Schutz \(1978\)](#), [Peebles \(1980\)](#) and [Aarseth, Lin & Papaloizou \(1988\)](#).

We introduce a Lagrangian perturbation in the position of a shell of constant mass by substituting $\mathbf{x} \rightarrow \mathbf{x} + \boldsymbol{\xi}(\mathbf{x}, t)$ and we set $\boldsymbol{\xi} = \xi \mathbf{u}_r$ for a radial displacement. Starting from the continuity equation, a linear treatment yields an expression for the perturbed density.

$$\frac{\partial \rho}{\partial t} + \nabla(\rho \mathbf{v}) = 0 \quad (2.31)$$

which transforms into

$$\delta\rho + \nabla(\rho \mathbf{v} \delta t) = 0. \quad (2.32)$$

We make use of the equivalence:

$$\frac{\partial}{\partial r} \equiv \frac{1}{a} \frac{\partial}{\partial x} \quad (2.33)$$

to obtain, considering $\mathbf{v}\delta t = \delta \mathbf{r} = a(\tau)\boldsymbol{\xi}$ and ignoring second order terms from $\delta\rho$:

$$\delta\rho = -\nabla \cdot (a\rho\xi) = -\rho(\tau) \frac{1}{x^2} \frac{\partial}{\partial x} (x^2 \xi) \quad (2.34)$$

which leads to a perturbation in the mass integrated up to radius r

$$\delta M(< r) = \delta \left(\rho \frac{4}{3} \pi r^3 \right) \quad (2.35)$$

$$= -4\pi a^3(\tau) \rho x^2 \xi. \quad (2.36)$$

Poisson's equation in spherical symmetry gives the perturbed potential

$$\frac{1}{r^2} \frac{\partial}{\partial r} r^2 \frac{\partial}{\partial r} \delta\phi = \frac{1}{a^2} \frac{1}{x^2} \frac{\partial}{\partial x} x^2 \frac{\partial}{\partial x} \delta\phi = 4\pi G \delta\rho. \quad (2.37)$$

Substituting for $\delta\rho$ from (2.34) in (2.37), and using (2.33), we obtain:

$$\frac{\partial}{\partial x} \left(x^2 \frac{\partial \delta\phi}{\partial x} \right) = -4\pi a^2 G \rho_0 \frac{\partial}{\partial x} (x^2 \xi). \quad (2.38)$$

Integrating once, we obtain the general solution

$$a(\tau) \nabla \delta\phi = \frac{3G\mathcal{M}}{R_o^3} \left(-\xi + R_o^3 \frac{\mu(\tau)}{x^2} \right) \quad (2.39)$$

where μ stands for a central point mass. A point mass would form by shell crossing at the center of coordinates. In an expanding system, shell crossing at the center is unlikely. For that reason, we make $\mu = 0$ in the remainder of this paper.

The equations of motion at co-moving radius $x + \xi(x, t)$ can be expanded to first order in ξ ; identifying terms of the same order we obtain (with $\partial/\partial x = \nabla_x$)

$$a(\tau) \frac{d^2}{dt^2} \xi + 2\dot{a}(\tau) \frac{d}{dt} \xi = -\nabla \delta\phi - \xi \nabla_x \nabla \phi - \ddot{a}(\tau) \xi. \quad (2.40)$$

The second and third terms on the right-hand side cancel out exactly ; the first is known from (2.39). It is standard practice to demote this second-order dynamical equation to a set of first order equations ; for convenience we use the initial system radius R_o as unit of length, and we introduce starred (*) dimensionless variables. We then have $x = R_o x_*$, $\xi = R_o \xi_*$, and so on. After simplification using the dimensionless functions of τ defined in (2.27) and recalling that $\dot{a}(\tau) = H(\tau)$, the differential equations read

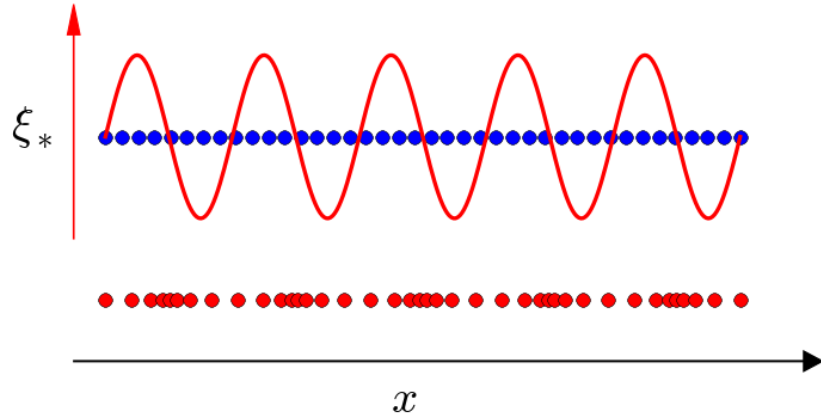


Figure 2.2: Schematic illustration of a sinewave density perturbation (red line) applied to an uniform distribution of matter (blue dots) and the resulting distribution (red dots). The mode displayed here has $m = 10$ and its amplitude was exaggerated.

$$\frac{d}{d\tau} \xi_* = \eta_*(\tau) \quad (2.41a)$$

$$\frac{d}{d\tau} \eta_* = \frac{3E_*}{a(\tau)^2} \xi_* - 2 \frac{H(\tau)}{a(\tau)} \eta_* \quad (2.41b)$$

where we have introduced the peculiar velocity $\eta \equiv d\xi/dt = H_0 R_o \eta_*$.

2.2.3 Consistent initial conditions

Initial conditions

Equations (2.41) can be numerically integrated with an explicit integration scheme once the initial values R_o , H_0 , \mathcal{M} and $\xi_*(0)$ are specified and values of $a(\tau)$ are obtained from (2.29) and (2.28). All functions of the dimensionless time τ are set to unity except that $\eta_*(0) = 0$. The solution is shown in the next section, on Fig 2.3a.

The Hubble parameter $H(\tau) \rightarrow 0$ when the system reaches a maximum radius $a(\tau)R_o$ ($\theta[\tau] = \pi/2$ in Eq. 2.29). Around that time, equation (2.41b) transforms so the Lagrangian displacement ξ_* grows exponentially, and the clumps become the densest. We investigate the growth of a density perturbation as a Fourier fragmentation mode before that. In the linear regime, such a mode is decoupled from all the others. We pick

$$\xi_*(x, 0) = \xi_*^{(o)} \sin(kx), \quad (2.42)$$

where the wavenumber k is such that $kR_o = m\pi$ and $\xi_*(R_o, 0) = \xi_*(R_o, \tau) = 0$ at all times. When deciding which wavenumber to choose, we must bear in mind the finite numerical resolution of the models that we will present later. The next subsection gives quantitative arguments that motivated our choices. The aspect of the perturbed system is shown as a rough schematic on Fig 2.2.

Fourier modes: resolution issues

An uniform distribution of N discrete mass elements cannot resolve infinitely small wavelengths, the lower limit depends on the mean separation $l_o \simeq R_o/N^{1/3}$ which gives a reference wavelength $\lambda/R_o = \lambda_* \geq N^{-1/3}$ for a resolved Fourier mode. Since $kR_o = m\pi$, this also implies that $m \leq 2N^{1/3}$.

The initial amplitude $\xi_*^{(o)}$ of the perturbation can be tailored to the actual Poissonian fluctuations in a uniform distribution of discrete elements. The radius bounding a shell of N mass elements distributed randomly will fluctuate freely between r , $r + \delta r$ due to stochasticity. The radius r of a uniform sphere being a power-law of mass M , we find:

$$\frac{\delta r}{r} = \frac{1}{3} \frac{\delta M}{M} = \frac{1}{3} \frac{\delta N}{N} = \frac{1}{3} N^{-\frac{1}{2}} \quad (2.43)$$

for identical mass elements. We then compute the number-averaged value $\langle \delta r/r \rangle$ by summing over all elements from 1 to N and dividing by $N - 1$ to find

$$\langle \frac{\delta r}{r} \rangle = \langle \xi_*^{(o)} \rangle = \frac{2}{3} \frac{\sqrt{N} - 1}{N - 1}. \quad (2.44)$$

Thus the mean amplitude (in units of R_o) is $\langle \xi_*^{(o)} \rangle \simeq 1/10$ for $N = 32$ which drops to $\langle \xi_*^{(o)} \rangle \simeq 6 \times 10^{-4}$ when $N = 10^6$. We checked that the mode with the shortest wavelength λ_* still resolved would have a displacement $\langle \xi_*^{(o)} \rangle$ initially smaller than $\lambda_*/2$ for any sensible value of N . This in turn implies that this mode may grow over time to reach an amplitude $\xi_*(x, \tau) \simeq \lambda_*/2$, which is the point when orbit-crossing between shells of constant mass must occur. In other words, at this point, the overdensity transitions from linear convergence of particles to collisional evolution (not covered by Eqs. 2.41). The time when shell-crossing occurs can be seen as the "birth" of a clump, whether this clumps undergoes consequent two-body relaxation effects depends on its characteristics, such as density and membership, and the remaining time before the end of expansion.

2.2.4 Segregation time-scale

We already noted that H_0^{-1} sets a time-scale for the expansion of the system. That time should be chosen so that it matches the hydrodynamical star formation phase of 0.5 – 1 Myr (Maschberger & Clarke, 2011; Bate, Tricco & Price, 2014). When $H(\tau) = 0$ and the expansion is over, the stars relax to a new equilibrium driven by star-star interactions. Therefore we need to address first the internal dynamics in clumps in time units of H_0^{-1} , before discussing the later phase of violent relaxation and consider the system as a whole. The definitions are the same, only the face values change between the two phases of evolution.

Let us consider a clump of membership N_λ initiated by a Fourier mode of wavelength λ . With its total density $\rho + \delta\rho$ given by Eq. (2.34), we may write

$$\rho_g = \frac{\rho_o}{a^3(\tau)} \left(1 + \frac{\delta\rho}{\rho} \right) \equiv \frac{\rho_o}{a^3(\tau)} \rho_*. \quad (2.45)$$

Combining this with Eqs. (1.5), (1.6) and (1.10) from the introduction, the mass-segregation timescale in the clump now reads:

$$t_{ms} = \frac{0.138}{6} \pi \left(\frac{3}{4\pi} \right)^{1/2} \frac{\langle m_* \rangle}{\max\{m_*\}} \frac{N_\lambda}{\ln 0.4 N_\lambda} (G\rho_g)^{-\frac{1}{2}}. \quad (2.46)$$

Making use of the equality

$$\frac{4\pi}{3} G\rho_o = H_0^2 E_*, \quad (2.47)$$

the last three relations simplify to the expression of the new dimensionless mass-segregation timescale:

$$\tau_{ms} = H_0 t_{ms} = \frac{0.138}{6} \pi \frac{a_\lambda^{3/2}}{(\rho_* E_*)^{1/2}} \frac{\langle m_* \rangle}{\max\{m_*\}} \frac{N_\lambda}{\ln 0.4 N_\lambda} \quad (2.48)$$

where a_λ refers to the expansion factor $a(\tau)$ evaluated at time τ when $\xi_* \simeq \lambda_*/2$. Note that our use of Eq. (2.34) to compute ρ_g means that the gravitational radius r_g does not have its usual definition based on the gravitational energy W of the system. Linking ρ_g to R_g in this way has the advantage that R_g is not derived from an implied mass profile, which is (by definition) not resolved here.

Clearly the segregation time depends strongly on the mass spectrum of individual clumps, on their membership N_λ , as well as the density contrast $\rho_*(\tau_\lambda)$. We find the density contrast from (2.42) and (2.34),

$$\frac{\delta\rho}{\rho}\Big|_{\tau=0} = -\frac{1}{x^2}\frac{\partial}{\partial x^2}x^2\xi = -\left(2\frac{\sin m\pi x_*}{m\pi x_*} + \cos m\pi x_*\right)m\pi\xi_*^{(o)}$$

which admits an upper-bound of $3m\pi\xi_*^{(o)}$. In the course of evolution, the initial amplitude of perturbation grows to $\xi_* = \lambda_*/2$ so that the density contrast peaks at

$$\rho_* = 1 + \frac{\delta\rho}{\rho} = 1 + 3m\pi\lambda_*/2 = 1 + 3\pi, \quad (2.49)$$

where the last substitution follows from the definition of the integer m . The mass M_λ in a shell bounded by $r, r+\lambda$, is known from the unperturbed density profile ; in terms of the total system mass \mathcal{M} , we find

$$\frac{M_\lambda}{\mathcal{M}} = (\overline{3x_*^2} + \lambda_*^2/4)\lambda_* = (1 + \lambda_*^2/4)\lambda_*, \quad (2.50)$$

where we have replaced $3x_*^2$ by its space-averaged value in the last step. Eq. (2.50) provides an estimate of bound mass of a clump formed through the growth of a radial perturbation mode. If all the stars have equal masses, or, if the stellar mass function is symmetric with respect to the mean value $\langle m_* \rangle$, the ratio of the number N_λ of stars in the clump to the total number N is in the same proportion as $\frac{M_\lambda}{\mathcal{M}}$. We find an estimate for N_λ which reads

$$N_\lambda = N \left(1 + \frac{\lambda_*^2}{4}\right) \lambda_*. \quad (2.51)$$

We argued in §2.3.2 that a resolved mode should have $\lambda_* \geq N^{-1/3}$, which translates as:

$$N_\lambda > N^{2/3} \left(1 + \frac{N^{-2/3}}{4}\right). \quad (2.52)$$

This number inserted into Eq.(2.48) leads to a rough picture of the segregation process in clumps. The rate of mass segregation leans on the choice of initial value for the expansion phase, H_0 . In the limit when $H_0 = 0$, there is no expansion whatsoever, and the clumps form unsegregated (aside from random associations when attributing positions and velocities to the stars) during global infall. If by contrast, the expansion is vigorous, $a_\lambda \gg 1$, and the segregation timescale remains large. For $N \sim 10^4$, we compute from (2.52) $N_\lambda \gtrsim 464$: a clump with that many stars will mass-segregate rapidly only if its stellar mass function includes very massive stars. We note that one-dimensional (radial) modes would in fact split into several smaller fragments in a three-dimensional calculation.¹ We expect the clumps to form quickly and contain $N_\lambda \ll 464$ stars, so that the internal dynamics will drive mass segregation *before* the system expansion stops. Because this depends in the details on H_0 and other important parameters, we defer the analysis to §?? and N-body simulations.

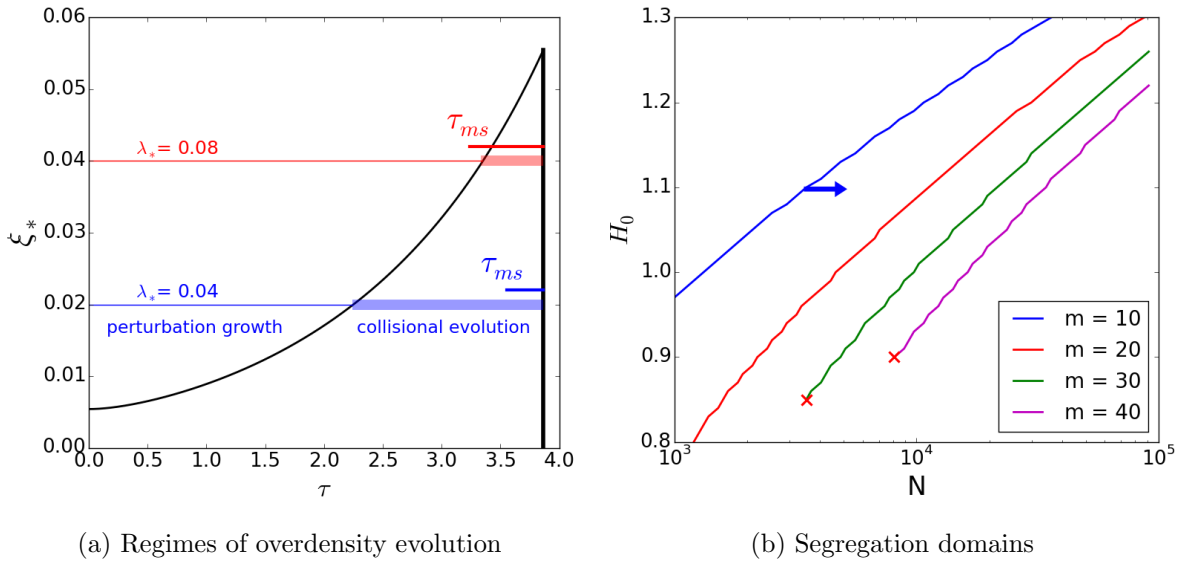


Figure 2.3: (a): growth of perturbation ξ_* over dimensionless time τ until the end of expansion at $\tau = 3.84$. An overdensity seeded with a wavelength λ_* begins its collisional evolution when ξ_* reaches $\frac{\lambda_*}{2}$. These regimes are illustrated for $\lambda_* = 0.04$ and $\lambda_* = 0.08$. The overdensities have to evolve collisionally for at least τ_{ms} to mass-segregate. This time-scale is also shown for each case. The blue case evolve collisionally for several τ_{ms} and will end up mass-segregated, while the red case visibly don't have have time to segregate. Modes of large wavelength tend to produce less mass-segregated clumps. (b) for a given number of nodes m , a model on the right of the corresponding line (arrow for $m = 10$) will have mass-segregated overdensities at the end of the expansion, will on the left, the collisional evolution is too short for segregation to sets in. The red crosses show the minimum N below which the modes cannot be resolved.

2.2.5 Example with $N = 15000$

We now make use of all previous development to follow the evolution of a perturbation in a given system and assess its dynamical state.

To ease comparisons with N-body calculations cast in standard Hénon units, we set $\mathcal{M} = G = R_o = 1$ and use $H_0 = 1.0833.. \simeq 1$ so that the total binding energy $E = -1/4$, which gives a value of $E_* \simeq 6/7$. The Hubble expansion proceeds until a time $t = \tau/H_0 \simeq 3.87/H_0$, when $H = 0$ and the bounding radius R reaches $R = a(\tau)R_o \simeq 2.4R_o$. The evolution time up to that point coincides almost exactly with the *current* global system free-fall time of ≈ 4.1 time units. System-wide collapse to the barycentre will ensue on the same time-scale, but now this process will involve the merging / scattering of several high-density clumps.

For simplicity, and for ease of calculations, we chose the mass of individual stars to follow a truncated [Salpeter \(1955\)](#) distribution function, where the distribution function $dN/dm \propto m_\star^{-\alpha}$ with index $\alpha = 2.35$ for masses in the range $0.3M_\odot < m_\star < 100M_\odot$ giving a mean value of $\simeq 1M_\odot$.

We set $H_0 = 1$ and $N = 15000$ as reference². We compute a mean initial amplitude of perturbation $\xi_*^{(o)} \approx 0.005$ with a shortest-resolved wavelength $\lambda_* \approx 0.04$. Fig. 2.3a displays the solution from integrating Eqs. (2.41). The amplitude $\xi_*(\tau)$ grows monotonically and crosses the values $\lambda_*/2$ at $\tau \approx 2.3$: thereafter the perturbation enters a non-linear regime of evolution during which the internal dynamics may become collisional ($\Delta\tau > \tau_{ms}$). A second case is depicted on Fig. 2.3a, where the wavelength $\lambda_* = 0.08$ and the perturbation reaches amplitude $\xi_* = \lambda_*/2$ at $\tau \approx 3.6$: there is then too little time left before the end of the Hubble expansion phase for a clump of stars to evolve collisionally ($\Delta\tau < \tau_{ms}$).

The dynamical state of individual clumps is clearly a question of membership N_λ and mass spectrum as shown in (2.48). We have been arguing that most small-size clumps will show collisional internal evolution : a small cluster of stars would lose low-mass stars in the process and so have an increased ratio of average- to maximum stellar mass. It is not clear, then, whether this trend is strong enough to compensate for the (almost) linear dependence on membership.

2.3 Concluding remarks

We presented the procedure to build a Hubble-Lemaître fragmented model. With an appropriate H_0 , below $\sqrt{2}$, the expansion of our model ends at a time we named apex time. We derived its expression as a function of H_0 , as well as the governing equations of the expansion. A perturbation analysis was performed to follow idealized radial overdensities. We expect clumps to undergo a phase of linear convergence followed by collisional evolution. We can also expect mass-segregation to occur in our clumps, though quantitative prediction cannot be obtained from idealized radial shell-like overdensities. N-body simulations are needed to obtain detailed characteristics.

¹ A full-grown radial mode forms a thin shell subject to fragmentation. See *e.g.* [Ehlerova et al. \(1997\)](#); [Wünsch et al. \(2010\)](#).

²The more accurate value is $H_0 = 1 + 1/12 = 1.0833$ but we rounded up to 1 to simplify the discussion

CHAPTER 3

Nbody application

After the previous analytical study, we present here the characteristics of numerically obtained Hubble-Lemaître fragmented models. The integrator NBODY6 and data analysis framework StarFiddle are described, as well as a clump-finding algorithm that we use to analyse the population of clumps obtained from the expansion. The influences of N , H_0 and stellar mass functions on the clumps mass function are investigated. We then look at the stellar content and distribution inside clumps, comparing them to clumps obtained from hydrodynamical simulations.

Contents

3.1 Numerical tools	41
3.1.1 Hénon units	41
3.1.2 NBODY6	43
3.1.3 StarFiddle, an N-body API	43
3.1.4 Clump finding algorithm	45
3.2 Clump mass function	48
3.2.1 Influence of H and N	48
3.2.2 Influence of stellar mass function	52
3.3 Clump contents	54
3.3.1 The velocity field	55
3.3.2 The stellar mass function in clumps	56
3.3.3 Mass segregation	59
3.4 Concluding remarks	60

3.1 Numerical tools

3.1.1 Hénon units

Many N-body integrators use a set of units specifically invented for the Nbody gravitational problem, the Nbody units, or Hénon units (as prescribed by Douglas Heggie during the MODEST 2014 meeting). They were introduced by Hénon (1971) and are based on three relations:

$$G = 1 \tag{3.1}$$

$$M_t = 1 \tag{3.2}$$

$$E = -\frac{1}{4} \tag{3.3}$$

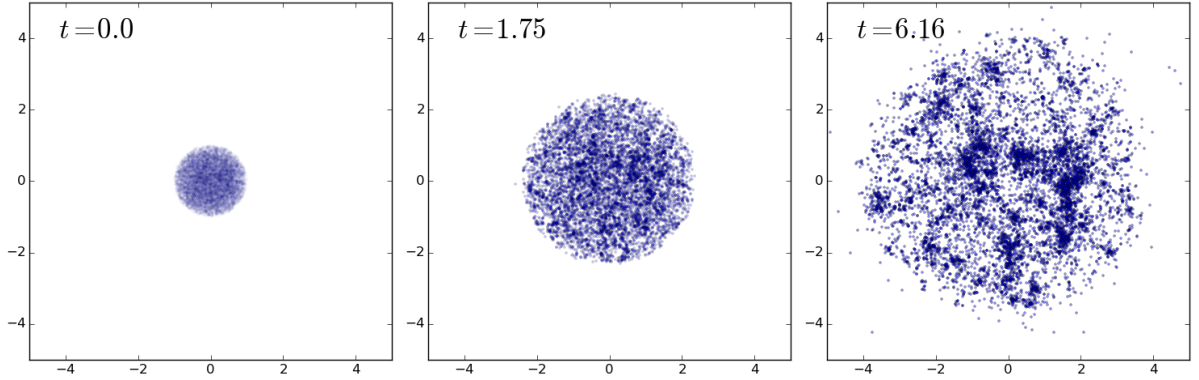


Figure 3.1: Progressive fragmentation through the Hubble expansion. The left panel shows the initial uniform sphere; the middle panel, an intermediate step, slightly fragmented with a slowed down expansion; the right panel is the final stage, when the expansion has stopped and the fragmentation is fully developed. $N=10000$ particles were used in this N-body model, with $H_0 = 1.0$. Time and coordinates are in Hénon units.

With G the gravitational constant, M_t the total mass of the system and E total energy of the system. For a virialized system, that is a relaxed system in which the virial ratio

$$Q = -\frac{E_k}{E_p} = 0.5 \quad (3.4)$$

it comes that $E_k = 0.25$ and $E_p = -0.5$ and, considering the definition of the virial radius

$$R_v = -\frac{GM_t^2}{2E_p} = 1. \quad (3.5)$$

This unit system was designed for virialized systems, but can be used for out of equilibrium systems, as long as they are bound ($Q < 1$), with energy expressions functions of Q

$$E_p = -\frac{1}{4(1-Q)} \quad (3.6)$$

$$E_k = \frac{Q}{4(1-Q)} \quad (3.7)$$

which still fulfills the $E = -\frac{1}{4}$ condition. In practice, the Hénon mass, radius and velocities are obtained through

$$m_h = \frac{m}{M_t} \quad (3.8)$$

$$r_h = 4(1-Q)|E_p| \cdot r \quad (3.9)$$

$$v_h = \sqrt{\frac{Q}{4(1-Q)E_k}} \cdot v \quad (3.10)$$

with E_p and E_k being computed with Hénon masses and $G = 1$ but before rescaling length and velocities. Such a system can be used as an input for NBODY6 without the need for the software to rescale anything, as NBODY6 internally works with Hénon units.

3.1.2 NBODY6

NBODY6 is a N-body integrator, it computes the trajectories in a system of interacting point masses. It is the second youngest iteration of the NBODY family, a suite of N-body integrators created by Sverre Aarseth. It can compute the gravitational interaction between up to 128,000 stars in a collisional fashion, meaning there is no softening of the potential, at any scale. This allows for very close binaries to form and remain in the system. The code preserves the total energy and angular momentum to better than one part in 10^4 for integration over ~ 100 time units.

To achieve its impressive performances, NBODY6 relies on several optimization technique which have been first developed in the 1960s and 1970s, and improved ever since. NBODY1, first of its name, was developed in the early 1960s and based on the idea of force polynomial fitting: to ensure convergence, trajectories were computed by fitting polynomials to forces and obtaining high-order derivatives. Over time, the force fitting was enhanced, and additional techniques were added over the versions: NBODY3, NBODY2, NBODY4, NBODY5 (in that order, see [Aarseth 1999](#) for a summary of the NBODYs development).

NBODY6 was a work-station version of NBODY5 and was first developed throughout the 1990s. It has been enhanced and optimized ever since. It inherited the major features from its NBODY ancestors that made them so successful. They are briefly described here in chronological order of their implementation:

block time-steps ; very early on, particles were attributed individual time-steps, functions of their acceleration. An innovation was to commensurate these time-steps: they could only be reduced by factors of 2, so all particles could easily resynchronise at some point in the simulation;

KS-regularization was introduced to circumvent the large acceleration in close pairs that slowed down integration, it relies on a change of variables for the pair that makes its integration faster, while still factoring perturbing influence from other particles;

Ahmad-Cohen Neighbour scheme ; considering close neighbours and distant particles have distinct dynamical effects, their influence was split into regular and irregular integration, with some level of synchronization;

Hermite integration scheme was introduced as the latest integration scheme in the NBODY codes, it allows to obtain high-order estimates of future positions and velocities with limited computational cost.

Appendix [TODO] contains additional details on these optimization techniques, while a complete description can be found in Sverre Aarseth's book ([Aarseth, 2003b](#)).

While a new generation, NBODY7, was developed to include post-newtonian effects and correctly integrate black hole binary dynamics ([Aarseth, 2003a](#)), the NBODY6 family has been extended into several branches. [Spurzem \(1999\)](#) developped Nbody6++, a parallel version powered by MPI, while ([Nitadori & Aarseth, 2012](#)) developed NBODY6GPU, a GPU-accelerated version. Recently, both versions were merged into a MPI-GPU hybrid NBODY6++-GPU ([Wang et al., 2015](#)). [Renaud, Gieles & Boily \(2011\)](#) and [Renaud & Gieles \(2015\)](#) introduced Nbody6tt, which allows the inclusion of complex tidal fields from large-scale galactic simulations.

In this work, we adopted the widely used "vanilla" version NBODY6, and its GPU accelerated version when the number of particles exceeded 3000 (from several performance tests on our models).

3.1.3 StarFiddle, an N-body API

Over the course of this work, I developed several python interfaces and modules to handle snapshots of N-body simulations. Several C and Cuda libraries were implemented in these

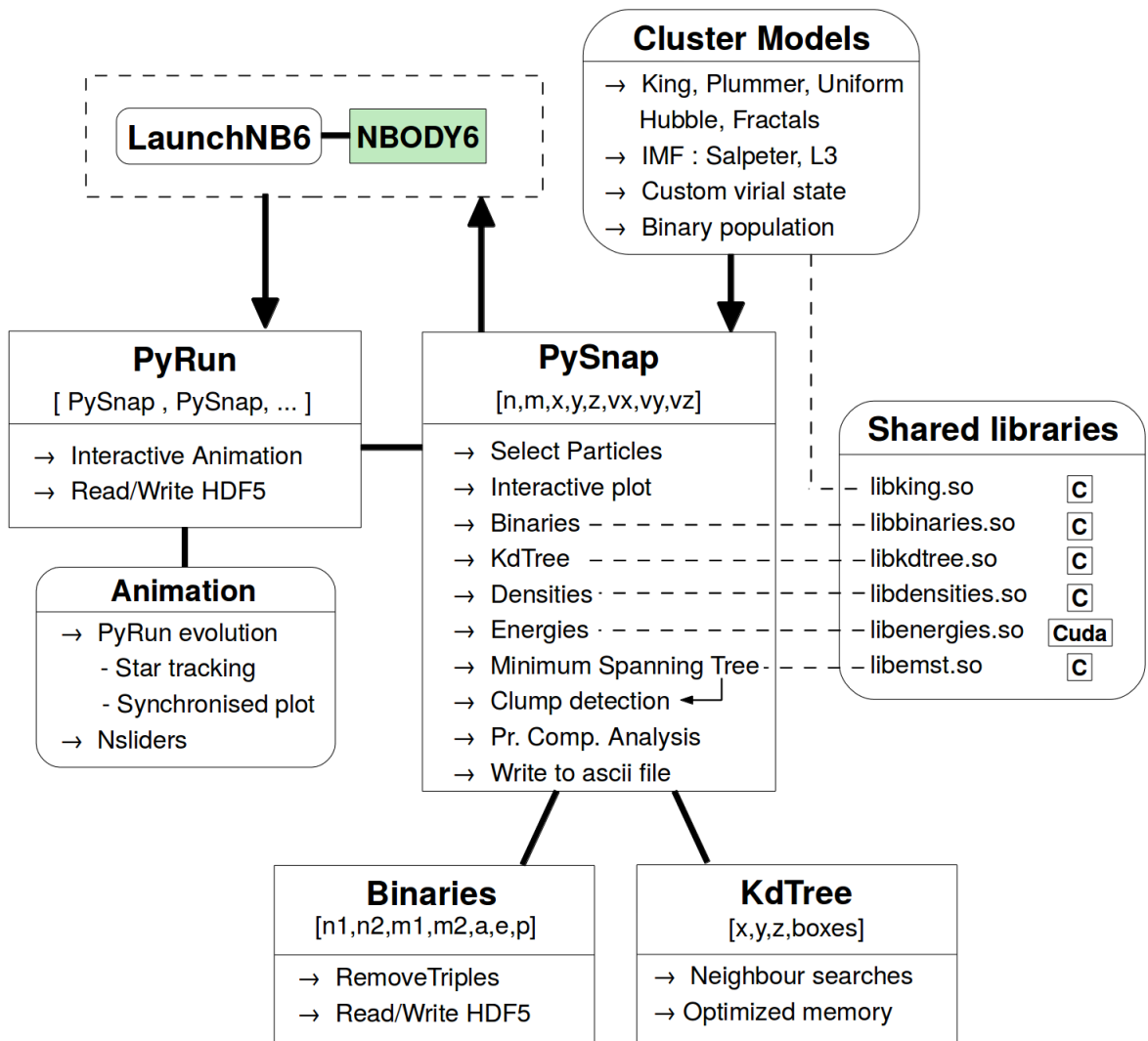


Figure 3.2: Visualization of the StarFiddle API. Squared boxes are data storing classes while rounded boxes are modules.

modules. Finally, all these were unified as a N-body python API called StarFiddle.

StarFiddle is centered around the PySnap class, which stores information about a N-body simulation snapshot: identities of particles (n), masses, position and velocities. This class has a wealth of methods to perform various analysis. The main methods are:

- Interactive Plot - 3d interactive and customizable 3D representation
- SelectParticles - allows boolean selection to produce a PySnap of a subsample;
- Binaries - detect binary stars using the algorithm described in chapter ?;
- kdTree - builds a kdTree of the spatial distribution to perform neighbour searches;
- Densities - computes local densities for each particles through the kdTree
- Energies - computes individual potential and kinetic energies for all particles
- Minimum Spanning Tree - builds the MST of the system, for structure analysis
- Clump detection - extract overdensities through the algorithm described in chapter ?
- Principal Component Analysis - performs a PCA on the system for structure analysis
- Write to file - writes the data to a ASCII file

Computationally intensive algorithms were written in C or Cuda, then compiled into shared libraries. These can be called from C or Python through the ctypes module. The binary, energy and density algorithm were fully written for StarFiddle. The kdTree algorithm was adapted from C++ from [Press et al. \(2007\)](#) to C, and its memory use was optimized; the algorithm was successfully ran on cosmological simulations for 20 million points. The minimum spanning tree was provided by the [MLPACK library](#). Binaries and kdTree are classes of their own which allows easy data storage and management.

The cluster models module lets the user create PySnap instances of various models of star clusters: King, Plummer, Uniform, Fractal or Hubble. The King model uses a C implementation of a fortran algorithm by Gerry Quinlan and Christian Boily. The model can be set to an arbitrary virial parameter Q and injected with a primordial binary population. The stars can have identical masses or follow a Salpeter or L3 Initial Mass Function (**IMF**) with user-provided parameters.

LaunchNB6 is a Python interface for NBODY6. I slightly modified NBODY6 so it prints ASCII snapshot files in place of the regular binary format output. LaunchNB6 creates the specified working directory and launch the integration from initial conditions, either a specific PySnap, or one created from the Cluster Models. It then reads the snapshot files to create a PyRun instance. A PyRun can be stored and retrieved from a HDF5 file. It is strongly related to the Animation module.

The Animation module allows interactive 3D animation of a PyRun and the creation of synchronized plot to follow related data during the evolution. A specified subset of stars can be marked and follow during the animation. In addition to PyRun, Animation lets the user create interactive plots with an arbitrary number of sliders to easily explore a parameter space.

StarFiddle is available on [GitHub](#).

3.1.4 Clump finding algorithm

As seen on Fig 3.1, once expansion stops, the distribution is roughly spherical and visibly clumpy. By clump we mean here a local overdensity of stars. To characterize the model, it is necessary to find and isolate clumps, using an efficient clump-identification algorithm (or, *halo-finding*

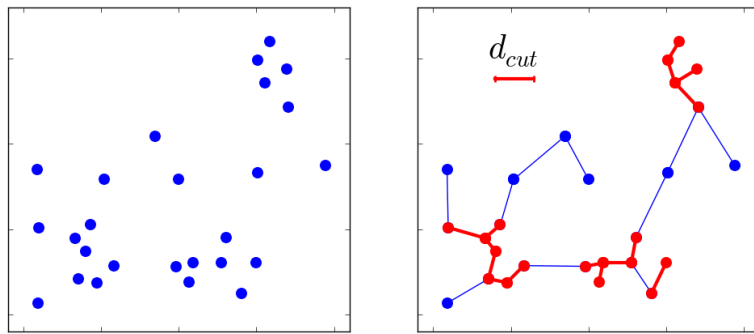


Figure 3.3: Illustration of a Minimum Spanning Tree and its use to isolate subgroups, using a cutting length d_{cut} .

in cosmology). Several methods are commonly used such as the HOP algorithm (Eisenstein & Hut, 1998; Skory et al., 2010) which relies on attributing local densities to each particle and separating the clumps through density thresholds. The HOP algorithm is very robust on large cosmological data sets. However, our calculations have comparatively coarse statistics and noisy density fields. This issue, coupled with the large number of free parameters of the HOP algorithm, makes the method less appealing.

Instead we follow Maschberger et al. (2010) who adapted the minimum spanning tree (MST ; see e.g. Allison et al. 2009b; Olczak, Spurzem & Henning 2011) technique to the detection of clumps. A spanning tree is a set of edges connecting a group of particles without closed loops ; the MST seeks to minimise the total length of the edges. One may then construct the MST for the whole system, and then delete all edges larger than a chosen cutting length, d_{cut} . The sub-sets that are still connected are labeled as clumps. This process is illustrated in Fig 3.3. In practice a minimum sub-set size N_d is also chosen so as to avoid many small-N subgroups : experience led us to choose $N_d = 12$ for the minimum number of stars per clump.

With N_d fixed, the length d_{cut} is then the only free parameter left. There is some freedom in choosing an appropriate value. Maschberger et al. (2010) fixed the value of d_{cut} by visual inspection of clumps. We instead identified clumps in a fragmented system for a range of values for d_{cut} and settled for the value which optimised the number of identifications. This is shown on Fig. 3.4a for the fully-fragmented state of R80h100 (see table 3.1). For small values of d_{cut} , the number of detected clumps at first increases rapidly. The rise is due to the length d_{cut} initially being small compared with the typical volume spawned by N_d or more nearest-neighbours. Beyond a certain value, a transition to another regime occurs, whereby the algorithm starts to connect previously separated clumps, counting them as one. The number of clumps thereafter begins to decrease. The value $d_{cut} \approx 0.023$ H.u optimises the outcome of the clump-search. This is a generic feature of the MST algorithm and we have adopted the same strategy throughout, adapting the value of d_{cut} to the number N of stars used.

Another method to find the critical cutting length was used by Gutermuth et al. (2009); Kirk & Myers (2011). In these works, the authors build the MST, then trace the cumulative distribution function of all edges in the tree. In a clumpy configuration, there are at least two regimes: the "intra-clump" regime, with the majority of small edges, and the "inter-clump" regime with longer, scarcer edges. The intersection of the linear fits to these regimes provide a good cutting length for clump detection. This procedure was applied to our system and gave the same result than the clump count, as shown on Fig 3.4b.

On Fig. 3.5, a sub-set of R80h100 is shown; we have identified stars that belong to clumps with filled symbols. The three panels on that figure are each for a different value of d_{cut} ,

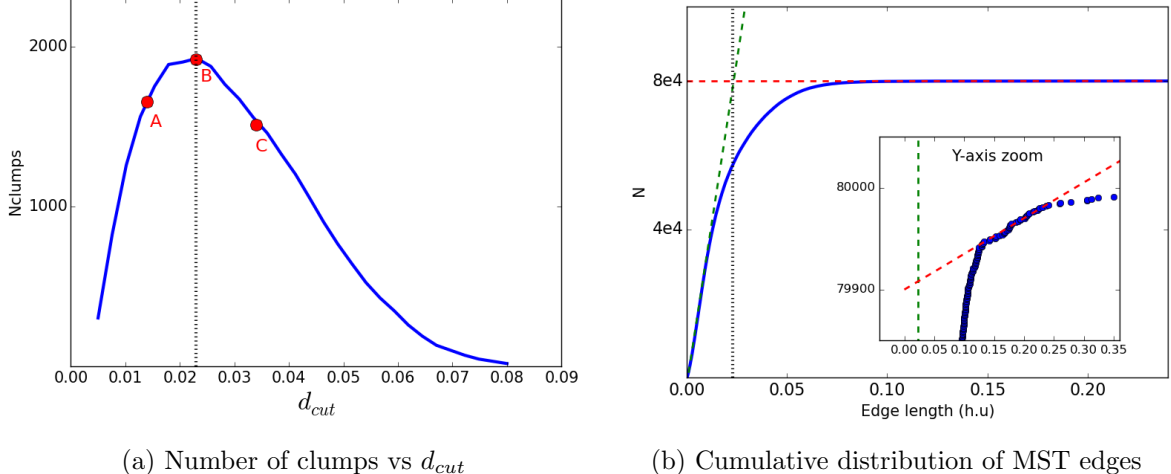


Figure 3.4: Two different methods to identify the critical d_{cut} for clump detection. Both methods give the same value. For this 80k model, the value is 0.023 in Hénon units. The red linear fit on (b) was made on the linear portion with sufficient data points, discarding the seven further points departing from the tendency.

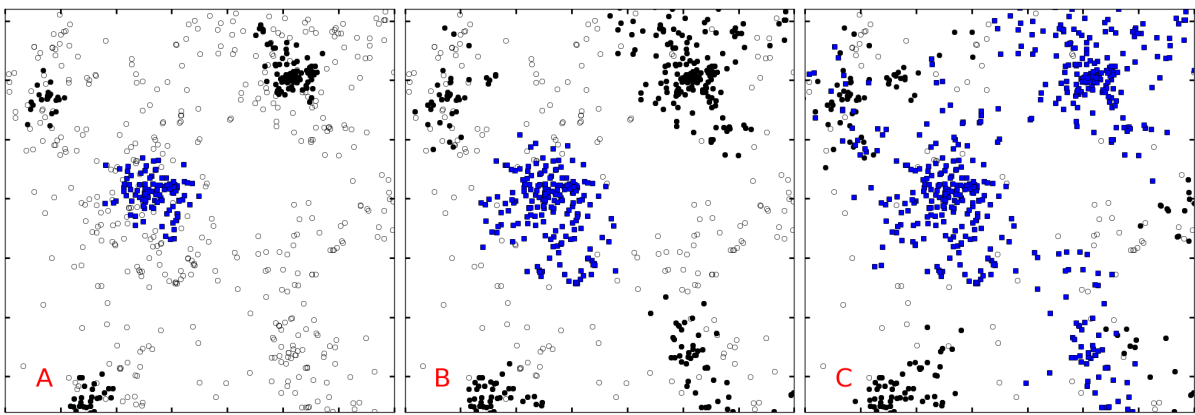


Figure 3.5: Example of detected clumps for three cutting length, 0.014 (top panel), 0.024 (middle panel), 0.034 (bottom panel), which were labeled A,B,C in Fig. 3.4a. A cube within a 80k particles fragmented model was extracted and projected. Empty circles are stars which do not belong to any clump, black circles are clump members, and blue squares are stars that are identified as a single large clump. Tick marks are spaced by 0.05 length units for a box size of 0.35 units.

Table 3.1: Summary of fragmentation models and their characteristics. These simulations, performed with NBODY6, started from an uniform sphere and were stopped at the apex time, t_a , when the expansion halts. The third column shows the number of independent computations for each model. Stars are drawn from an Salpeter distribution with truncation values shown in the fourth column. All mass ranges preserve an average stellar mass of $1M_\odot$. Models that stops at 40 H.u starts from already fragmented configuration. The RunsHN runs are detailed in the two lower tables.

Name	N	Sampling	Mass range	t_{end}	Model
RunsHN	see below	175	[0.3 - 100]	t_a	Hubble
Rmh20	15000	30	[0.35- 20]	t_a	Hubble
Rmh100	15000	30	[0.3 - 100]	t_a	Hubble
Rmh1	15000	60	1.0	t_a	Hubble
R40h20	40000	1	[0.35- 20]	t_a	Hubble
R40h100	40000	1	[0.3 - 100]	t_a	Hubble
R80h100	80000	1	[0.3 - 100]	t_a	Hubble
Rh100	15000	1	[0.3 - 100]	40 H.u	Hubble
Rh20	15000	1	[0.35- 20]	40 H.u	Hubble
Ru100	15000	1	[0.3 - 100]	40 H.u	Uniform
Ru20	15000	1	[0.35- 20]	40 H.u	Uniform

Detailed characteristics of RunsHN:

N	1000	2000	4000	8000	16000
Sampling	12	8	5	5	5

Each RunsHN run is performed with 5 different H_0 .

H_0	0.8	0.9	1.0	1.1	1.2

increasing from top to bottom. For the smallest value $d_{cut}=0.013$ H.u, clumps look somewhat truncated as we are still in the under-sampling regime and only their cores registered as clumps. The second, optimal, value $d_{cut}=0.023$ H.u produces visually well-isolated clumps. Finally, the third and largest value is so that clumps begin to merge together : this is shown by the unique clump identified in the bottom panel (filled blue squares).

3.2 Clump mass function

The numerical realizations of the Hubble-Lemaître model allows to assess the influence of important parameters on the fragmentation, such as H_0 , N and the stellar mass function.

3.2.1 Influence of H and N

We wish to evaluate the influence of H_0 and N on the fragmentation and clump growth. H_0 tunes the strength of the expansion, which tunes the duration of the fragmentation. A stronger initial expansion allows for more time for clumps to grow, so we expect more massive clumps with increasing H_0 . On the other hand, a higher N smooths the spatial distribution, reducing Poisson noise in the distribution. However, a high membership only samples more stars from the same stellar mass function, and the density fluctuations should not change in nature, just

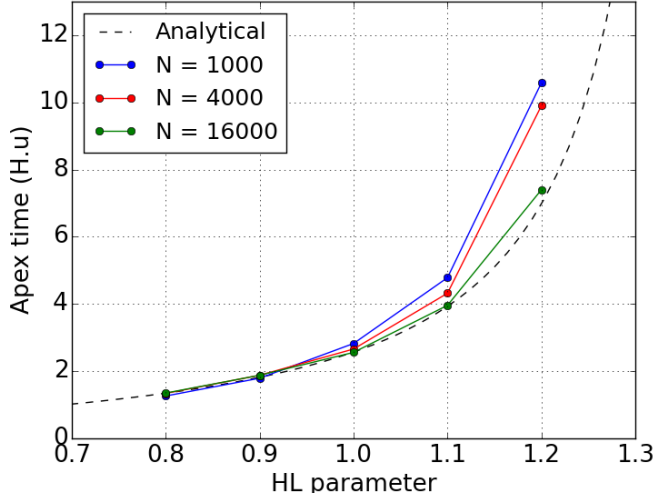


Figure 3.6: Analytical and simulated apex times as a function of H_0 .

scale down with the average distance between stars. We do not expect N to significantly affect the fragmentation in physical units.

To verify these, a set of simulation was performed to explore the mass function of clumps in the H_0 - N parameter space. The models have 5 different memberships that go as powers of 2 in thousands, with an increasing sampling to obtain acceptable statistics. They are summarised in table 3.1 under the name RunsHN.

Apex time

In section 2.1.2, we derived an analytical prediction for the apex time of our expanding models. To compare our numerical realizations to this prediction, we follow for each model the evolution of the half-mass radius over time, then take the apex time as the maximum radius time, when the cluster stops expanding and starts collapsing.

We show on Fig 3.6 the expected analytical curve as a dashed line, then the numerically obtained apex times from our different H_0 and memberships, averaged over all similar runs. The 16k runs follow the analytical expectation within 5%, while lower membership models take more time than expected to stop expanding at high H_0 , overshooting by as much as 30% for $H_0 = 1.2$. Visual inspection of the runs showed that low memberships were more susceptible to have a clump "take over" during the expansion. As we will show in the present section, low- N clusters contains more massive clumps in relative mass than high- N models. When a massive enough clump form during the expansion, it offsets the matter distribution and skews the half-mass radius (computed from the barycenter of the full system) to higher values, offsetting its fall from the collapse. To reduce unwanted "sur-fragmentation" effect, we use analytical apex times to select our fragmented configurations.

Clump mass function

The clump-finding algorithm was ran on the fragmented models to obtain the clump mass function. The results are summarised as histograms on figures 3.7 and 3.8. We have used bins of constant logarithmic intervals. We average the results over each model's sampling, hence the histogram can go down to fractional values.

Looking at the top panels of Fig 3.7, we see the mass function of clumps in *relative* mass, the percentage of total mass they contain. Clumps in small- N systems tends to contain a much

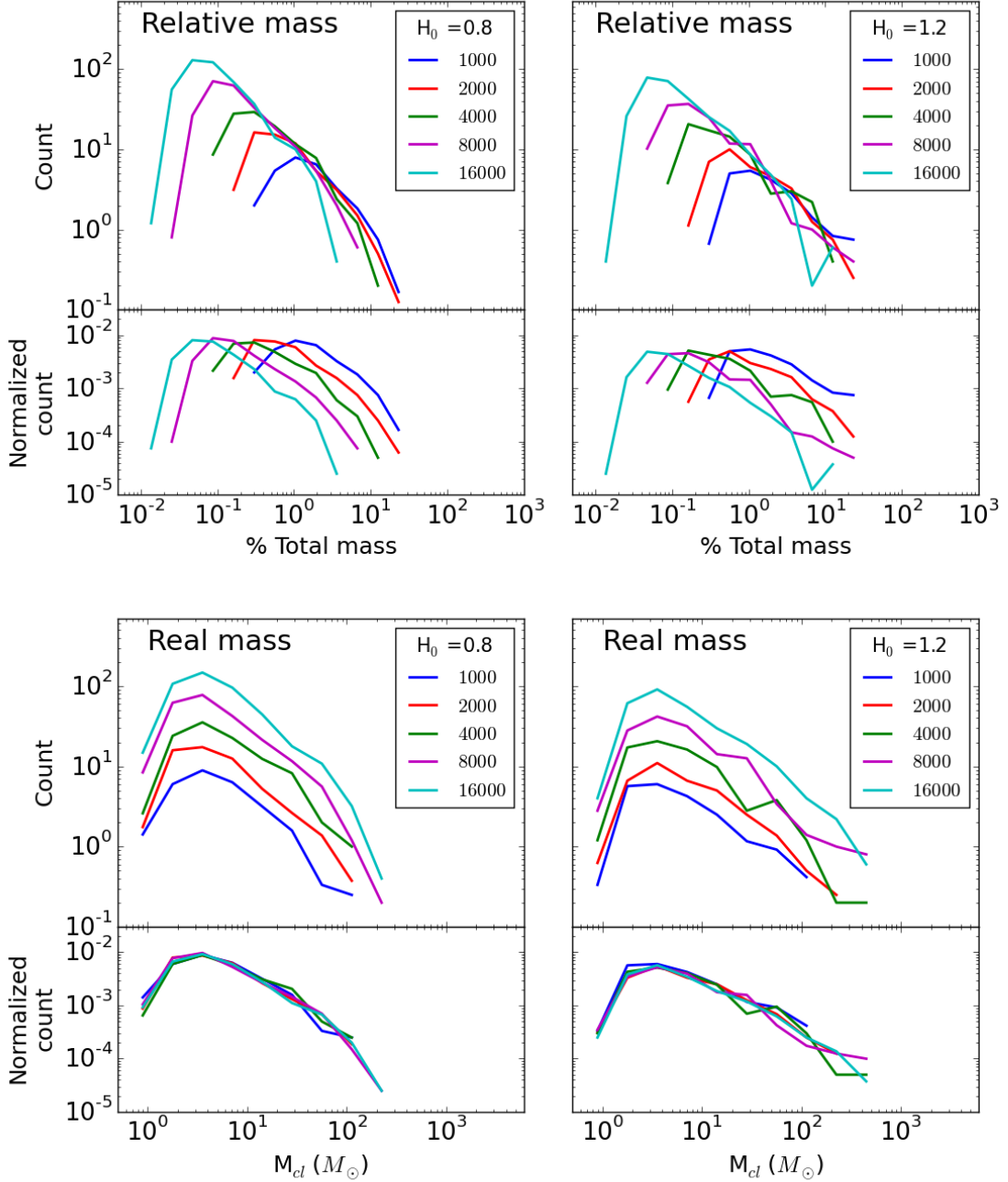


Figure 3.7: Clump mass function for several memberships and two H_0 . Masses in the top panels are in Hénon units, the x-axis was scaled with a factor 100 to get a percentage of the total mass of the system. Bottom panel masses are in physical units. In each panel, top sub-panel shows actual clump count in each bin (averaged over sampling), while bottom sub-panel normalize the count by the model membership.

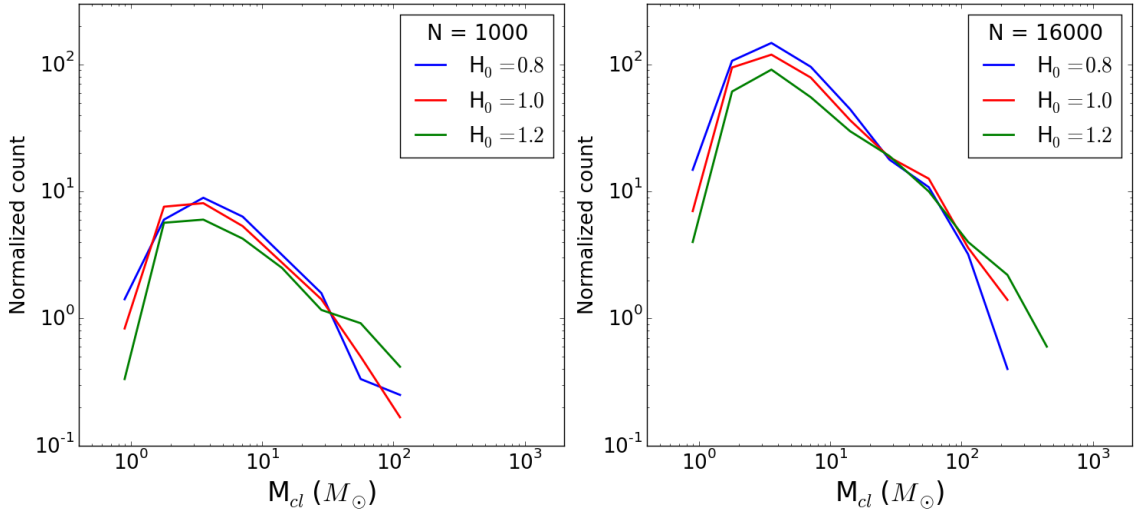


Figure 3.8: Clump mass function (real mass) for several H_0 and two memberships.

larger portion of the total system mass than in large- N systems, which is even clearer in the normalized count sub-panels. In fact, for $H_0 = 0.8$, the peak of the mass function for $N=1k$ happens at 1.1% of total mass, while for $N=16k$, it happens at 0.07%. These values ratio gives ~ 16 , the membership ratio: the clumps relative masses are inversely proportional to the model's membership.

This can be interpreted as a underlying common clump distribution in physical mass, regardless of the total membership of the model. This is confirmed by looking at the bottom panels of Fig 3.7, in which clump distributions are plotted in physical mass, once the masses of stars have been rescaled from Hénon units to match the original stellar mass function. Looking at the normalized count subpanels, it is clear that 1k and 16k models have the same clump distribution, when raw count subpanels show clumps are expectedly more numerous in high- N models. The difference between $H_0 = 0.8$ and 1.2 is not clear from the graph, but it seems a higher H_0 pushes the upper limit of the distribution to slightly higher masses.

To illustrate this last trend, we turn to Fig 3.8 where clump MF are shown for various H_0 and a common membership. For both $N=1k$ and $N=16k$, the distribution preserves its shape for various H_0 , and gets prolonged at higher clump masses for $N=16k$, as more mass is available to build clumps.

Thought the distribution does not undergo any dramatic change, a weak trend with H_0 is seen in both panels: as the strength of expansion increases, the distribution slightly decreases at low clump masses and slightly increases at higher clump masses, the pivot masse being $\sim 30 M_\odot$. We look at the 16k model and follow the cumulated mass inside all clumps, as well as the percentage of this mass in clumps below and above $30 M_\odot$, for different H_0 :

H_0	0.8	0.9	1.0	1.1	1.2
M_{tot}	3502	3478	3582	3683	3561
$< 30 M_\odot (\%)$	66	65	55	49	44
$> 30 M_\odot (\%)$	34	35	45	51	56

From this data, we get two facts about our fragmented models: the mass contained in clumps does not depend on H_0 ($< 2\%$ dispersion) and there is a transfer of mass from small clumps to more massive ones as the expansion lasts longer.

To summarise: the general shape of the clump mass function is common to all membership and H_0 . In physical mass, the same clumps form in 1k and 16k models, almost regardless of

the duration of the expansion. We note a mass transfer from small to high mass clumps when H_0 increases, that is consistent with a merging process: small clumps assemble or get accreted by large clumps. When the initial expansion is strong, the merging lasts longer and more mass is transferred. This is confirmed by visual inspection of the models, as we see clumps merging during the expansion.

3.2.2 Influence of stellar mass function

Neither H_0 or N seem to heavily influence the shape of the clump mass function. We now turn to another parameter: the stellar mass function. We know the clumps are seeded by density fluctuations in the initial uniform sphere. These fluctuations are governed by pure Poisson noise in the case of identical stellar masses, but are modified and enhanced once stars follow a mass function themselves: a high-mass star surrounded by lighter ones will by itself introduce a localized strong density fluctuation. We expect a relation between the clump mass function and the *stellar* mass function in the generated initial conditions.

We wish to quantify this relation. To this end, we ran a set of simulations where all the stars have the same mass, and two sets for which a Salpeter mass function with $\alpha = 2.35$ was truncated at different upper- and lower-bounds. A total of 15000 stars in a Hubble configuration were used, all let go with the same initial expansion rate $H_o = 1$. For the multi-mass models, the mass range was chosen as $[0.3, 100] M_\odot$ and $[0.35, 20] M_\odot$ so that the mean stellar mass $= 1M_\odot$ as for the single-mass models. Thirty different runs were performed in each case and the outcome averaged for better statistics. These are referred to as Rmh1, Rmh100 and Rmh20 in Table 3.1.

On Fig. 3.9, we display the number of clumps as function of clump mass for the truncated Salpeter models as a red solid line, while the single stellar mass models are shown in green dash. A grey shade indicates one standard deviation where statistics allow (*i.e.*, large numbers), and, as in previous section, we have used bins of constant logarithmic mass intervals. Fig. 3.9a shows Rmh20 models, and 3.9b shows Rmh100 models. With clump membership restricted to $N \geq 12$, the identical-mass model stays relatively close to a power law (straight dotted line on the figure) of index ≈ -4 for the higher mass clumps. A spread in stellar masses leads to much more massive clumps (we counted $\simeq 80$ clumps of $12M_\odot$ for the equal-mass case ; and ≈ 32 with a mass $\leq 12M_\odot$ for the other ones) . This transforms the clump mass function, from a near-power-law, to a bell-shaped distribution.

When very massive stars are included in the calculations, yet more massive clumps are formed (Fig. 3.9b). The formation of large sub-structures depletes the number of clumps around the peak value, and so the distribution becomes broader and shallower. The mean clump mass for the different cases read $20M_\odot$ (equal-mass), $32M_\odot$ (Salpeter $m_{max} = 20M_\odot$) and $45M_\odot$ (Salpeter $m_{max} = 100M_\odot$), a steady increase with the width of the stellar mass spectrum. On the other hand, the position of the peak of the distribution remains unchanged at (roughly) 20 to $21M_\odot$. The trend in total number of clumps detected is a slight decrease with the broadening of the stellar mass spectrum, from 187, down to 151 respectively for the $m_{max} = 20$ and $100M_\odot$ Salpeter models. We observe that the overall fraction of stars found in clumps (some ≈ 6500 out of 15000, or 43%) stays unchanged.

We argue that the shape of the clump mass spectrum provides indirect evidence for the role of massive stars predominantly as seeds for growth in our simulation. This is to be opposed to a full hierarchical build-up of clumps from very tiny sub-structures. There are two tell-tale signs to support this view : a) if high-mass clumps formed through the repeated and stochastic merger of small clumps, then the clump mass function should tend to a log-normal distribution, which is symmetric (in logarithmic scales) with respect to the peak value, whereas the distributions shown here lack this basic property ; and b) the ratio of maximum clump mass to mean mass may exceed 15 when the stellar truncation mass is set to $20 M_\odot$, and reaches only ~ 4 in the case when the upper mass is set to $100 M_\odot$. If small-ish clumps were merging at the same

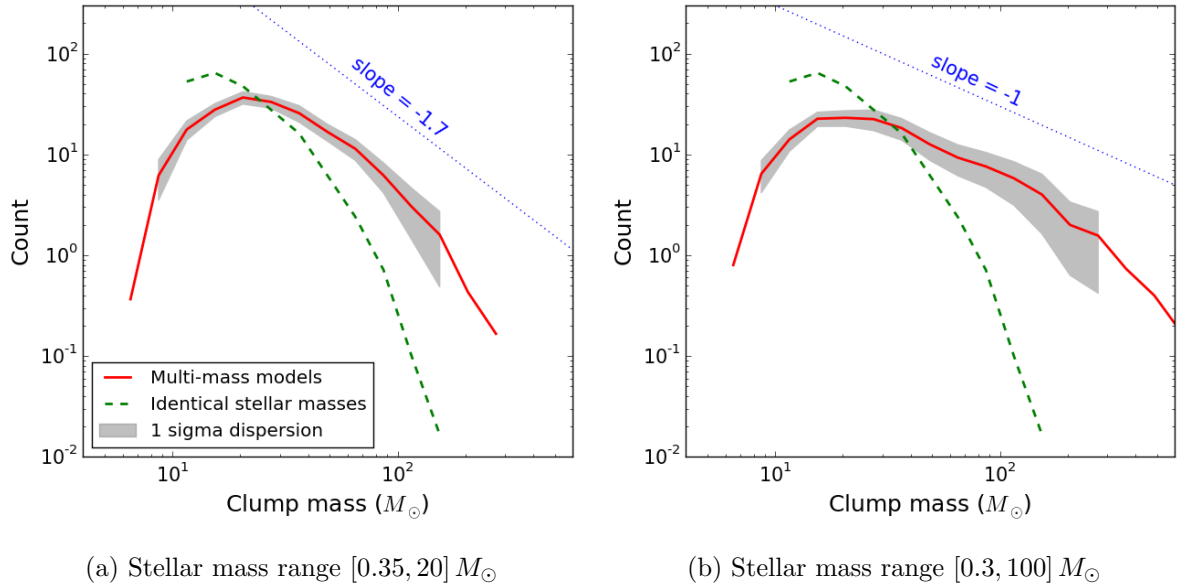


Figure 3.9: Mass function of the clumps identified with the MST algorithm. The calculations all had $N = 15000$ stars, and we have averaged over 30 realisations for each configuration. The results for three stellar mass functions are displayed : a model with equal-mass stars (green dashed line) ; a Salpeter distribution function truncated at $20M_{\odot}$ (solid red line, left) ; a Salpeter distribution function truncated at $100M_{\odot}$ (solid red line, right). (a) The clumps mass function for equal-mass models shows a trend with mass roughly in agreement with an M^{-4} power-law. By comparison, the results for an Salpeter stellar distribution function truncated at $20M_{\odot}$ has a bell-shaped profile, with a peak around $M = 20.5M_{\odot}$; only the tail-end shows marginal agreement with an $\propto M^{-1.7}$ power-law (dotted line on the figure) ; (b) another Salpeter distribution function but with the upper-mass truncation set at $100M_{\odot}$. The tail at large clump mass is now much flatter, with a slope $\approx M^{-1}$, (dotted line on the figure as well). The bins used had constant logarithmic mass intervals.

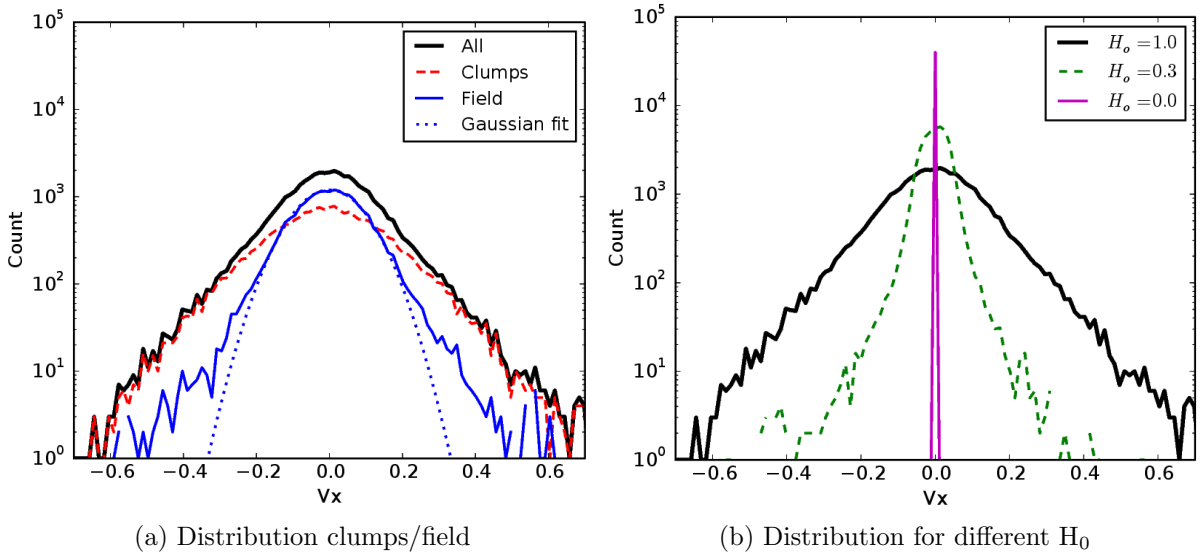


Figure 3.10: (a) Distribution of the one-dimensional velocity field for the whole cluster as the thick solid black line, in the simulation labelled as R40h20 at the apex time ($H=0$). The red dashed distribution matches clump members and thin solid blue the field particles. (b) The distribution for three different values of H_0 : when $H_0=0$, the distribution is a Dirac- δ around $v=0$. The central distribution broadens as H_0 increases to 0.3 and 1. Observe the exponential profiles at large $|v|$. Velocities are in $H.u$

rate in both models, then this ratio should be comparable. Instead, very large clumps take too long to assemble and the merger rate drops with clump mass. Recall that all fragmentation calculations ran for the same total time. There is a weak merging process happening, as shown in the previous section, but it is marginal, as heavy clumps likely form from massive star seeds.

To check this hypothesis, we borrow from black hole dynamics in galactic nuclei the notion of a *radius of influence*, which is the radius enclosing as much mass in the stars as the central black hole mass (see e.g. Merritt 2013). Here, the stars inside the influence radius are bound to the massive star at the centre. Thus if a massive star is a seed for a clump, and only the stars inside the influence radius remain bound to it, we should count as many clumps in the mass range $2m_\star, 2m_\star + 2dm_\star$, as there are stars in the range $m_\star, m_\star + dm_\star$. The maximum clump mass exceeds twice that of the most massive stars m_{max} , which implies some degree of merging and is consistent with the previous section. If we count all clumps starting from the truncation value m_{max} of the stellar mass function, then we should find as many clumps in the mass range above m_{max} , as there are stars in the interval $[m_{max}/2, m_{max}]$. We find for runs with $m_{max} = 20M_\odot$ some 120 clumps more massive than that, when there are $\simeq 100$ stars in the range $[10, 20]M_\odot$, essentially identical ; and some 14 clumps of $100M_\odot$ or more, when there are (on average) 9 stars in the mass range $[50, 100]M_\odot$. This calculation suggests that most massive stars act as seeds for the formation of large clumps in the generated initial conditions.

3.3 Clump contents

In this section we compare the clump configurations derived from the Hubble-Lemaître expansion method with the distribution of proto-stars that form in hydrodynamical simulations. We first look at the velocity field inside and outside the clumps, then we investigate the stellar content of the clumps themselves and their mass segregation.

3.3.1 The velocity field

There is no hydrodynamics in the approach that we have taken, nevertheless expansion under gravity alone is equivalent to the adiabatic expansion of gas : for that case, the first law of thermodynamics equates the drop in internal energy dU to minus the external work, $-pdV$. At constant mass, the change in gravitational energy dW is $-dE_k$, where E_k is the kinetic energy. With $W < 0$ but increasing over time, this implies that E_k drops in amplitude. In the case when the motion is strictly radial, $E_k = 0$ when $H = 0$ and all stars come to rest. We ask to what extent the growth of substructures and non-radial motion off-set the ‘adiabatic cooling’ brought on by expansion.

Fig. 3.10a graphs the x-axis one-dimensional velocity distribution for the R40h100 model. The left-hand panel displays the overall distribution as well as the two sub-populations of clumps members and out-of-clump *field* stars. We identified some 20944 stars in clumps (or $\approx 52\%$) at the end of expansion. The expectation that all stars have zero- or low-velocities is validated by the peak in the distribution around $v_x = 0$.

As sub-structures form and interact mutually, generating tangential as well as radial motion, the peak broadens but remains symmetric about the origin. The large velocities are brought by stars in clumps, which demonstrates that interactions within the substructures boost the internal velocity dispersion of the cluster as a whole. Field stars dominate the low-amplitude regime. Their velocity distribution is well-fitted with a Gaussian (shown as a dotted blue line), down to one-tenth the height of the central peak, or about 1% of all field stars.

To illustrate further the idea that large velocities are confined to clumps formed by fragmentation modes, we compare on Fig. 3.10b a set of models with different initial values of H_o : 0, 0.3, and 1. Clearly when $H_o = 0$, the velocities are identically zero and there is no fragmentation whatsoever (apart from root-N noise). The distribution is then a sharp peak centered on zero. For positive but low values of H_o , the fragmentation modes do not develop much before the apex and the (non-radial) velocities remain small. The central peak has a much narrower dispersion, and the high-velocity wings are clipped. In this case, too, analysis of the weakly fragmented system shows that virtually all high-velocity stars are found in clumps. The velocity distribution for the case $H_o = 1$ is added for comparison. The fact that the full range in velocities is reduced by a factor ~ 3 for the less fragmented model is also an indication of the shallower potential well of the clumps

The full population velocity distribution (solid black line) at first sight is very similar to those of Klessen & Burkert (2000, Fig. 5). In that figure, the authors show the velocity distribution of gas particles in a fragmenting system. Klessen & Burkert attribute the high-velocity tails to gas particles falling towards stellar clumps at supersonic speed. Supersonic motions imply that gas particles trace ballistic trajectories, and hence behave like point mass particles.

A small fraction of field stars in our calculations also have large velocities. We suspected that these stars might have acquired their large velocity through in-fall toward a nearby stellar clump. We did not, however, find compelling evidence that would allow us to identify the origin of high velocities in field stars. Inspection of a sequence of snapshots failed to show that the velocity vectors were pointing at nearby stellar clumps: it is therefore not possible to make the same assertion as Klessen & Burkert and state that stellar clumps accrete some field stars.

It is possible, on the other hand, that high velocities originate from past star-star interactions. However, we did not find clear trends in the few orbits that we studied which would confirm such an event. The question of mass accretion by stellar clumps might be best settled if we added gas to our simulations to boost the mass resolution, and analysed model data using mock CCD frames, as did Klessen & Burkert. This was not attempted here.

We close this section with a remark about the velocity distributions seen on Fig. 3.10 and the internal state of the stellar clumps. Because small clumps would have time to evolve dynamically through star-star collisions and reach a state of near-equilibrium (see §2.2.4) we would expect clumps to develop a velocity field similar to Mitchie-King models of relaxed self-gravitating star

clusters (Binney & Tremaine, 2008). The one-dimensional velocity distribution of Mitchie-King models plotted in a logarithmic scale approaches a flat-top when $|v_{1d}|$ is small, and cuts-off rapidly at large values : the distributions are concave at all velocities. This holds true for all models independently of their King parameter¹ W_0 .

The shape of the distributions displayed on Fig. 3.10, on the other hand, is convex as we shift, from small, to large $|v_{1d}|$. We deduce from this straightforward observation that the clumps that formed through fragmentation and subsequent mergers cannot be treated as fully in isolation and in dynamical equilibrium à la Mitchie-King. Fragmentation in hydrodynamical calculations often proceeds from filaments and knots (e.g., Klessen & Burkert 2001; Mac Low & Klessen 2004; Maschberger et al. 2010; Bate, Tricco & Price 2014). The clumps that form in a fragmenting Hubble flow are also surrounded by filaments and other structures which perturb them.

3.3.2 The stellar mass function in clumps

We show on Fig. 3.11 the mass function of stars both in clumps, field and in the whole cluster. For brevity, we only show a model with a mass function truncated at $20M_\odot$, Rmh20, however our conclusions are not sensitive to the truncation value. The mass function of ≈ 6400 stars that were found in clumps (some 43%) is displayed as the red solid curve and all other stars, field stars, as the blue solid curve. The theoretical Salpeter distribution function for the same number of stars is shown in black dots, with grey shades giving the 1σ dispersion from multiple samplings. Finally, the green dashed curve shows the mass distribution of all 15 000 stars in the model. The lower panel is the same data normalised to the Salpeter data.

The uptake in massive stars for the whole population (green dashed line) of both clumps members and field stars is a statistical artefact and lie within the standard deviation of a Salpeter distribution with comparable sampling number.

The clump member population clearly deviates from a Salpeter distribution in two ways : first we note a deficit of low mass stars with respect to the theoretical Salpeter; secondly, although a Salpeter mass function is more or less consistent with the population up to $M \approx 2M_\odot$ (black dotted line) the distribution shows a clear excess of massive stars. We find that practically all the stars more massive than $10M_\odot$ ended up in a clump (this is the point where the solid red curve joins the dash green one).

A linear regression fit of the clump members mass function gives a power-law index of -2.15 ± 0.02 , shallower than the Salpeter index of -2.35. Applying the same analysis to field stars, we find a steeper mass function of index -2.46 ± 0.02 . The difference of ≈ 0.3 between the two populations is very similar to what is found in the Milky Way disc (see e.g. Czekaj et al. 2014; Rybizki & Just 2015; Bastian, Covey & Meyer 2010)

Bonnell, Vine & Bate (2004) and Maschberger et al. (2010) showed from inspection of hydrodynamical simulations that massive stars play a key role in the assembling process of clumps, attracting already formed protostars to them. We find a similar general trend in Hubble-fragmented gas-free simulations: clumps develop around massive stars so that their stellar mass function is top-heavy.

This excess can also be seen in the top panel of Fig. 3.12a in which for each of 440 clumps, we show as white dots the mass of their heaviest star as a function of the host clump's mass. These data were obtained from the R40h100 run. For comparison, we sampled a Salpeter mass function, drawing the same number of stars as found in each clump. We then identify the most massive star in the Salpeter sample ; the procedure was repeated 15000 times *for each clump* to obtain suitable statistics. The grey shades (color levels in the electronic version) shows the resulting distribution.

In a nutshell, Fig. 3.12a shows for each clump the likelihood that their most massive stars

¹Notice how this holds only because of the choice of a logarithmic vertical axis.

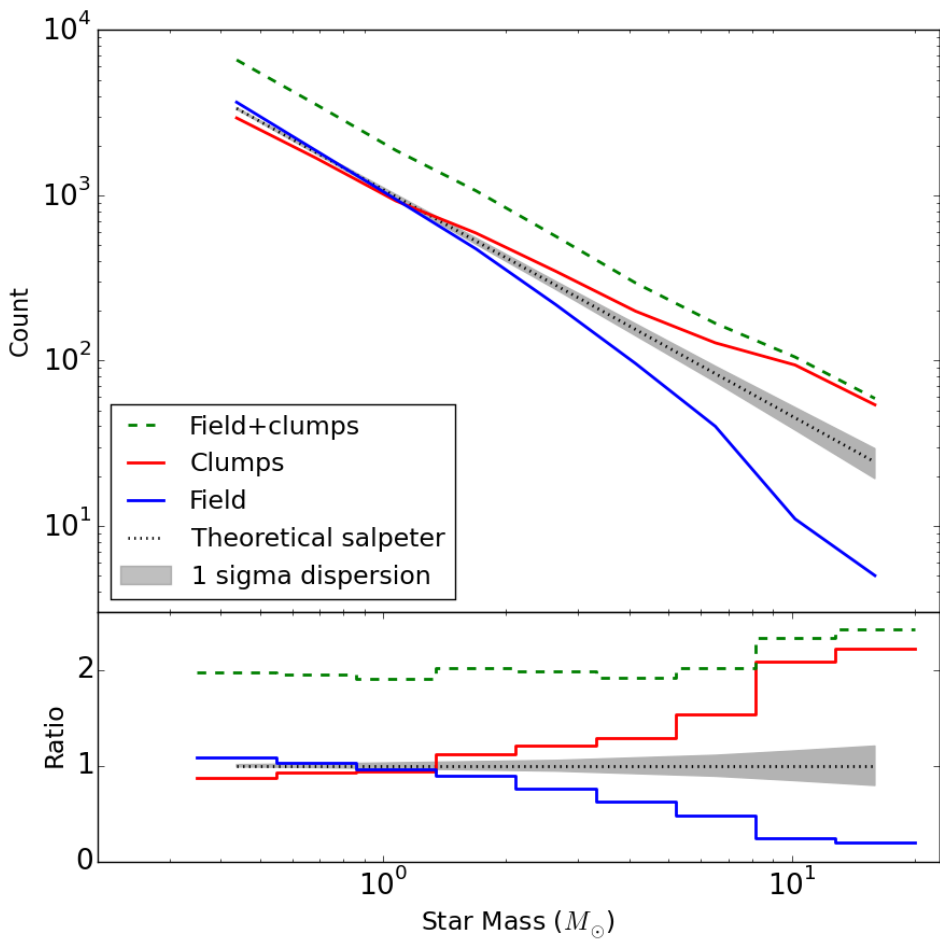
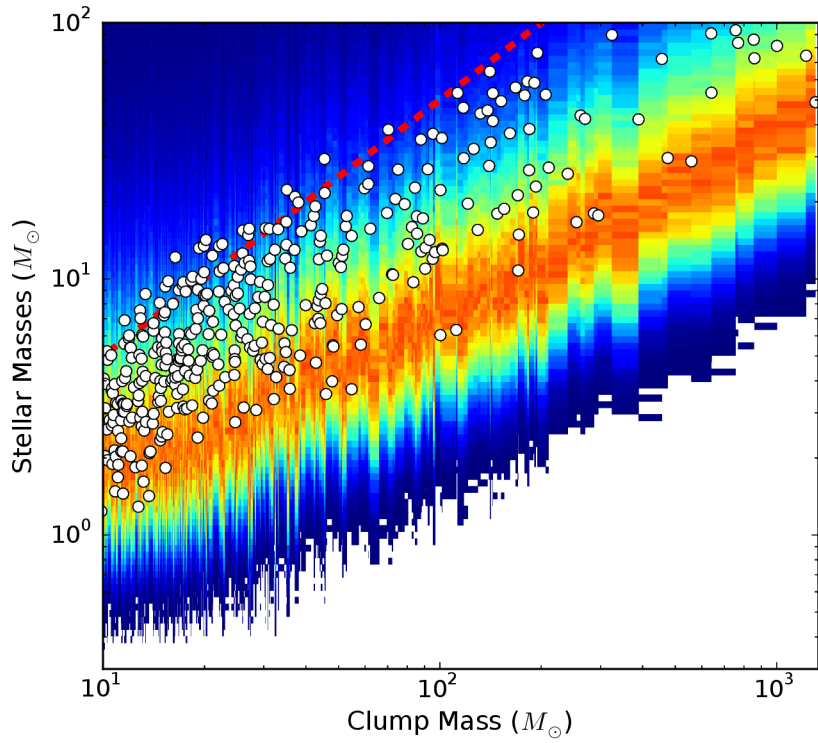
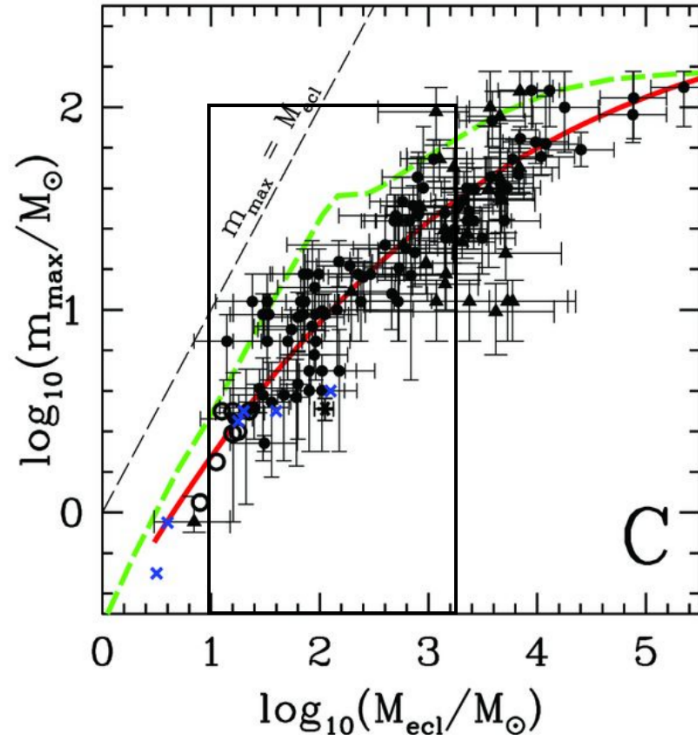


Figure 3.11: Top panel : Mass function of all stars belonging to a detected clump (solid red). The expectation drawn from a Salpeter distribution function for the same total number of stars in dotted black ; the grey shade are 1σ uncertainties. The green dashed line is the distribution for the full cluster. Bottom panel : same data normalised to the Salpeter expectation.



(a) Distribution clumps/field



(b) Distribution for different H_0

Figure 3.12: (a) Mass of the heavier star in each clump, shown as white dots, as a function of clump mass. The color map shows the likelihood for the maximum mass if all clump members were sampled from a Salpeter IMF ; the orange crest gives the maximum likelihood. The red dashed line shows the relation $m_{\text{clump}} = 2m_{\text{max}}$ (see. section 3.2.2). The data was taken from the R40h100 run. (b) is a similar distribution from Weidner, Kroupa & Pflamm-Altenburg (2013), built with data about young embedded star clusters from Weidner, Kroupa & Bonnell (2010). The black frame notes the range of masses displayed in (a).

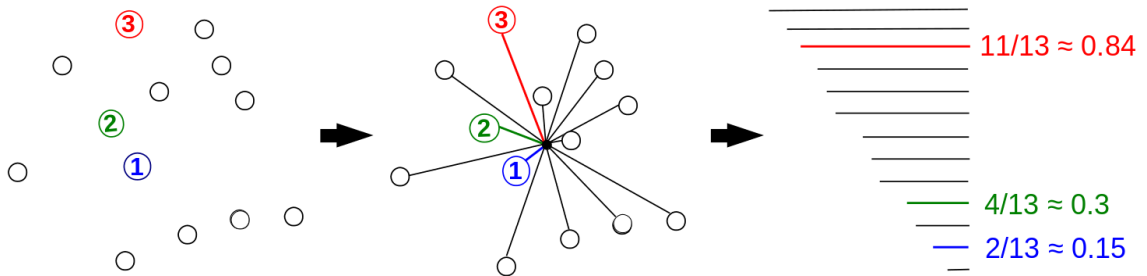


Figure 3.13: Illustration of the radial ranking method. Stars marked 1,2 and 3 are the first, second and third most massive stars in the clump. Distances to the geometrical center are computed then sorted. The position in the sorted list is converted to a number, the radial rank.

may be drawn from a Salpeter function, one could call the red maximum likelihood zone the "Salpeter valley". Only clumps with a mass $> 10M_{\odot}$ are included to account for a possible bias when clump membership reaches below $N_d = 12$ stars. It can be seen on the figure that the scatter of white dots tends to lie systematically above the Salpeter valley. If we add the relation $m_{clump} = 2 \max\{m_{\star}\}$ (cf. section 3.2.2), we find some overlap with the data (see the red dashed line on Fig. 3.12a). This clearly illustrates the tendency for massive stars to act as seeds when the clump form, while the scatter is driven by the merger and accretion history of individual clumps.

The correlation displayed on Fig. 3.12a is in good agreement with observational data for young embedded clusters of the same mass range published by Weidner, Kroupa & Pflamm-Altenburg 2013. We reproduced their figure on Fig. 3.12b with a black frame representing the range shown on Fig. 3.12a.

Note how the *scatter* in the correlation brought on by the dynamical processes at play during the adiabatic fragmentation phase also compares well with the data. Thus the stellar clumps modelled here recover an important characteristic of observed embedded young clusters.

3.3.3 Mass segregation

In this section, we ask whether the clump assembling process at play in our simulations accounts for the mass segregation measured in star-forming cores in hydrodynamical simulations. The measure of mass segregation of Olczak, Spurzem & Henning (2011) based on the MST, while efficient, will give noisy results for very small-N clumps. Instead, we follow Maschberger et al. (2010) and rank clump members according to their distance to the geometric centre of a clump, which is calculated by number-averaging (so this centre is not the clump barycentre). We then sort the bodies by mass and tabulate the radial rank of the three most massive ones. This process is illustrated on Fig 3.13.

The great advantage of this approach is that it is independent of geometry and absolute size once the ranking is normalised to the clump membership N_c . One issue arises with the binning of the rank, since small values of N_c give large intervals by construction, and conversely for populous clumps : we found a good compromise by setting the width of each bin to 1/20 since the mean clump mass $\sim 20M_{\odot}$ implies $N_c \sim 20$ on average. The procedure is repeated over all clumps identified in the run (typically on the order of ~ 200). The diagnostic for an un-biased sampling is a profile with radius that remains the same regardless of the mass selected ; if, furthermore, the stars are (on the mean) un-segregated in radius, then the profiles will be flat.

Fig. 3.14 graphs the distribution of rank of the three most massive stars in all the clumps from R40h100 fragmented state. The salient features are that 1) none of the distributions are

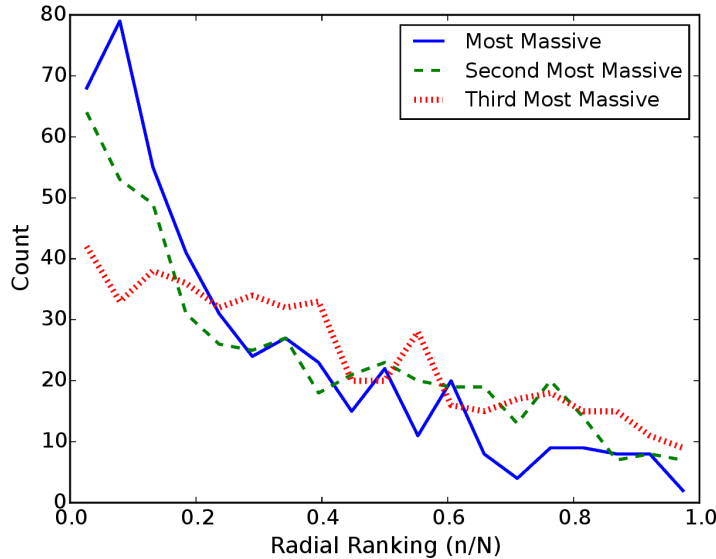


Figure 3.14: Histograms of radial ranking of first, second and third most massive star in each clump for a model with $N = 40\,000$ stars (R40h100).

flat, all three peaking significantly at small ranks ; and 2) there is a clear trend for the most massive star also to be the most segregated. Precisely this result had to be expected from the internal dynamics of small clumps (cf. section 2.2.4). Our Fig. 3.14 should be compared with Fig. 13 of [Maschberger et al. \(2010\)](#): the authors also found radial rank distribution to peak at small values for massive stars, showing a level of mass-segregation in their clumps.

It is striking that the measure of mass segregation attained here for a gas-free configuration is a good match to a full hydrodynamical setup. By implication the segregation proceeds more vigorously once the proto-stellar cores have condensed and behave essentially like point sources. The initial configuration that we have adopted relies only on density fluctuations to seed clumps, however once again we find evidence that massive stars begin and remain the centre of gravitational focus for clump formation. That is not so when clumps are setup using a fractal approach ([Goodwin & Whitworth, 2004](#); [Allison et al., 2009a](#)). There is then no segregation initially, and it all develops at or shortly prior to the global system evolution towards equilibrium (the collapsing violent relaxation phase).

3.4 Concluding remarks

We have developed a new approach based on adiabatic fragmentation to set up self-consistent configurations for stellar dynamics that link up the velocity field of stars to their irregular space configuration of arbitrary geometry, such as knots or filaments. The method offers great advantages: it is easy to implement; it can treat an arbitrary number of stars without any resolution issue. The light computational load allows for statistical ensemble averaging over large samples, as was done throughout this chapter. For instance, the computation time on a single card for 80,000 stars is about 12 hours. The methods has its limitations: the most significant one is the failure to include hydrodynamical effects. In the introduction, we mentioned other approaches partly based on hydrodynamics: such hybrid methods have been successful but remain limited in scope, for instance [Moeckel et al. \(2012\)](#), or demanding in computational resources (and so constrain the number of realizations), as in [Fujii & Portegies Zwart \(2016\)](#).

The importance of massive stars

During the fragmentation process in our models, heavy stars act as seeds for the growth of stellar clumps, and so the stellar clumps mass spectrum is shaped by the mass function of the available *stars*. Although the fragmentation through gravitation only does not include the detailed physics of star formation, we noted that hydrodynamical calculations including gas pressure and turbulence suggest that the gravitational potential of massive stars attract more gas and stars and, as such, act as seeds for the formation of clumps ([Bonnell, Vine & Bate, 2004](#)). We therefore recover a key prediction of hydrodynamical simulations. It is then interesting to ask whether observations show a correlation between the host clump mass and its population of massive stars.

Based on analysis of our fragmented Hubble models, we recover on Fig [3.12](#) a correlation between the maximum mass of a star found in a clump of a given mass, M_c . This $\max\{m_\star\} - M_c$ relation is eerily similar to the compilation for young clusters by [Weidner, Kroupa & Pflamm-Altenburg \(2013\)](#), from which we extracted the figure [3.12b](#). Furthermore, we also found that the stellar mass function in clumps has a much flatter (top-heavy) profile than in the field, *i.e.* stars that do not belong to any clump: power-law fits for the two stellar populations show that the Salpeter index for clumps stars is lower by about ≈ 0.3 compared to the same index for field stars. A similar difference is deduced for Milky Way data ([Czekaj et al. 2014; Rybizki & Just 2015](#); see also Fig 2 from [Bastian, Covey & Meyer 2010](#)): we argue that these characteristics will help tighten our understanding of the long-term evolution of such stellar associations, given that their properties are, on the out-set, close to actual data for young clusters. It should be emphasised that the global index of external galaxies may differ significantly from the canonical value $\alpha = 2.35$ (*e.g.*, the GAMA survey, [Gunawardhana et al. 2011](#); see also [Hoversten & Glazebrook 2008](#)). We have not explored here to what extent this difference in indices between field and clump populations will change for other values of the global index α .

We have also noted that the clumps are *mass segregated* at birth, *i.e.* at the end of the fragmentation process. When we apply the same ranking statistics as for hydrodynamical calculations of star formation, we obtain the same level of segregation for the three most massive stars in a clump (cf. Fig. [3.14](#)).

The slope of the clump mass function

[Klessen & Burkert \(2000, 2001\)](#) fit the gas clump mass function of their simulations with a power-law $\frac{dN}{dM} \propto M^{-\beta}$ where $\beta \simeq -3/2$. On the other hand, the *cluster* mass function in the Milky Way can be described as a power law with an index ranging from -2 to -2.4 ([Haas & Anders, 2010](#)). We have indicated that a power-law relation with a slope $\beta \simeq -4$ is a rough fit for the case where all the stars are identical (Fig. [3.9](#)). This is not so when a stellar mass spectrum is included : if a Salpeter distribution function is truncated at $20M_\odot$ a power-law with slope $\beta \simeq -1.7$ still fits approximately the distribution of clumps of mass $> 20M_\odot$; and when the Salpeter distribution function is truncated at $100M_\odot$, a power-law similarly fits the tail-end of the distribution but now with a slope of $\simeq -1$ (see Fig. [3.9b](#)). It is intriguing that the slope of the distribution should fall within the bracket of values for the observational data for clusters (-2.4^+) and hydrodynamical fragmentation models (-3/2). If the clumps formed from hydrodynamical fragmentation should become individual star clusters, and recover the $\beta \simeq -2$ or lower slope of observational data, then the distribution function must become steeper and also cover a broader range of masses. The same conclusion applies to the Hubble clump distribution function.

This implies either that clumps will merge so that a few very massive clusters will emerge, or that fewer massive clumps form in the first place. Comparison with existing cluster population needs us to assume these clumps do not fall back and merge through collapse. This is possible with an adequate galactic tidal field ripping apart this fragmented configuration and isolating the

clumps before the collapse. Many of the small stellar overdensities detected as clumps would not survive more than a few million years before dispersing through dynamical interaction, however the larger clumps could survive and appear as isolated cluster or part of an association. These massive clumps are the key to comparison to the galactic cluster mass function. We have shown how the stellar IMF provides seeds for the growth of massive clumps and have illustrated this with a Salpeter power-law IMF. A more realistic IMF has a steeper power index at larger stellar masses ([Kroupa, 2002](#); [Chabrier, 2005](#)). The fragmentation of stellar systems with fewer massive stars would deplete the clump mass function at larger masses more in line with observed statistics for clusters. This variability in the clump mass function highlights the major influence of the stellar IMF on the fragmentation process. A full exploration of fragmentation requires hydrodynamical simulations, which we have not performed here. These simulations remain limited to much smaller systems ([Bate, Tricco & Price, 2014](#); [Lomax et al., 2014](#)).

In the next chapter we assume an absence of tidal field and follow through with the final stage of evolution towards equilibrium. We compare the final configuration with those of [Allison et al. \(2009a\)](#) and the recent study by [Caputo, de Vries & Portegies Zwart \(2014\)](#).

CHAPTER 4

Collapse and dynamical evolution

In this chapter, we let the Hubble-Lemaître models evolve and undergo violent relaxation. We compare their dynamical evolution with that of cold uniform models. We investigate the evolution of the structure and global mass segregation.

Contents

4.1	The simulations	63
4.1.1	Description of the models	63
4.1.2	Scaling to physical units	64
4.1.3	Removal of the ejected stars	65
4.2	Collapse and virialisation	66
4.3	Global mass segregation	68
4.4	Concluding remarks	72

4.1 The simulations

4.1.1 Description of the models

The Hubble-Lemaître fragmented system is subvirial by construction. The configuration we took as a reference is the apex of the expansion: the kinetic energy initially injected in the expansion has been converted into potential energy through expansion or converted to transversal motion by two-body interaction. If the model is left to evolve further, it collapses, violently relaxing to reach a quasi-equilibrium state, resembling a Plummer or King model.

In the present chapter, simulations will use the fully fragmented state of Hubble models as initial conditions for the subsequent dynamical evolution. Observational clues point to collapsing and violently relaxing clusters. For example, [Cottaar et al. \(2015\)](#) find IC348, a young (2-6 Myr) cluster, to be both survirial and with a convergent velocity field, consistent with infalling motion. Our models undergo dry collapse with no gas, while real objects such as IC348 still contain residual gas. The scenario of our simulations is an idealized situation: clearly if there was residual gas between the clumps and it was evacuated through stellar feedback, both the clump merger rate and the depth of the potential achieved during relaxation would be affected. As a limiting case, rapid gas removal may lead to total dissolution (see for instance [Moeckel et al. 2012](#) and [Fujii & Portegies Zwart 2016](#)). In the current situation, all clumps will merge.

The numerical integration were done once more with the Nbody6 integrator with the same computational units. For comparison purposes, we also performed simulations of cold uniform sphere, a configuration which has been extensively used in the past (e.g.,[Theis & Spurzem 1999](#); [Boily, Athanassoula & Kroupa 2002](#); [Barnes, Lanzel & Williams 2009](#); [Caputo, de Vries & Portegies Zwart 2014](#); [Benhaiem & Sylos Labini 2015](#)) and one that minimises the level of

fragmentation and mass segregation in the on-set of collapse. The models are referenced as Rh100,Rh20,Ru100 and Ru20 in Table 3.1. We focus here on models with a mass function from $0.35M_{\odot}$ to $20M_{\odot}$ and 15000 stars, a compromise value for rich open clusters that should allow us to identify clearly collisional effects and trends with time, and ease comparison with the recent study by Caputo, de Vries & Portegies Zwart (2014) where most calculations are performed with that sampling. We let both Hubble-fragmented- and uniform sphere evolve up to 40 H.u.

4.1.2 Scaling to physical units

Before discussing the results, it is useful to translate the units of computation to physical scales. This is important if we want to discuss the state of the systems using one and the same physical time, such that the hypothesis of no stellar evolution holds good. To do so, we compute the free-fall time of an uniform sphere (a good approximation for fragmented model as well) both in physical units and Hénon units, which provide a conversion factor. We first have to choose an initial physical length scale for the system by setting $R_h = 1$ pc. With a total system mass of $M = 15 \times 10^3 M_{\odot}$, this gives a half-mass volume density

$$\rho_h = \frac{M/2}{\frac{4}{3}\pi r_h^3} \simeq 1.8 \times 10^3 M_{\odot}/pc^3, \quad (4.1)$$

well within values typically inferred from observations.

The free-fall time of an uniform sphere, obtained from conservation of energy and integration, is expressed:

$$t_{ff} = \sqrt{\frac{3\pi}{32G\rho_h}} \quad (4.2)$$

Computing $\rho_{h,\text{Hénon}} \simeq 0.13$, we can now compute both values of the free-fall time:

$$t_{ff} \simeq 1.5 t_{\text{Hénon}} \quad (4.3)$$

$$\simeq 0.2 \text{ Myr} \quad (4.4)$$

Which gives:

$$1 t_{\text{Hénon}} \equiv 0.13 \text{ Myr} = 1.3 \times 10^5 \text{ yr} \quad (4.5)$$

Thus by running up to 40 H.u we ensure that the systems evolve for ~ 6 Myr years, about the lifetime of a $50M_{\odot}$ star.¹

We now want to evaluate the crossing and relaxation timescales in such a system, as they were defined in the introduction (1.2.2), and how they relate to the total duration of the simulation. We could attempt to derive a crossing time for the initial, subvirial state but it would not be representative of the evolution of the system. Instead, the more useful crossing time has to be computed from the equilibrium state achieved. Using the virial theorem and conservation of energy, we can derive dynamical timescales for the equilibrium system. From the definition, the crossing times is defined:

$$t_{cr,eq} = \frac{2R_{h,eq}}{\sigma_{1d,eq}} \quad (4.6)$$

From here on, we write the subscript 0 for initial values and no subscript for equilibrium values. To obtain both R_h and σ_{1d} we start from the total energy of the system. At $t=0$, velocities are null, all energy is potential energy. It can be computed by integrating from the center to R_0 . We obtain

$$E_0 = -\frac{3}{5} \frac{GM^2}{R_0}. \quad (4.7)$$

¹For our models with more massive stars, up to $100M_{\odot}$, these represent only $\sim 5\%$ of the total mass and their removal would not significantly alter the dynamics of the system.

From virial theorem and conservation of energy, we get the following equations at equilibrium

$$\begin{cases} 2E_k + E_p = 0 \\ E_k + E_p = E_0 \end{cases} \implies \begin{cases} E_k = -E_0 = \frac{3}{5} \frac{GM^2}{R_0} \\ E_p = 2E_0 = -\frac{6}{5} \frac{GM^2}{R_0} \end{cases} \quad (4.8)$$

which can be combined with

$$E_k = \frac{1}{2} M \sigma_{3d}^2 = \frac{1}{2} M (3\sigma_{1d})^2 = \frac{9}{2} M \sigma_{1d}^2 \quad (4.9)$$

to get

$$\sigma_{1d} = \sqrt{\frac{2GM}{15R_0}}. \quad (4.10)$$

As for the half-mass radius at equilibrium, its value is dependant on how concentrated the system is and is not easy to derive. Instead, we replace in Eq. (4.6) the half-mass radius by the virial radius R_v , defined as:

$$E_p = -\frac{GM^2}{2R_v} \quad (4.11)$$

which value should not depart significantly from the half-mass radius and provides an useful approximation. Combining Eq. (4.8) and Eq. (4.11) it comes

$$R_v = \frac{5}{12} R_0. \quad (4.12)$$

Knowing that $R_0 = 2^{1/3} R_{h,0}$, we can now write a good approximation of the crossing time in the relaxed, equilibrium system

$$t_{cr} \simeq 2.28 \frac{R_0^{3/2}}{\sqrt{GM}} \quad (4.13)$$

$$\simeq 3.21 t_{\text{H\'enon}} \quad (4.14)$$

$$\simeq 0.5 \text{ Myr} \quad (4.15)$$

With $N = 15000$ we find from (1.6) a two-body relaxation timescale

$$t_{rel} \simeq 380 t_{\text{H\'enon}} \quad (4.16)$$

$$\simeq 60 \text{ Myr} \quad (4.17)$$

and from (1.10), considering a mass range of $m_{max}/\langle m \rangle = 20$, we find a mass-segregation timescale

$$t_{ms} \simeq 20 t_{\text{H\'enon}} \quad (4.18)$$

$$\simeq 2.8 \text{ Myr} \quad (4.19)$$

Our simulations last for far less than a relaxation time, but we can expect to see some mass segregation set in in our models.

4.1.3 Removal of the ejected stars

The previous section considered there was no mass loss during the collapse and relaxation that leads to the equilibrium system. However, a look at the simulations shows this assumption does not hold. Some stars are ejected from the system after the collapse, when the system bounces.

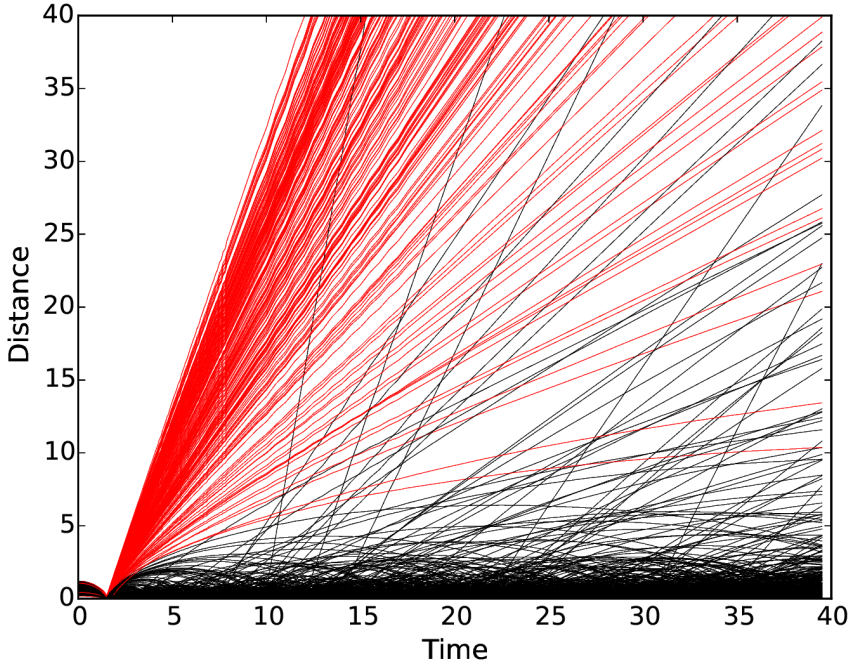


Figure 4.1: Distance to origin for 750 stars from run Ru20 (see Table 3.1). Red lines show the trajectory of stars that are considered ejected according to our criterion.

These stars are not part of the equilibrium system as they have no influence on the central dynamics.

To better understand the evolution of the central, bound system only, we need to isolate and subtract the ejected stars. The obvious way to do this would be to compute the stars mechanical energy and to remove all stars with positive energy. Though this works for a majority of the ejected stars, a subset of them has a marginally negative energy. These register as bound when they are essentially out of the system (far beyond the original system radius).

To collect a maximum number of ejected stars efficiently, we spotted the time when the potential energy is maximum, when the collapse occurs. We then identified all stars whose distance to the center increased monotonically from there onwards. The full selection criteria is therefore :

$$v_r(t) > 0, \forall t > t_{ff} \quad \text{or} \quad E_\star > 0, \forall t > t_{ff} \quad (4.20)$$

This allows a more complete selection of the ejecta. On Fig. 4.1 we graph $|\mathbf{r}|$ as a function of time for a subset of escapers (shown as red curves) for the uniform collapse model Ru20. The black curves are trajectories for bound stars given for comparison. Some of these bound stars are later ejected from the system due to two-body interactions, as seen on the figure.

4.2 Collapse and virialisation

The constant diffusion of kinetic energy by two-body interaction means that no stellar system ever reaches a steady equilibrium. However we can contrast the time-evolution of two configurations and draw conclusions about their observable properties.

With this in mind we turn to Fig. 4.2 in which we show the evolution of the half-mass radius for the cold uniform model (labeled Ru20 ; thick red curve), and the Hubble model (labeled Rh20 ; thin blue curve). Both systems have the same bounding radius initially, contract to a small radius when $t \simeq 1.4$ units and then rebound at time $t \simeq 2$ units. When all the stars are

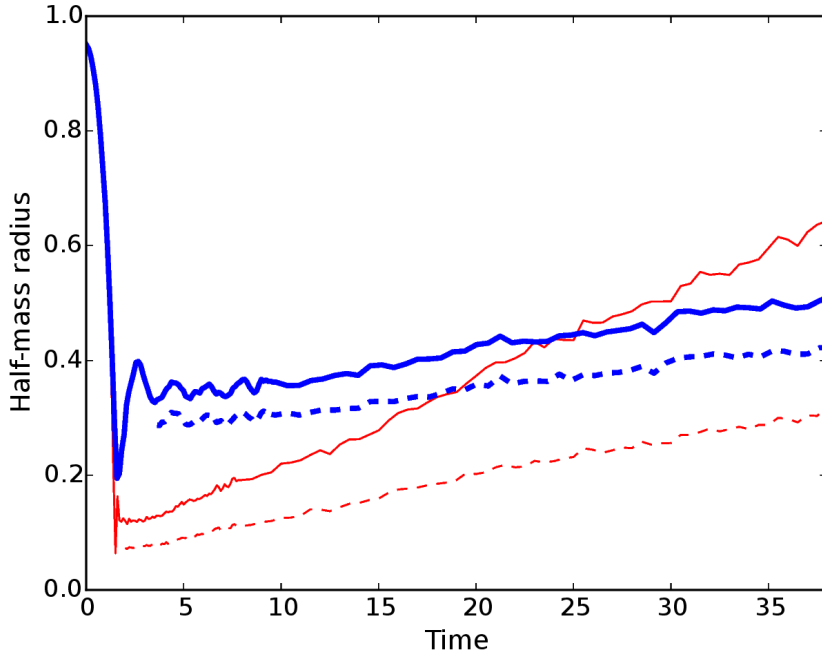


Figure 4.2: Half-mass radius as function of time for two systems undergoing collapse : a uniform-density sphere (thin red solid curve) and a clumpy Hubble model (thick blue solid curve). Half-mass radii are in H.u, as well as the time axis, where $t_{\text{Henon}} = 1 \text{ unit} = 0.13 \text{ Myr}$. Dashed lines are the half-mass radii of the same systems but including only the bound stars.

included in the calculation for r_h , we find that the radius increases at near-constant speed after the collapse. That trend does not appear to be slowing down which indicates that a fraction of the stars are escaping. The first batch of escapers is driven by the violent relaxation, however the trend continues beyond $t = 20$ units, corresponding to $t > t_{ms}$ which implies two-body scattering and effective energy exchange between the stars. Note how the uniform model has a much deeper collapse and rebounds much more violently, shedding a fraction twice as large of its stars:

Run	Ejected stars	Ejected mass
Ru20	4227	27%
Rh20	1932	12%

The half-mass radius R_h increases steadily in both models, from the bounce at $t \approx 2$, until the end of the simulation (values in H.u):

$$\begin{aligned} R_h \text{ Uniform} &\quad 0.11 \rightarrow 0.63 \quad (\times 5); \\ R_h \text{ Hubble} &\quad 0.34 \rightarrow 0.49 \quad (\times 1.4). \end{aligned}$$

Clearly the gentler collapse of the fragmented model has led to a more extended post-collapse configuration and reduced two-body evolution. Observe how the uniform model Ru20 is ejecting more stars than the Hubble model : if we repeat the calculation for the Hubble run Rh20 but now include only the bound stars, the curve of R_h obtained and shown as dash is shifted down but keeps essentially the same slope ≈ 0.004 . By contrast, the calculation for the bound stars of run Ru20 yields a much shallower slope than for the whole system: the slope drops from 0.015 to about 0.007. Irrespective of how the half-mass radius is calculated, the conclusion remains the same and agrees overall with the remark by [Caputo, de Vries & Portegies Zwart \(2014\)](#) that boosting the kinetic energy of the collapsing initial configuration softens the collapse ; this

was shown in a different context by [Theis & Spurzem \(1999\)](#) and confirms these older findings. Here, the fragmented model has finite kinetic energy due to the clumps' internal motion. The important new feature brought by the fragmented initial conditions is that the *mass profile* of the virialised configuration evolves much less over time in comparison.

At the bounce, the half-mass radius of the Hubble model is ≈ 4 times larger than that of the initially uniform sphere at rest (Fig. 4.2). The half-mass radii overlap at time $t \approx 15 H.u.$ (solid curves) or $t \approx 50 H.u.$ (dashed curves). Is the same trend applicable to all Lagrangian radii? To answer this question we plot on Fig. 4.3 the ten-percentile mass radii for the two models. The results are displayed for the two situations including all the stars (top row) or bound stars only (middle row).

It is striking that the curves show very little evolution at all mass fractions for the case of the Hubble model (see right-hand panels on the figure), whereas all mass shells either contract or expand in time for the uniform one. We have noted how this model should undergo two-body relaxation on a timescale of $t \approx 380 H.u$ while the innermost 10% mass shell shows an indication of *core-collapse* at $t \simeq 5 H.u..$ This is due to the presence of a mass spectrum, the time-scale for core-collapse should be closer to the mass-segregation timescale, $t \simeq 20 H.u..$ The remaining difference can be attributed to the smaller total mass (due to the ejecta) and the various assumptions made in section 4.1.2.

We note here that the two sets of curves reach very similar values at the end of the calculations ($t = 40 H.u.$). A key difference between the two models, therefore, is that the final configuration of the Hubble model is almost identical to what it was at the bounce ; the same simply does not hold in the case of a uniform-density collapse. Furthermore, the Hubble calculation shows no hint of two-body relaxation or core-collapse.

[Caputo, de Vries & Portegies Zwart \(2014\)](#) and [Theis & Spurzem \(1999\)](#) noted how a finite amount of kinetic energy in the *initial* configuration alters the depth of the bounce during collapse. The ratio of half-mass radius at the bounce, to its initial value, is then

$$\frac{R_h}{R_{h,0}} \simeq Q_0 + N^{-1/3} \quad (4.21)$$

where Q_0 is the virial ratio of the initial configuration (see [Caputo, de Vries & Portegies Zwart, 2014](#), Fig.5). We computed the kinetic energy of the Hubble configuration and found that the internal motion of the clumps means that $Q_0(\text{Hubble}) \simeq 0.02$ for a Salpeter mass function with upper truncation value of $20M_\odot$. With $N = 15k$ stars, the ratio $R_h/R_{h,0} \simeq 0.041$ when $Q_0 = 0$ shifts to $R_h/R_{h,0} \simeq 0.061$ when $Q_o = 0.02$, or a factor close to $3/2$. To account for the difference in kinetic energy of the initial configurations, we may therefore rescale the uniform model such that positions are $\times 3/2$ and the time unit is $\times (3/2)^{3/2} \simeq 1.84$.

The new configuration would evolve in time in exactly the same way after mapping positions and time to their rescaled values. The result is shown as the bottom row on Fig. 4.3. Note that we have blown up the vertical axis to ease comparison between uniform and Hubble models with bound stars only included. The rescaled uniform model is now slightly more extended than before, but overall the final two configurations (at $t = 40 H.u.$) are as close as before rescaling. This demonstrates that the outcome of the uniform collapse and its comparison with the Hubble model is not sensitive to a small amount of initial kinetic energy. We note that while the ratio Q_0 is a free parameter in many setups for collapse calculations, that parameter is fixed internally in the Hubble approach.

4.3 Global mass segregation

To investigate the state of mass segregation in our models, we follow the analysis of [Caputo, de Vries & Portegies Zwart \(2014\)](#). The masses are sorted by decreasing values, then subdivided into ten equal-mass bins. This means that the first bin contains the most massive stars. The

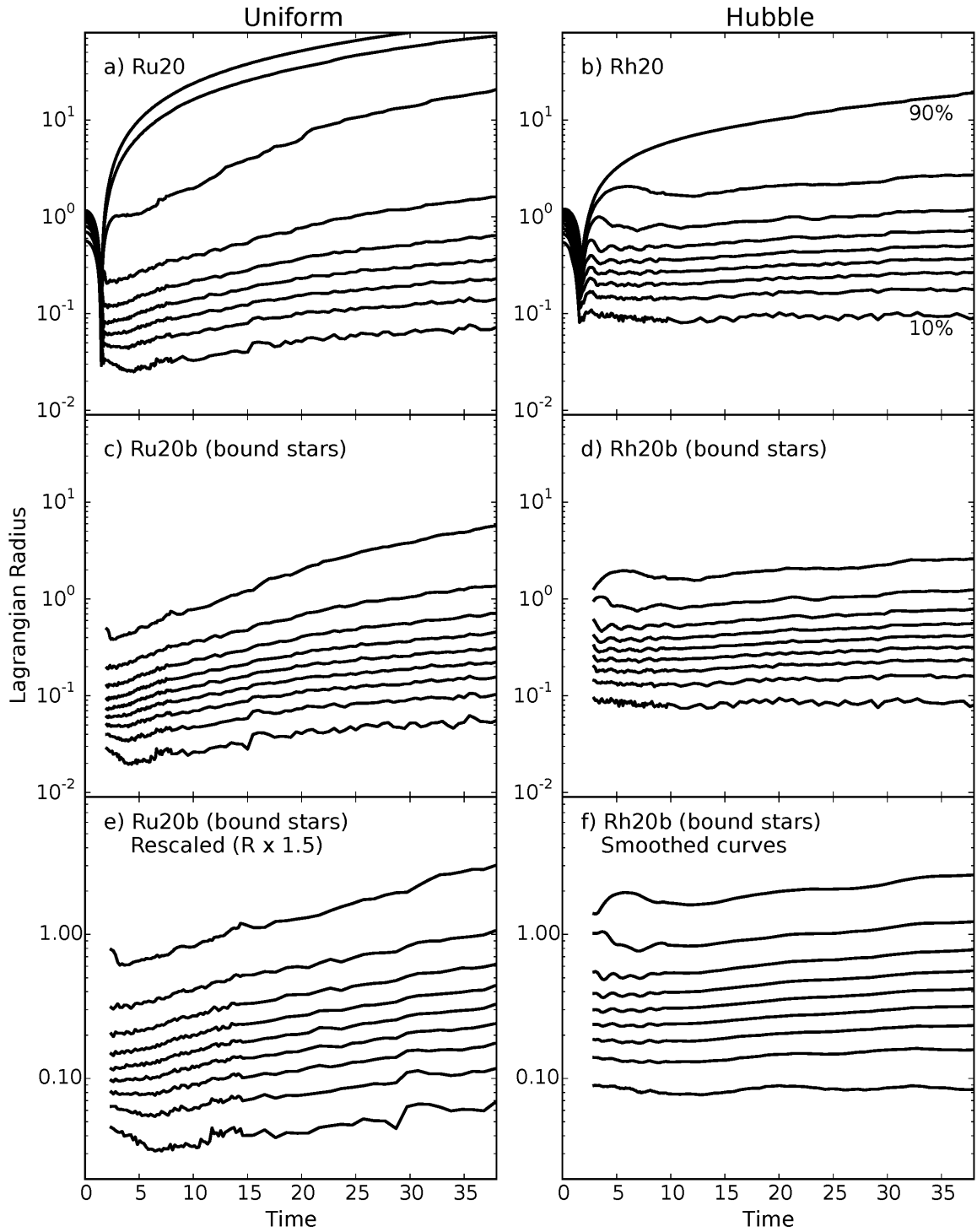


Figure 4.3: The ten-percentile mass radii (10% to 90%) as function of time. Radii and time axis are in H.u, with $t_{\text{H}\acute{\text{e}}\text{n}\text{o}n} = 1\text{unit} = 0.13\text{Myr}$. Left panels show the Uniform model and right panels show the Hubble fragmented models. Panels a and b show the evolution of the whole systems, while panels c and d shows the same radii computed for the bound stars only. Panel e shows the Uniform bound model (Ru20b) for which radius and time were rescaled to compensate the difference of initial kinetic energy (see text for details). Panel f shows the same information as panel d with smoothed data. 10% and 90% radii are labelled in the top right panel.

number of stars in each bin increases as we shift to the following bins, since their mean mass decreases, and so on until we have binned all the stars. The half-mass radius R_h computed for each bin is then plotted as function of time. In this way the mass segregation unfolds over time: if the stars were not segregated by mass, all radii R_h would overlap. If two sub-populations share the same spatial distribution, their respective R_h will overlap.

Figure 4.4 graphs the results for initially uniform-density- and fragmented Hubble models. The layout of the figure is the same as for Fig. 4.3. The violent relaxation phase leads to mass loss for both models and the much more rapid expansion of the half-mass radii of low-mass stars is an indication that most escapers have a lower value of mass.

Fig. 4.4(c) and (d) graphs R_h for the bound stars of each sub-population. Clearly the initially uniform-density model is more compact early on, but note how the heavy stars sink rapidly to the centre, more so than for the case of the Hubble model. The spread of half-mass radii increases with time for both models, however two-body relaxation in the uniform-collapse calculation is much stronger, so that by the end of the simulations the half-mass radii of the low-mass stars of the respective models are essentially identical.

Since the low-mass stars carry the bulk of the mass, that means that the two models achieve the same or similar mean surface density by the end of the run. At that time, the heavy stars in the uniform-collapse calculation are clearly more concentrated than in the Hubble run (compare the radii out to $\sim 40\%$ most massive stars). A direct consequence of this is that the *color* gradients of the core region of a cluster are much reduced when the assembly history proceeds hierarchically, in comparison with the monolithic collapse. It will be interesting and possibly important in future to compare such models with actual data for young clusters.

Another interesting remark is that the kinematics of the stars within the *system* half-mass radius is much different between the two models. For the Hubble calculation, the system half-mass radius, ≈ 0.43 H.u, at $t = 40$ (cf. Fig. 4.4d) coincides with the half-mass radius of the $30 - 40\%$ bin stellar sub-population. All bins up to that range show little or no time-evolution, around the end of the run, which we interpret as efficient retention of these stars by the relaxed cluster. In the case of the uniform-collapse run, the system half-mass radius reaches ≈ 0.33 H.u., which is significantly larger than the radius for the $30 - 40\%$ stellar sub-population. For that model, only the bins $0 - 10\%$ and $10 - 20\%$ are flat, and all the others increase almost linearly with time. Thus a fair fraction of bright stars deep in the cluster show systematic *outward streaming* motion, along with low-mass ones. This brings up the possibility to measure this signature motion through relatively bright stars, originating well inside the cluster half-mass radius. Recall that only post-bounce bound stars were selected to compute R_h on Fig. 4.4(c) and (d); the expansion is therefore not driven by chance events (e.g., Fig. 4.4a), but rather through two-body relaxation. On the down side the bright tracers would be short-lived, and this may prove a strong constraint for observational detection.

Given the early dynamical evolution associated with substructured stellar clusters, some observed dense objects may yet be out of equilibrium. We wish to investigate the out-of-equilibrium state of our models just after the collapse. To ease the comparison between the two systems, the same rescaling procedure as for Fig 4.3 was applied to the uniform model, only this time the scaling was chosen so that the two clusters have comparable densities after the bounce. Lengths were multiplied by 4; the time-axis is then scaled up by a factor $(4)^{3/2} = 8$. The result can be seen in panel (e); panel (f) shows a smoothed and zoomed in Hubble model for comparison.

We compare the values of the different half-mass radii of the various population before the dynamical mass segregation sets in. This process is clearly visible as the drop of the half-mass radius of the most massive stars during the evolution. We are interested in the segregation which originates from the collapse and is present before this dynamical evolution. Table 4.1 sums up the values of the half-mass radii taken at $t \sim 5$ for both models, both corresponding to the same unevolved post-collapse state (see arrows on panels e and f on Fig 4.4). With on the

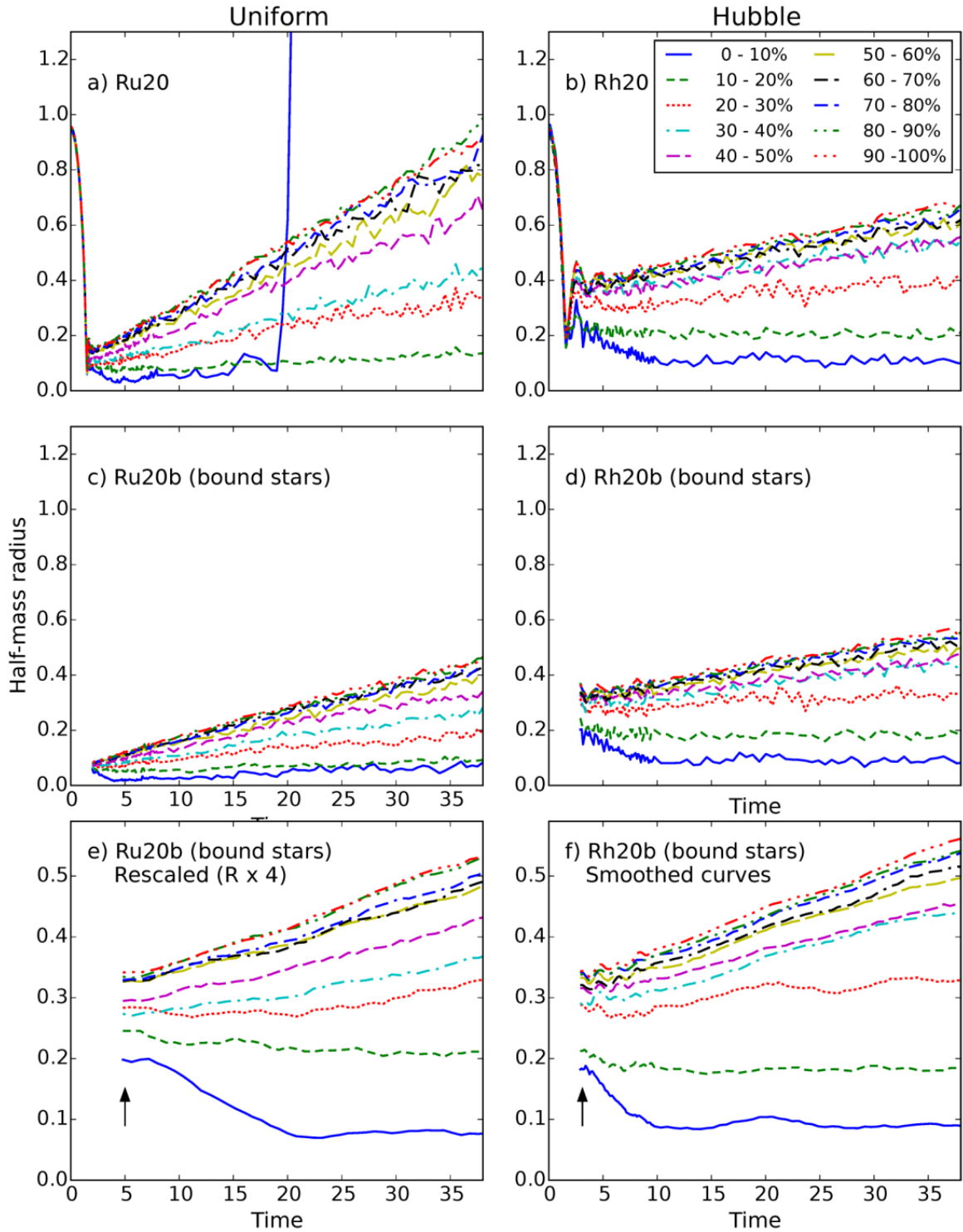


Figure 4.4: Half-mass radii of stars selected by mass as function of time. Each bin identified with 0-10%, 10-20% .. 90-100%, contains ten percent of the total system mass. The stars where sorted by mass in decreasing order, and used to fill each ten-percentile mass bin in order. Hence the first ten-percentile contains the most massive stars, the next ten-percentile the second group of massive stars, and so on until the 90-percentile bin which contains the least massive stars in the model and is the most populated. Half-mass radius and time are in H.u, with $t_{\text{Henon}} = 1 \text{ unit} = 0.13 \text{ Myr}$. Left panels show the evolution of the Uniform model (Ru20, Ru20b) and right panels do the same for the Hubble model (Rh20, Rh20b). The organization of panels follows the same layout than figure 4.3 with a different factor for the rescaling of the uniform system.

Table 4.1: Values of half-mass radii and their ratio to that of the most massive stars. The mass categories are labelled X%-X+10%, with the percent symbol omitted for brevity. The results are for the rescaled bound uniform model (rescaled Ru20b) and the bound Hubble model (Rh20b), after the collapse, and before dynamical mass segregation sets in.

Uniform (%)	0-10	10-20	20-30	30-40	40-50	50-60	60-70	70-80	80-90	90-100
Radius	0.20	0.245	0.282	0.273	0.294	0.325	0.326	0.328	0.335	0.340
Ratio	1	1.23	1.41	1.37	1.47	1.63	1.63	1.64	1.68	1.70
Hubble (%)	0-10	10-20	20-30	30-40	40-50	50-60	60-70	70-80	80-90	90-100
Radius	0.18	0.21	0.286	0.293	0.316	0.321	0.333	0.338	0.342	0.344
Ratio	1	1.16	1.58	1.63	1.76	1.78	1.85	1.88	1.90	1.91

order of ~ 100 stars per bin or more, one estimates roughly a ten-percent standard deviation from random sampling. To measure the *relative* segregation between populations, the table also lists the ratios of each half-mass radius to the one for the most massive stars.

Both models appear mass segregated (since these ratios are significantly greater than unity). The Hubble model is more segregated, on the whole, albeit in a different way compared to the uniform model. The segregation in that one is more regular and spreads over more mass bins. In the Hubble model, the segregation is much enhanced for the first two mass bins. Such differences in the degree and nature of segregation can be explained by the clumps structure before the collapse. We showed in section 3.3.3 the clumps were mass segregated with the most massive members being preferentially located at their center. The low membership and mass of most clumps implies that segregation mostly affects the very top of the stellar mass function. This segregation, predominant among massive stars, is then found in the resulting centrally concentrated system, after the collapse, and visible on Fig. 4.4.

The inheritance of mass segregation was studied by [McMillan, Vesperini & Portegies Zwart \(2007\)](#) for the case of merging Plummer spheres. [Allison et al. \(2010\)](#) furthermore showed that mass segregation in the system as a whole is enhanced for more filamentary fractal initial condition (lower dimension, D ; see their Fig. 5). Here our results confirm this observation. Mass segregation is a sensitive function of the initial clumpiness of the system and has immediate bearing on the dynamics of the virialised configuration, since all massive stars are more concentrated in the core.

4.4 Concluding remarks

We followed Hubble-Lemaître fragmented models throughout collapse and subsequent dynamical evolution, and compared their structure and mass segregation to cold uniform models.

Fragmented models undergo a softer, shallower collapse than uniform models, due to their irregular spatial distribution and internal kinetic energy. Uniform models eject more than twice as much stars from the system at the bounce due to this deeper collapse and virialize with a 4 times smaller half-mass radius. This high concentration enhances two-body evolution and the system expands faster than the Hubble models, even when excluding the ejected stars from the system. Interestingly, after 40 H.u, or 6 Myr, both systems achieve approximately the same density and distribution.

Both uniform and fragmented models develop mass-segregation over time, with the low-mass stars being preferentially ejected or diluted. However, just after collapse, Hubble-Lemaître models exhibit a mass segregation mainly affecting the most massive stars. This characteristic is preserved throughout evolution while the segregation seen in uniform models is more spread out in the mass function. This is a signature of the hierarchical formation, as this "Top-focused"

segregation developed in small clumps and was inherited by the whole system. This would enhance colour gradient in the core of real clusters, opening the way for an observational criteria to assess the formation scenario of relaxed clusters.

Part II

Binary stars in substructured clusters

CHAPTER 5

Introduction to binaries

In the second part of this thesis we turn to binary stars and their relation to star clusters.

Binary stars are crucial to understand the evolution of star clusters for a variety of reasons. They can be a reservoir of energy, supporting the core of a cluster against collapse by giving away their internal energy to perturbers, effectively ejecting stars and heating the system, affecting its global evolution and stopping core collapse (e.g [Heggie & Aarseth 1992](#)).

The statistical properties of binary star populations in dense stellar associations in particular may shed light on the discovery of multiple star-formation episodes in rich stellar clusters ([Anderson et al., 2009](#)). For instance, binary stars enhance strong dynamical interactions which in turn may speed-up evolution off the main sequence and so boost enrichment of the ISM through winds (e.g., [Tailo et al. 2015](#)). Tight binaries of short-lived massive stars may evolve to produce exotic stellar remnants including black hole progenitors ([Bacon, Sigurdsson & Davies, 1996](#); [Davies et al., 2009](#)). Blue stragglers, abnormally hot stars for the age of their host clusters, are thought to form in binary mergers, making them a dynamical record of the past binary population and dynamical state of the cluster ([Knigge, Leigh & Sills, 2009](#)).

Finally, accurate knowledge of binary populations in stellar clusters enable good estimation of their dynamical mass, as the integrated velocity dispersion is largely biased by the binaries internal motions, see [Rubenstein & Bailyn \(1997\)](#).

In this short introduction to binaries, we define a binary system, detail

5.1 What is a binary star ?

When two massive bodies of mass m_1 and m_2 interact gravitationally, they can have different types of trajectory depending on their total energy:

$$E = E_k + E_p = \frac{1}{2}m_1v_1^2 + \frac{1}{2}m_2v_2^2 - \frac{Gm_1m_2}{\|\mathbf{r}_1 - \mathbf{r}_2\|}. \quad (5.1)$$

If $E < 0$, they are bound and locked in a binary system. Such systems are characterised by their semi-major axis a , their eccentricity e , their period p , their total mass $m_t = m_1 + m_2$, mass ratio $q = m_2/m_1$ with m_1 being the primary, more massive than m_2 . Mass, period and semi-major axis are related by Kepler's third law:

$$\frac{Gm_t}{4\pi^2} = \frac{a^3}{p^2}. \quad (5.2)$$

Interestingly, expressed in AU, M_\odot and years, $G \simeq 4\pi^2$, thus the law can be written:

$$\left(\frac{m_t}{1M_\odot}\right) \simeq \left(\frac{p}{1\text{yr}}\right) \left(\frac{a}{1\text{AU}}\right)^3. \quad (5.3)$$

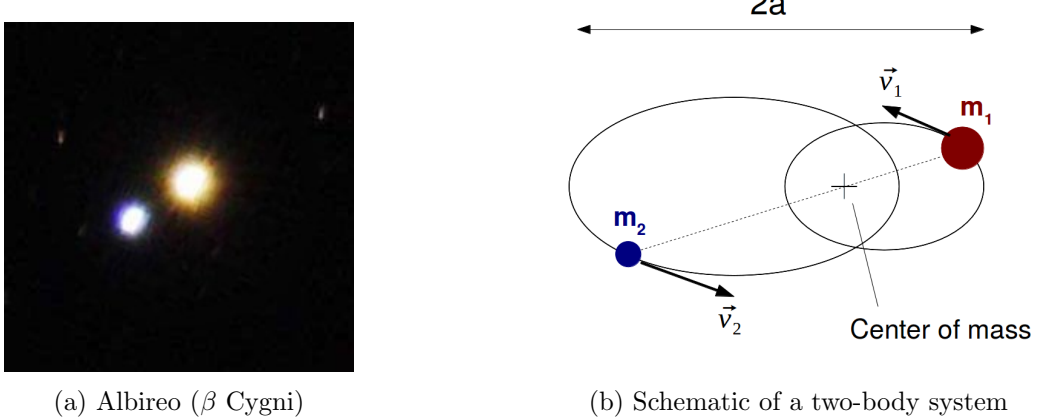


Figure 5.1: (a) Hubble observation of the binary star Albireo, fifth brightest star in the Cygnus constellation. Albireo A, the red star, is a close binary system itself (not represented on (b) for simplicity). The pair has a period of 213 years and a semi-major axis $a \simeq 66$ AU.

The total energy of the binary can be expressed as a function of a and m_t :

$$E = -\frac{Gm_1m_2}{2a} \quad (5.4)$$

5.2 Multiplicity fraction

In a stellar population, some fraction of stars will be found in multiple systems: some in binaries and some in higher order hierarchies. A hierarchical triple is a stable 3-body bound system, a binary of which one of the component is a binary itself. The same principle applies to quadruple, quintuple, etc. One of the brightest stars in the night sky, Castor, is a sextuple hierarchical system, with 6 stars in a stable system.

Counting binaries and multiples is not straightforward: do you count triples as two binaries or three stars in a multiple system ? In their SPH simulation paper, [Goodwin, Whitworth & Ward-Thompson \(2004\)](#) discuss several ways to measure the degree of multiplicity among stars in a system, each of them quantifying different properties, such as companion probability, companion frequency or pairing factor.

Let S be the number of single stars, and B, T , and Q the number of binary-, triple-, and quadruple systems, respectively. The fraction of multiple stars bound in binaries, triples, .. to the total number of multiple plus single stars, is

$$f_m = \frac{B + T + Q}{S + B + T + Q}. \quad (5.5)$$

This last measure is used in seminal observational papers ([Duquennoy & Mayor, 1991](#); [Raghavan et al., 2010](#)) and is our adopted choice. As pointed out by [Hubber & Whitworth \(2005\)](#), f_m in Eq. (5.5) has several advantages: 1) it may be restricted to a given mass m , setting S_m the number of single stars, and B_m, T_m, Q_m the multiple stars with a primary of that mass ; 2) the multiplicity fraction is observationally robust: when a binary is being reclassified as a triple, or an even higher order multiple system, the fraction does not change. These definitions may be extended to cover a mass range in a coherent way, by substituting $m \rightarrow \langle m \rangle$, the mean value over the range. This is useful mostly when comparing systems with different stellar mass functions.

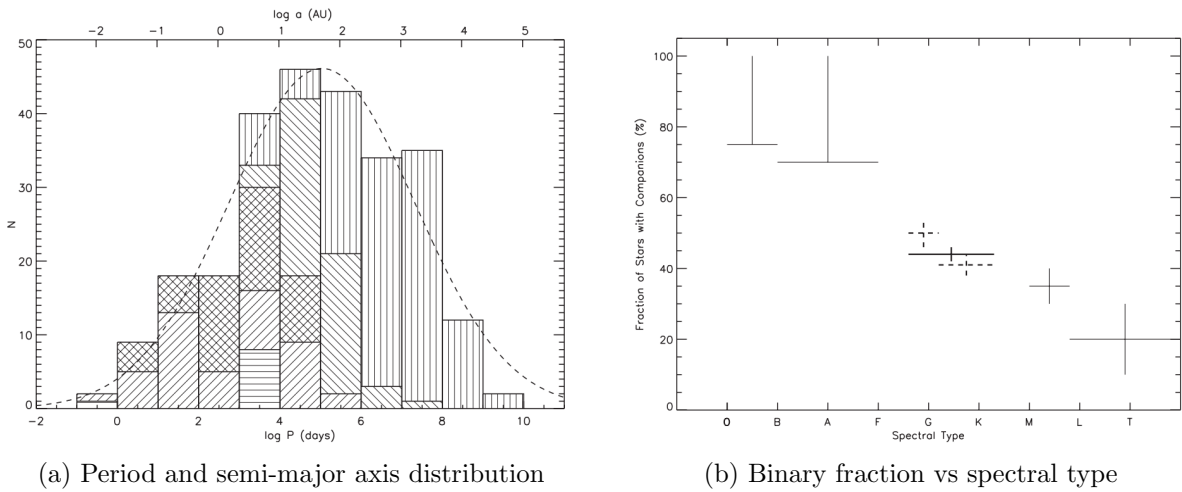


Figure 5.2: (a) shows the observed distribution of period and semi-major axis observed in the field. Different hatchings show different observation techniques: horizontal lines show unobserved companions detected by the proper-motion acceleration of components, positively sloped lines show spectroscopic binaries, negatively sloped lines visual binaries, cross hatching show objects found with both, and vertical lines are objects with common proper motions. (b) was compiled from several surveys, detailed in Fig 4.? (to come later). Both figures were extracted from [Raghavan et al. \(2010\)](#).

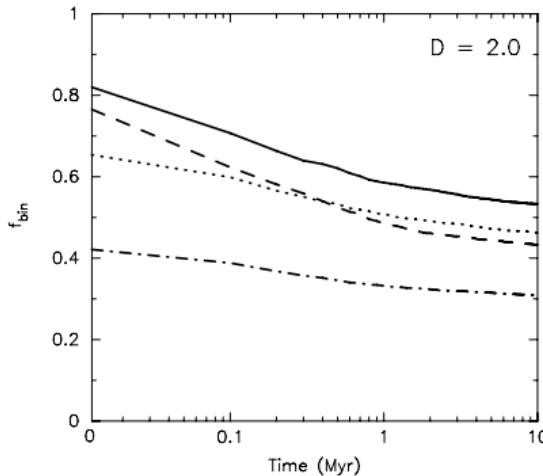
5.3 Observed population

A seminal survey of binary solar-type stars in the field was performed by [Duquennoy & Mayor \(1991\)](#). This seminal paper was updated and completed by [Raghavan et al. \(2010\)](#), who essentially confirmed the main results from the first study. They observed hundreds of F and G main-sequence stars in pairs and derived their binary parameters. The total binary fraction for these stars was found to be $\sim 53\%$ as binaries are quite common in most stellar populations. The authors also derived a period distribution, extending from less than a day to more than a Myr. The distribution was consistently well fitted by a log-normal distribution. The period distribution for F and G stars (as well as K and M stars, see [Fischer & Marcy 1992](#)) is:

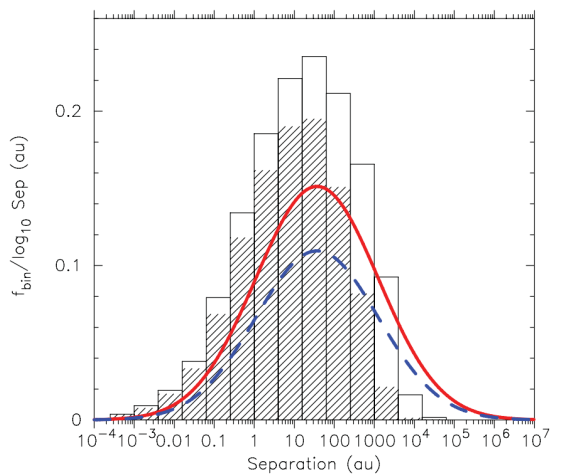
$$f(\log P) \propto \exp \left[\frac{-(\log P - \mu_{\log P})}{2\sigma_{\log P}^2} \right] \quad (5.6)$$

with the peak value $\mu_{\log P} = 5.03$, about 300 years, and the dispersion $\sigma_{\log P} = 2.28$, the distribution is shown on Fig 5.2a.

[Raghavan et al. \(2010\)](#) also compiled several observational studies of binaries with primaries of various spectral types. High mass stars, types O,B,A, (from $30+$ down to $2M_\odot$) have a high multiplicity fraction, about 75% while lower mass stars such as M-dwarfs only have 10-30% multiplicity, see Fig 5.2b. This trend of increasing multiplicity with increasing primary mass is found in many surveys. Binary surveys are easier in the field due to the very large sample and low stellar density. To perform similar studies in young star clusters is much harder due to source crowding and embedded stars. [Kouwenhoven et al. \(2007\)](#) attempted to characterize the birth binary population in the OB association Scorpius OB2. They found a very high multiplicity fraction, consistent with 100%, and a period distribution more consistent with a powerlaw than a log-normal distribution. From this survey and others, it is likely that the binary population in clusters undergoes an erosion through dynamical processing, with the field distribution as an end-result.



(a) Evolution of total binary fraction



(b) Evolution of semi-major axis distribution

Figure 5.3: (a): total binary fraction over time in a subvirial fractal system. Corresponding models for the solid, dashed, dot-dashed and dotted are respectively 100% initial binary fraction with log-normal distribution, 100% fraction with Kroupa distribution, field-like fraction with log-normal distribution and field and 75% fraction with log-normal distribution. (b): 100% initial binary fraction with an initial log-normal distribution (open histogram) and the evolved distribution after 1Myr (hashed histogram). Solid red and dashed blue lines are fits for, respectively, the G-dwarf and M-dwarf populations. Both figures were extracted from [Parker, Goodwin & Allison \(2011\)](#).

5.4 Simulate binary populations in clusters

As noted earlier, young clusters are born substructured, then undergo dynamical evolution. The rapid, global merging of sub-structures would bring together stars at a different stage of their formation (as in NGC1333, see [Foster et al. 2015](#)) while at the same time induce a shift from a clumpy Taurus-like profile to a more regular one. A simple but important question is how the internal dynamics of such complex configurations may affect the characteristics of a population of binary stars.

Many authors have explored this question through optimised initial conditions ([Kroupa & Burkert, 2001](#); [Marks & Kroupa, 2012](#)) or fractal configurations evolved with N-body integrators ([Parker, Goodwin & Allison, 2011](#); [Geller et al., 2013](#); [Parker & Meyer, 2014](#)). A common feature to all these studies is that the binary fraction drops over time regardless of their components (masses), due e.g. to close star-star encounters or heating from the external galactic tidal field, see Fig 5.3a. It was also shown that wide binaries are, as expected, more prone to destruction than more compact systems, as is illustrated by the evolution of the population seen in Fig 5.3b.

[Parker & Meyer \(2014\)](#) pointed out that the distribution of semi-major axes a of the field population is a strong function of the primary's mass: at fixed a , low-mass binaries carry less binding energy so the distribution cuts off at shorter separation (~ 20 AU) compared to that for binaries with a more massive primary (~ 300 AU). Their study of fractal initial conditions show that gravitational dynamics enhances the dissolution of low-mass systems. This then provides a clue to account for the larger relative fraction of heavy stars in binaries, such as seen in a compilation by [Raghavan et al. \(2010\)](#).

We note that hydrodynamical calculations of star formation have found young heavy stars to be preferentially found in dense clumps ([Maschberger et al., 2010](#)). Furthermore, it is not clear yet whether binary populations should be tailored according to the total system mass because of the limited range of $M \sim 10^2$ to $\sim 10^3 M_\odot$ of these studies ([Kroupa & Burkert, 2001](#); [Parker,](#)

[Goodwin & Allison, 2011](#); [Parker & Meyer, 2014](#)). Recall that the intensity of the tidal field is a prime agent of binary heating. A trend with mass may be expected on the ground that the drive to equilibrium of more massive systems leads to deeper potential wells (e.g. [Aarseth, Lin & Papaloizou 1988](#); [Boily, Athanassoula & Kroupa 2002](#)). A steep potential will give rise to strong tidal fields which may disrupt bound sub-systems ([Boily et al., 2004](#); [Renaud, Gieles & Boily, 2011](#)). A definitive assesment of this effect is difficult to reach because the results are a strong function of the system initial mass distribution and kinetic energy content ([Boily, Athanassoula & Kroupa, 2002](#); [Caputo, de Vries & Portegies Zwart, 2014](#)).

In the following chapters, we present an algorithm to detect binary stars in N-body simulations. This algorithm is applied to Hubble-Lemaître fragmented configurations, revealing a spontaneous binary population created by the expansion of the initial uniform sphere. We inject new binaries in the system to follow observed trends in the binary distribution. These systems are then left to collapse, as before, and the binary populations are monitored. We evaluate the influences of cluster membership and stellar density on the processing of binaries in substructured and subvirial systems. We also detail the formation of "extreme" binaries in our simulations, very short and very wide systems, and their dynamical origins.

CHAPTER 6

Detecting and injecting binaries

In this chapter, we introduce a new algorithm to detect and record binary system in N-body simulations. With this tool, we analyse the spontaneous binary population arising in the Hubble-Lemaître systems and we describe a binary injection method to complete this population to match the observations.

Contents

6.1 A new binary detection algorithm	83
6.1.1 Density comparison	83
6.1.2 Choosing a density ratio	84
6.2 The spontaneous binary population	86
6.2.1 Binary fraction vs primary mass	88
6.2.2 Spontaneous semi-major axis distribution	89
6.2.3 Completing the population	90

6.1 A new binary detection algorithm

6.1.1 Density comparison

The study of binary populations in nbody simulations requires an algorithm to detect binary systems and compute their characteristics. The simplest approach is to compute all star-star energies and consider bound pairs as binaries. This records a lot of ephemeral interactions, as n-body dynamics cause transient bound systems. An additional criteria is needed to assess the stability and robustness of a pair as a binary.

We introduce a new algorithm based on the idea of a density threshold: binaries must be denser than their direct environment. Before describing the algorithm, we wish to emphasize the importance of neighbour searches in this kind of study. Be it to obtain bound pairs or to study said pair direct environment, the quick retrieval of neighbours is crucial to an effective algorithm.

The method described here relies on the KD-tree algorithm (Press et al., 2007). While brute-force neighbour searches scale as $\propto N$, as all stars in the system have to be checked as potential neighbours, a KD tree, once built, performs neighbour searches with algorithmic complexity $\propto \log(N)$. The tree is built by sorting particles along one dimension, splitting them at the median, then sorting each branch along another dimension, splitting them again, and so on, cycling over dimensions. A two-dimensionnal example is show on Fig 6.1.

First, binary candidates are identified as negative energy pairs. The semi-major axis of the system is derived from the star motions, then a "binary density" is computed, with a the binary's

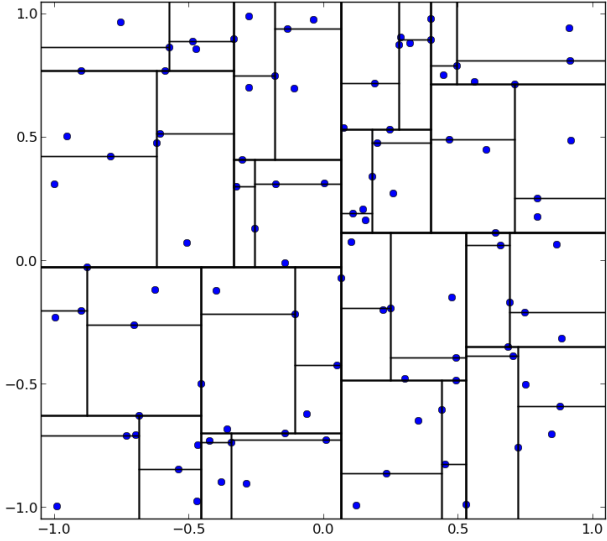


Figure 6.1: Illustration of a kdtree for a random two-dimensional distribution (blue dots).

semi-major axis :

$$\rho_{binary} = \frac{m_1 + m_2}{4\pi a^3/3}. \quad (6.1)$$

This is then compared to the local neighbour density, defined as the cumulated mass of a fixed number N_{nb} of neighbours to the pair over the spherical volume reaching to the last neighbour.

$$\rho_{local} = \frac{\sum_{i=0}^{N_{nb}} m_i}{4\pi r_{N_{nb}}^3/3}. \quad (6.2)$$

If the density ratio exceeds a threshold D ,

$$\frac{\rho_{binary}}{\rho_{local}} > D, \quad (6.3)$$

the pair is registered as a binary. Other authors, eg [Parker et al. \(2009\)](#); [Lomax et al. \(2015\)](#), have used close hybrids of the criteria that we have implemented.

Stars can be found to be part of several binaries at once, which happens more often for massive stars as they clear more easily the density threshold. When that happens, the algorithm selects from such connected systems only the pairs exhibiting the lowest (most negative) binding energy.

This method has two free parameters: N_{nb} and D . N_{nb} can be set from 6 to 10 neighbours without a substantial impact on the detection. The density ratio is a more critical parameter, as if it is chosen too low, a lot of ephemeral binaries are found, while a high value picks only the closest binaries, ignoring wider, yet stable, systems.

6.1.2 Choosing a density ratio

We wish to find a good compromise value for the critical density ratio D that maximizes the number of detected stable binaries without collecting too much transient system. To do so, we explore the results brought by different values of D in a nbody system containing binaries.

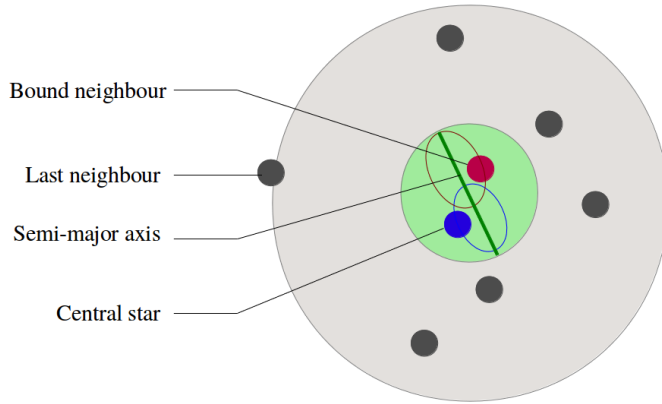


Figure 6.2: Illustration of the density threshold method. The central blue stars and the red bound neighbour describe a two-body orbit shown on the figure while the green bar indicates the major-axis of the system. This defines the binary density, green sphere, while the local density is defined with the grey stars, the other neighbours. Here, N_{nb} was set to 7.

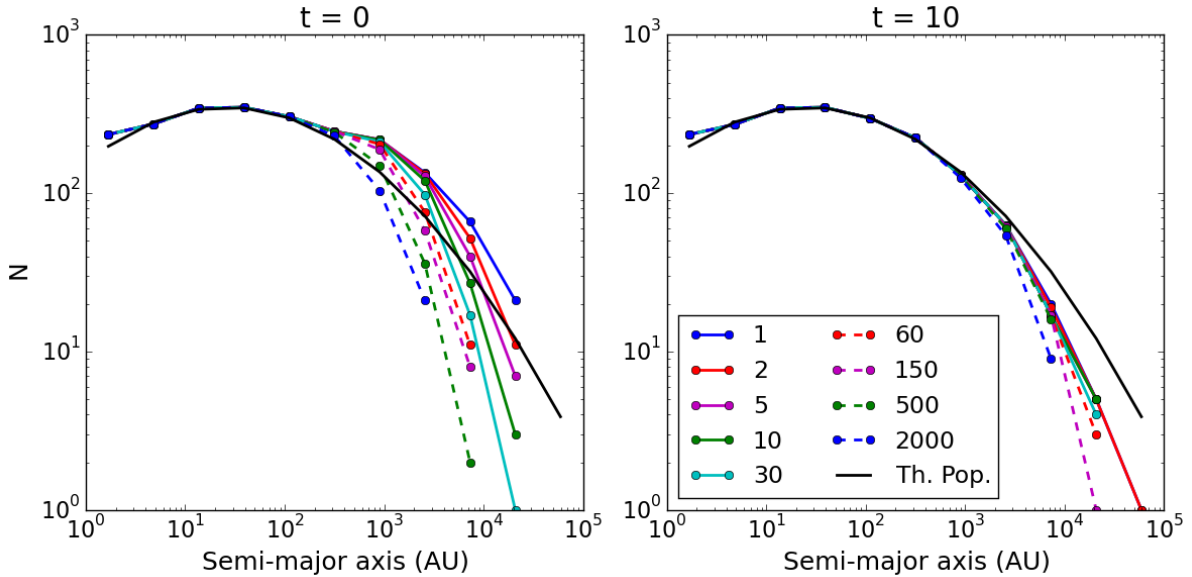


Figure 6.3: Semi-major axis histograms for various value of the density ratio D at $t=0$ and 10 H.u for a 10k star King model and a binary fraction $f_b = 0.3$. The injected log-normal population is shown as a black solid line.

We create a virialized King model with $N = 10000$ stars and a binary fraction of 0.3. This means there are 2300 binaries and 5400 single stars:

$$f_b = \frac{N_b}{N_s + N_b} = \frac{N_b}{N - N_b} \implies N_b = \frac{f_b}{1 + f_b} N = 2300. \quad (6.4)$$

The binaries follow the [Raghavan et al. \(2010\)](#) log-normal distribution introduced in [5.3](#). We let the system run for 10 H.u, or 12 crossing times, and write a snapshot every 0.1 H.u.

The binary detection is ran over all snapshots once per density ratio in the following list:

D	2000	500	150	60	30	10	5	2	1
---	------	-----	-----	----	----	----	---	---	---

We show on Fig [6.3](#) the semi-major axis distribution retrieved for various D for $t=0$ and $t=10$, with the theoretical injected population as a solid black line.

Looking at the left panel, for $t=0$, we see all density ratios return the same population for $a < 1000$ AU, while for higher separation, there are large variations. $D = 2000$ does not detect semi-major axis larger than 3000 AU, while $D = 1$ detects ~ 30 systems with $a > 10^4$ AU. After 12 crossing times, on right panels, we see the tight detected population didn't change, while all wide populations converged. The highest ratios did not undergo much change, while low ratios saw a large depletion of the population they initially returned.

We can say that a very high ratio only detect binaries that are guaranteed to resist the dynamical processing and survive, while low ratios detect more fragile systems. How ephemeral are these latter binaries ? To evaluate the different population detected by different ratios, we show on Fig [6.4](#) the detailed evolution of the wide, $a > 1000$ AU population. The large upper panel show all wide binaries evolution (time on y-axis) for $D = 2000$, arranged on the x-axis by time of first detection. Each pixel column represents a binary. The smaller sub panels show, for each density ratio, the history of the binaries this ratio detected that the previous, greater ratio did not. A binary that is detected with $D = 2000$ will also be detected for $D = 500$ and any other lower value. Fig [6.4](#) shows what kind of binaries lowering the ratio progressively brings to the detected population. The color codes the logarithm of the semi-major axis in AU, white means the binary is not detected.

The $D = 2000$ population is mainly made of stable, relatively tight binaries. About half the binaries are detected at $t=0$, while the others dynamically form in the system. Some are destroyed, other widened through interactions as their color bars transitions to a lighter color, sometimes after a "flickering" phase, when the detection goes on and off over successive snapshots. This is due to the binary entering a dynamical interaction with a third star or other binary, making the neighbour density undergoing spikes. This interaction leaves the binary with a weaker bound, thus higher binding energy.

Looking at the populations brought by lower ratios, we see they are progressively wider and more transient/flickering as the ratio lowers, which is to be expected. $D = 1$ only brings very ephemeral pairs, often not lasting more than a single snapshot. All ratios bring their share of transient binaries, but $D = 10$ is the last to capture relevant, relatively long-lived pairs.

Extreme values of density ratios bring a large difference in the detection of large binaries, but a moderate value like $D = 10$ appears the best compromise to capture the substance of a binary population.

6.2 The spontaneous binary population

Star-star interactions which take place during the HL expansion phase speed up the internal evolution of small substructures (or, clumps). The global expansion, on the other hand, brings about correlations in phase-space coordinates and the formation of loose binary stars (see Appendix A and [Kouwenhoven et al. 2010; Moeckel & Clarke 2011](#)). We refer to that population

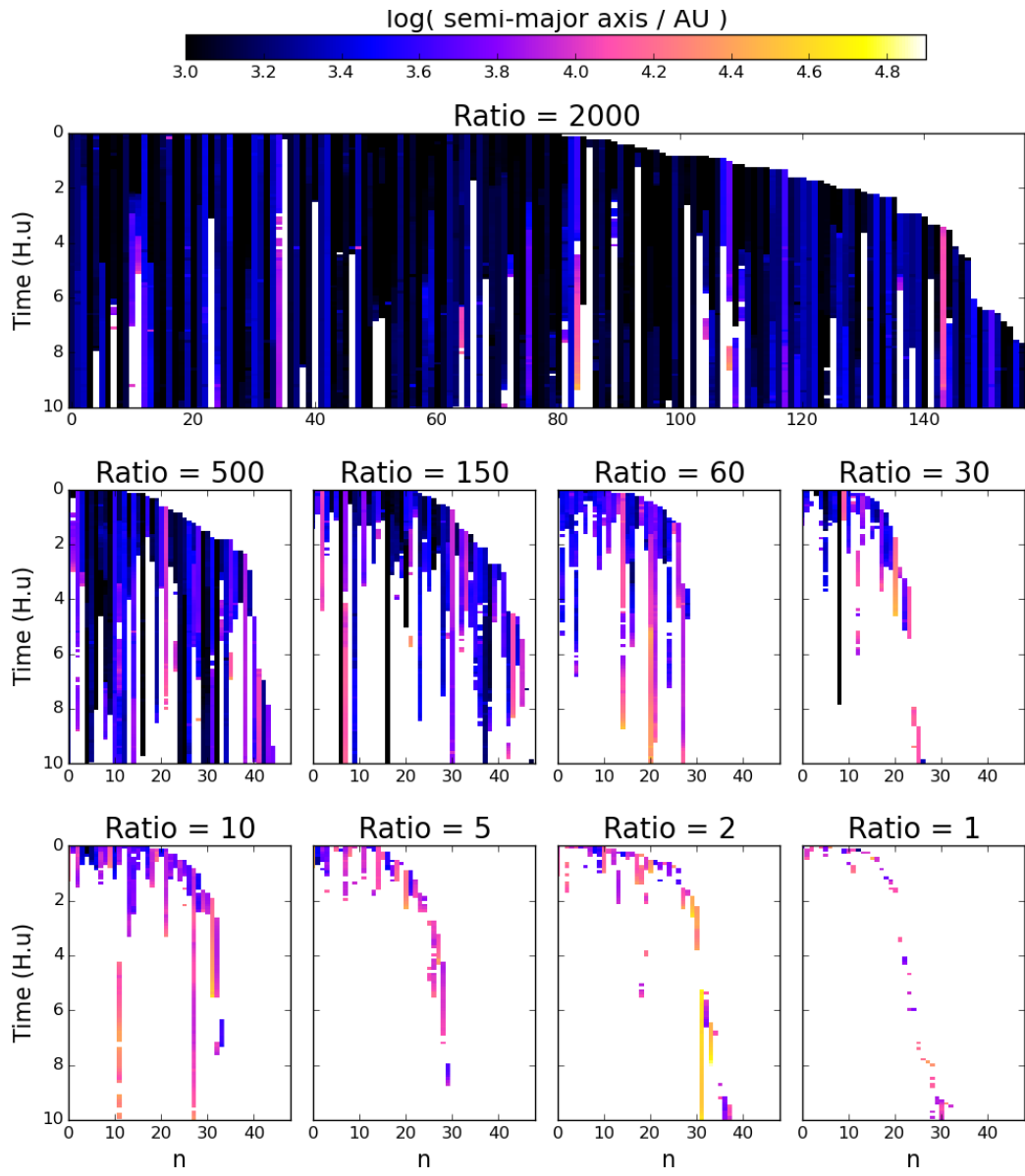


Figure 6.4: Visualization of the wide ($a > 1000$ AU) binary population in a King model over time. Large upper panel show the evolution of all binaries detected for a density ratio $D = 2000$, ordered by time of first detection. Each lower sub-panel show the new binaries detected with the new, lower, value of D compared to the previous one.

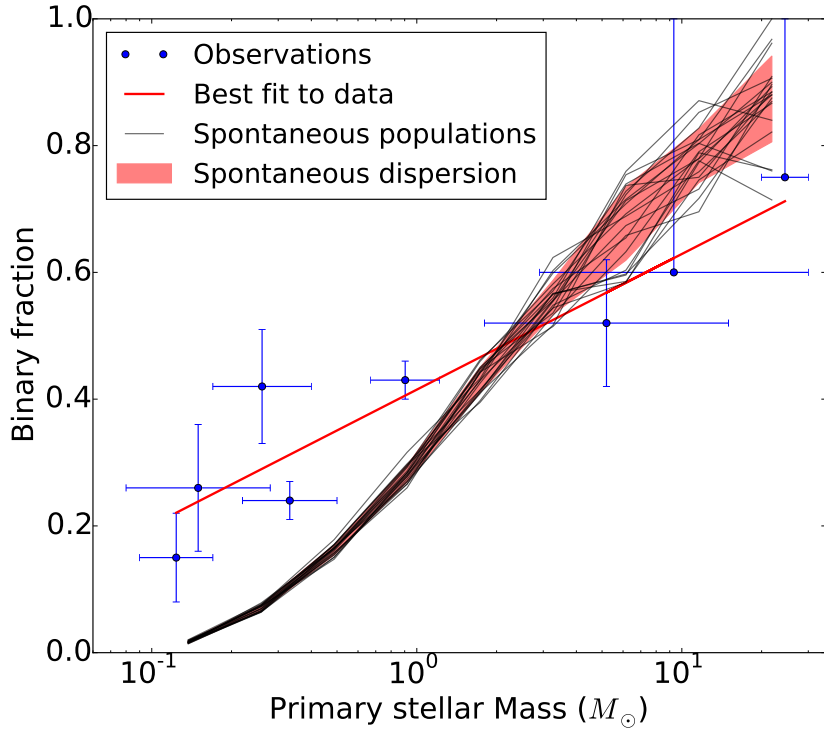


Figure 6.5: Observational data of binary fractions (dots with uncertainties) as a function of primary mass. The data are taken from (in increasing primary mass): [Close et al. \(2003\)](#); [Basri & Reiners \(2006\)](#); [Fischer & Marcy \(1992\)](#); [Ward-Duong et al. \(2015\)](#); [Raghavan et al. \(2010\)](#); [Patience et al. \(2002\)](#); [Preibisch et al. \(1999\)](#); [Mason et al. \(1998\)](#). The red line is a best-fit linear relation. The thin curves and 1- σ dispersion shaded area are the results for a population of spontaneous binaries obtained from HL models.

of binary stars as *spontaneous* binaries in the following. There is a trade off between the creation of spontaneous binaries, and their destruction / heating when they sit near or inside a clump. Their properties as a sub-population will be addressed statistically through numerical experiments.

6.2.1 Binary fraction vs primary mass

Several studies have found a strong correlation between the binary fraction f_m and the primary mass m of a binary system (for compilations, see e.g. Fig. 17 of [Bate 2012](#) and Fig. 12 of [Raghavan et al. 2010](#)). Since heavy stars tend to drive the formation of clumps in HL models, by attracting stars to themselves, it is natural to expect the HL procedure to give rise to a correlation of that nature.

The spontaneous binary fractions found in HL models for logarithmic primary mass bins are plotted as light grey lines on Fig 6.5. The shaded area shows the 1- σ dispersion for these distributions. The fraction increases rapidly with primary mass, and is in close agreement with the data for primaries of mass higher than $2 M_{\odot}$, when f_m exceeds 50%. However, the HL models show a significant deficit of low-mass primary binaries in comparison to observational data.

The high binary fraction for heavy primaries can be explained, at least in part, by considering the mass segregation occurring in the clumps during their formation. We shown in Chapter 3 that massive stars tend to sink to the center of clumps. These high mass stars are more likely to capture another star to form a binary through a three-body interaction as they sit in denser

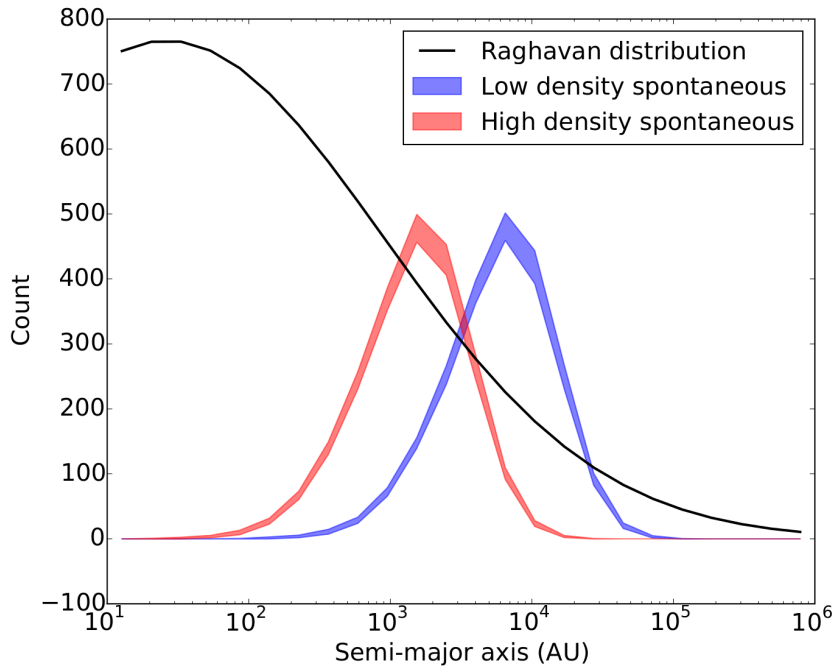


Figure 6.6: Distribution of semi-majors axis of spontaneous binary populations for two values of stellar number density. Green curve show the canonic separation distribution from [Raghavan et al. \(2010\)](#).

environments ([Spitzer, 1987](#)). A heavy star also creates a deeper potential well wherein to trap a fly-by star at the on-set of HL fragmentation. There is indirect evidence for the three-body binary formation process to draw from mass-segregated clumps, because these binaries have a mean mass ratio $q = m_2/m_1$ that is significantly *larger* than expected from random pairing. The mean value of q for binaries with a primary star in the range $15 - 30M_\odot$ is 0.21 ± 0.11 , whereas random pairing yields a mass ratio of 0.02 ± 0.02 for that mass range. Due to mass segregation inside clumps, massive stars are more likely to pair up with moderately heavy companions rather than light ones.

6.2.2 Spontaneous semi-major axis distribution

The distributions of semi-major axes a and orbital periods are the main parameters used to characterise binary populations. Up to this point, the distances were given in computational N-body units. To convert the models to physical scales, we matched their stellar number density within the half-mass radius to that of observed clusters. [King et al. \(2012\)](#) compiled data for several young clusters and gave their stellar densities within half-mass radii, with high values reaching $400 \text{ stars}/\text{pc}^3$, typical of the ONC, and low-densities of $\sim 6 \text{ stars}/\text{pc}^3$, more akin to the Taurus region. These are the two reference values used to build up our dataset of numerical models. The time conversion gives a total duration of the simulations of 2.3 Myr for the high density clusters and 18 Myr for the low density ones.

In practice the spontaneous binaries develop a bell-shaped distribution of separation centered on ~ 2000 AU for a high-density HL model, and ~ 7000 AU for a low-density one, shown on Fig. 6.6. This is much wider than the averaged value of ~ 50 AU for the Galactic field population ([Duquennoy & Mayor, 1991](#); [Raghavan et al., 2010](#)), where separations of ~ 1 AU or lower are not uncommon. Hydrodynamical calculations by [Bate \(2012\)](#) show that orbital energy dissipated in the early stages of formation may cause binaries with an ~ 10 AU separation to shrink to $a \sim 0.5$ AU in the course of $t \sim 1$ Myr. Analytical arguments by [Stahler \(2010\)](#)

and [Korntreff, Kaczmarek & Pfalzner \(2012\)](#) would have external drag forces from residual gas drive a tight binary to merge completely. [Kroupa & Burkert \(2001\)](#) have shown that stellar collisions alone can not bring a narrow distribution of semi-major axes to the full width of observed values. Other studies such as [Parker & Meyer's in 2014](#) investigated the evolution of a binary population identical to the field but embedded in clumpy, fractal clusters ([Goodwin & Whitworth, 2004](#)) to test the robustness of the field population. A full spectrum of separations is desirable for comparison with data and theoretical models but is not a natural outcome of the HL fragmentation.

We follow [Parker & Meyer \(2014\)](#) to ease comparison with their setup, by supplementing the population of spontaneous binaries with one that matches the field galactic populations at small a . In doing so, we should also constrain the primary mass distribution so as to redress the deficit of small-mass primaries (Fig. 6.5).

6.2.3 Completing the population

Completion procedure

The addition of new binaries to the HL distribution is not straightforward, as the phase space coordinates of stars in an HL fragmented system are the consequence of the numerical evolution during the expansion (no known functional distribution function). A practical and coherent method is to build the extra binary population *before* the HL expansion phase, and split them at apex.

The first step is to choose the proper distribution of primary mass for these new binaries. It should take into account the spontaneous population to preferentially populate the low-mass primary space. It should also take into account the fact that as the system expands with an effective number of stars $\tilde{N} = N - n_{in}$ with n_{in} the number of injected binaries, as these contain two stars fused in a single object until apex. Thus, the number of spontaneous binaries is reduced. Moreover, some spontaneous pairs form at the end of the HL phase with one fused binary as a component. Many of these spontaneous binaries (we found $\approx 50\%$) are no longer classified as bound pairs once the massive point mass is split into the binary. By making a few assumptions, it is possible to account for these influences and derive a distribution of primary masses consistent with a final binary fraction distribution close to observations. The procedure is detailed in appendix ???. Once primaries are picked, secondaries are chosen through random pairing in the remaining population and fused binaries are introduced in the uniform, pre-expansion model.

Once the expansion ends and before binary splitting, the semi-major axis distribution of spontaneous binaries is measured. Many of these (we found $\approx 50\%$) will no longer be classified as bound pairs once the massive point mass is split into the binary. A completion distribution is obtained by subtracting the semi-major axis distribution from spontaneous (only considering the ones expected to survive) from the [Raghavan et al. \(2010\)](#) distribution, so the final population recovers the observed population as much as possible. The injected binaries are split with semi-major axis drawn from this completion distribution.

Result

This procedure was tested on two sets of twenty Hubble-Lemaître models, one with low density (≈ 6 stars/ pc^3), the other with high density (≈ 400 stars/ pc^3), both with 20k stars. The resulting binary fraction is plotted on Fig 6.7 as a function of the primary mass¹. The deficit of low-mass primaries was bridged, while the fraction for high-mass primaries was slightly reduced (from 0.85 down to 0.75 for a primary mass of $\approx 20M_\odot$; note the increased scatter). This is the effect previously mentioned of splitting fused spontaneous binary components with a heavy

¹Only the low mass primary models are shown, as density does not affect the primary-mass distribution.

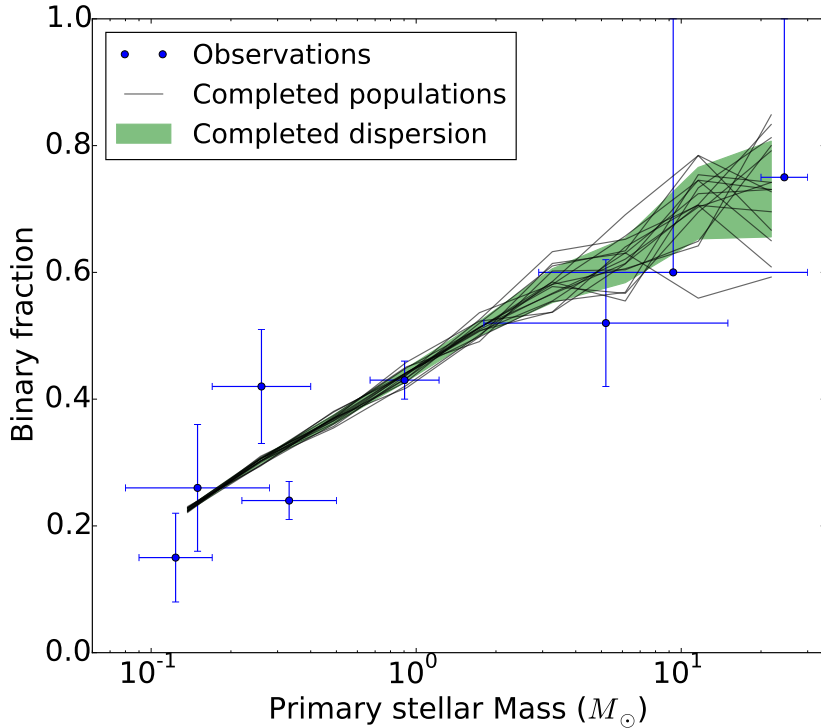


Figure 6.7: Binary fraction as a function of primary mass. The results displayed are the average of twenty realisations for 20k particles models; the shade indicates 1- σ deviations. Short semi-major axis binaries were injected to complete the spontaneous population (compare with Fig ??).

primary. (Several of these heavy spontaneous binaries with large separation no longer satisfy Eq 6.3). No massive binaries were introduced to compensate for this effect, which remains relatively small. The values derived for this range of primary masses remain in complete agreement with observational data.

Turning to the distribution of semi-major axis, we choose to truncate the injected binary population at short semi-major axis. Extensive numerical exploration of binary tidal heating has been performed by one of us (O. Roos 2012, unpublished). Binaries were put on highly eccentric orbits in cuspy Dehnen (1993) potentials, so experiencing large variations in the tidal force. It was found the binary's binding energy varied by $\approx 50\%$ or more only when the semi-major axis $a > 100$ AU. No binary-single stars or binary-binary interactions were included. The conclusion from this study is that binaries with axis a shorter than 100 AU should rarely unbind due to tidal heating. Further tests with NBODY6, and the results of the next section, largely confirm this. With that in mind, and in view of the computational costs, we truncated the binary population at $a = 1$ AU. This choice allows to recover the range found in ? SPH calculations, so a closer parallel can be made with his setup.

We show on Fig 6.8 in short-dashed the full spontaneous binary population (with a peak value at $a \approx 7000$ AU), prior to the procedure to split fused binaries. The distribution of separations for the fused binaries is shown as the long-dashed blue curve, with a dip around $a \approx 10000$ and 2000 AU for low and high density. Finally, the splitting procedure is carried out, and the result shown as the solid green curve. The grey shade is the expectation value for the parametrised Gaussian distribution of Raghavan et al. (2010). Discrepancies with this distribution are only significant for binaries with $a > 4000$ AU for both densities. For low-density models, the peak of the spontaneous population, still visible after the splitting procedure, introduces an excess of binaries for (roughly) $4000 < a < 20000$ AU. Note how the excess of binaries in that range

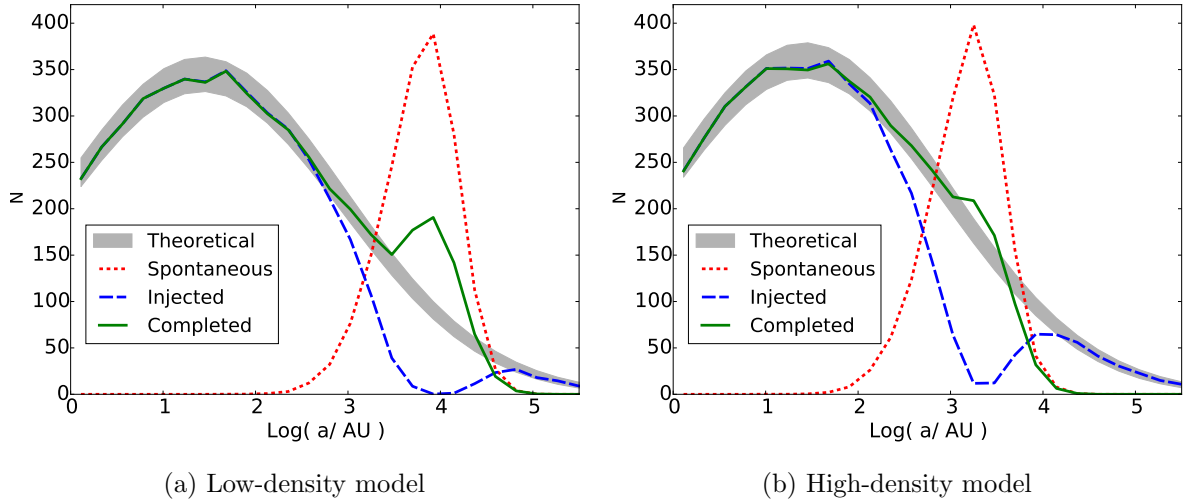


Figure 6.8: Distributions of binary separations for the completion of a population in low and high density models. Spontaneous binaries before splitting are shown in short-dashed red, the population injected in the system in long-dashed blue and the resulting measured distribution in the completed system in green. The observational separation distribution from [Raghavan et al. \(2010\)](#) is shown as a grey area, taking into account Poisson dispersion.

has been halved by the splitting procedure, dropping from a maximum of ≈ 370 to ≈ 170 . For the high-density model, as the spontaneous population is shifted towards short separation, their inclusion is easier and they only introduce a slight bump in the distribution at $a \sim 2000$ AU.

For larger separations, the very wide binaries are not identified by the density threshold algorithm and are dropped from consideration. Since none of them is likely to survive for a long period of time given the density of the system, this will have no bearing on our conclusions.

While Hubble-Lemaitre fragmentation allows to obtain a self-consistent phase space distribution for a substructured model, the population completion presented here preserves this consistency by taking into account naturally occurring multiple systems, while allowing the user to inject a realistic binary population.

In the next chapter, we use the resulting, completed systems as initial conditions to investigate the evolution of a binary population during the violent relaxation of a clumpy configuration.

CHAPTER 7

The evolution of the binary population

In this chapter, the fragmented HL models with a completed binary population from the previous chapter are left to evolve. The binary population is monitored to evaluate the influences of membership and density on the processing of binaries in a substructured configuration. In the end of the simulation, we detect very short and very wide binaries; we detail their dynamical origins and the possible implications for binary formation.

Contents

7.1	Results	94
7.1.1	Total binary fraction	94
7.1.2	Binary fraction vs primary mass	96
7.1.3	Semi-major axis distributions	98
7.1.4	Tidal shocks	100
7.2	Extreme tight- and wide binaries	101
7.2.1	Tight binaries	101
7.2.2	Wide binaries	104

A system bound gravitationally will resist external tidal forces if it sits within its Roche radius ([Binney & Tremaine 2008](#), §8; [Renaud, Gieles & Boily 2011](#)). For binary stars, the condition for boundedness is given by Eq. (6.3) with $D = 3$ and setting the mean density ρ_{bin} over the full Jacobi volume. Thus the question of how much the mean background density rises and compares to the mean density of the binary has important consequences for the further evolution of the binary. The situation is made more complicated if the host’s potential changes rapidly, on the dynamical time-scale t_{cr} of Eq. (1.5).

Let us first recall the results of the collapse of an homogeneous sphere of N identical stars. For this case the sphere collapses by a factor C before it rebounds and evolves towards equilibrium ([Aarseth, Lin & Papaloizou, 1988](#); [Boily, Athanassoula & Kroupa, 2002](#)). The ratio of minimum radius achieved during collapse, to the initial system radius, is a 1/3 power-law of N , so $C \propto N^{-1/3}$. If the total mass is conserved during the collapse, the mean background density scales as $\rho \propto C^{-3}$ and so reaches a peak value $\max(\rho) \propto N$. Based on this analysis, one would expect a strong relation between the system *total* mass $M = N\bar{m}$ and the rate of destruction of binary stars, especially those of large semi-major axis a , if and when a cluster undergoes a phase of collapse.

To investigate this effect of membership on the destruction rate, various simulations were performed: their parameters are summarized in Table 7.1. Runs with N ranging from 1500 to 80000 were sampled in such a way that ensemble-averaging gave roughly the same Poissonian

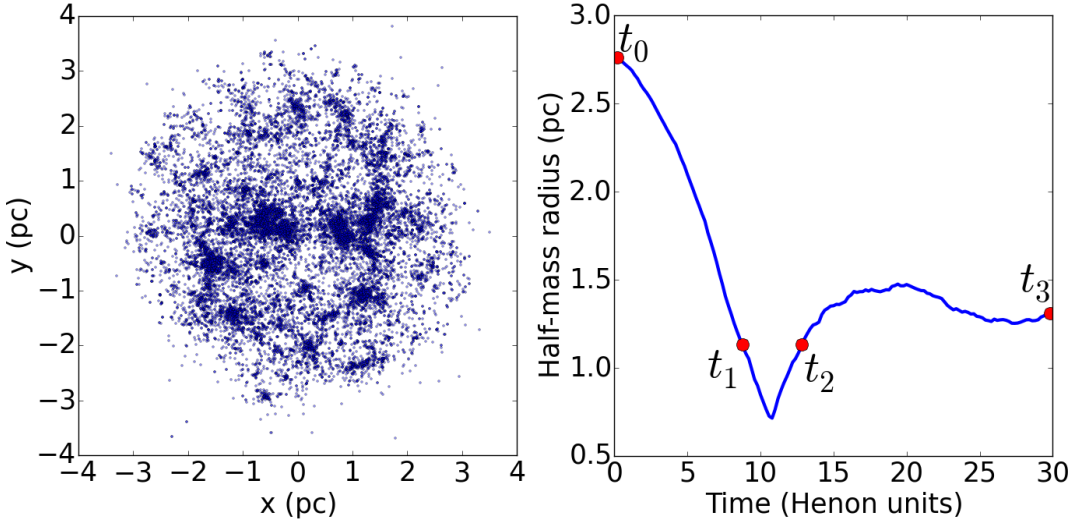


Figure 7.1: Left panel: spatial distribution of a Hubble-Lemaître fragmented model. Right panel: evolution of the half-mass radius over time. The times labelled as t_0 to t_3 are the system configurations used in §4 for analysis.

Table 7.1: Summary of simulations. Starting from an HL fragmented configuration, a binary population was injected to complete the spontaneous binaries, reaching an overall binary fraction of 0.42. Densities within half-mass radius are shown at $t=0$ and time of deepest collapse.

Name	N	Sampling	$\rho_{h,0}$ (pc $^{-3}$)	$\rho_{h,max}$ (pc $^{-3}$)
R1.5h	1500	40	400	$1.7 \cdot 10^3$
R5h	5000	10	400	$4.0 \cdot 10^3$
R20h	20000	10	400	$1.4 \cdot 10^4$
R80h	80000	1	400	$7.1 \cdot 10^4$
R1.5l	1500	40	6	13
R5l	5000	10	6	79
R20l	20000	10	6	192
R80l	80000	1	6	10^3

standard deviations in each case. All models underwent the binary population completion procedure described in the previous chapter, with the two reference densities 6 pc^{-3} and 400 pc^{-3} .

The aspect of a 20k star models with high density, R20h in Tab 7.1, is shown on the left panel of Fig. 7.1, while the evolution of its half-mass radius over time is shown on the right panel. Four epochs of interest are shown as red dots: t_0 , the initial conditions; t_1 , end of collapse and before the bounce; t_2 , just after the bounce; t_3 30 H.u, the system reached quasi-equilibrium. These will be reference epochs throughout this chapter.

7.1 Results

7.1.1 Total binary fraction

We show on Fig. 7.2 the evolution of the binary fraction in HL fragmented systems as a function of time. The time when the systems rebounds from the global in-fall, $t \approx 10$ units, is marked

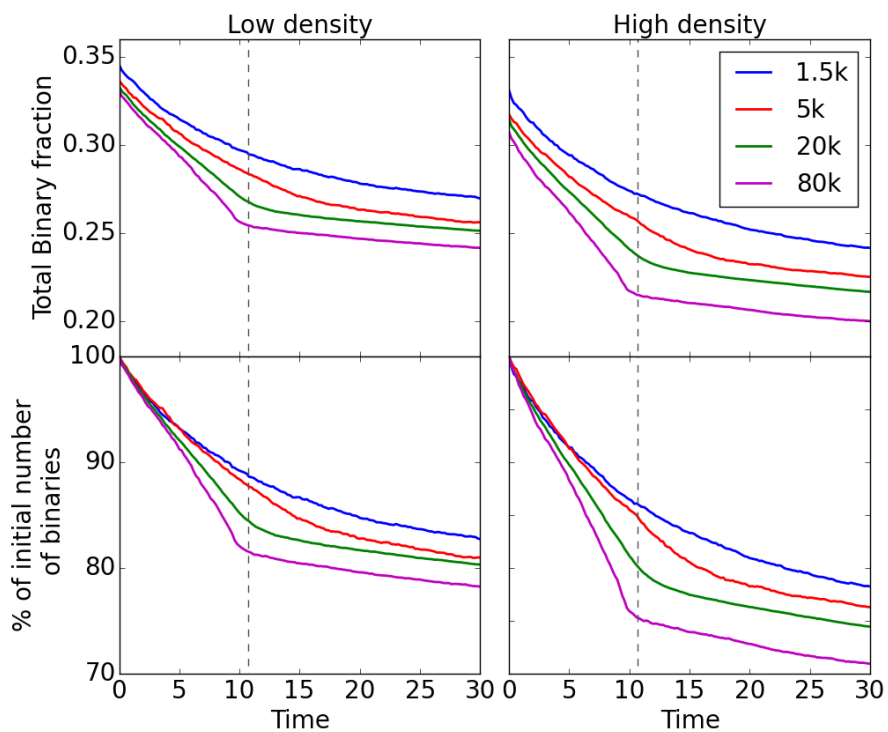


Figure 7.2: Top panels: total binary fraction over time for different cluster memberships. Lower panels: total number of binary over time compared to initial number in each system, in percentage. The vertical dashed line indicates the time of deepest collapse.

with a vertical dotted line on each frame. The binary fraction decays in each case during the course of evolution, regardless of their membership N or initial density. All systems display two different regimes of binary destruction, before and after the bounce from global collapse. Before the bounce, binaries are destroyed at a higher average rate, the more so for the more massive systems (large N). After the bounce ($t > 10$) the slopes all flatten out and binaries are continuously destroyed but at a lower rate. For example, the R80h simulation removes 2.5% of its binaries per time unit before the collapse; this rate goes down to 0.25% afterwards. Similarly, the low-density $N = 80k$ run has 1.7% before the collapse and 0.16 % thereafter.

We interpret these findings as follows. In the first stages of evolution, the rate of binary destruction is driven by the two-body relaxation in the small clumps of the HL configuration. To see this, Fig. 7.2, bottom row, graphs the *relative* fraction of surviving binaries for each model. The linear slope is virtually identical up to $t \approx 5$ units. The internal dynamics of clumps is independent of the larger system in which they are embedded. As collapse proceeds, larger N systems develop a deeper global potential well: this is easier to see for $t \rightarrow 10$ as the curves fan out. The range, of about 10%, accrued at $t = 10$ between runs of different N , is almost unchanged at the end of the simulations, at $t = 30$ units. The rate of binary destruction post-bounce is practically the same for all N , though note that it remains higher for the high-density calculations (the final count of binaries drops from $\simeq 80\%$ at low density, to $\simeq 70\%$ at high density).

There is a clear tendency for the pre- and post-collapse transition to be sharper as N increases. We interpret this in the light of Eqs. (1.5) and (1.6). We note that the $N = 1.5k$ models are dominated by two-body interactions, the mass-segregation time-scale drops to ~ 1 time units, and not by the overall collapse motion that drives density upwards, destroying binaries. At the other end of the spectrum, the $N = 80k$ models have a global mass-segregation time-scale > 30 time units. These models, like all the others, are initially dominated by two-body interactions in their clumpy substructures. However the later evolution sees the overall collapse motion take over. It is the imprint of that global in-fall which allows the density to peak at higher values (cf. Table 7.1) and laminate binaries more efficiently around that time. Since the re-bound is of short duration, the strong tidal field drops quickly as we shift in the post-bounce phase.

7.1.2 Binary fraction vs primary mass

To determine whether the evolution affects binaries differently according to their mass, we show on Figs. 7.3 and 7.4 the binary fraction in relation to the primary mass. Results are shown at four different times, and for all runs of N . The top row of each figure is the binary fraction f_m and the bottom row the percentage of binaries with respect to the initial distribution. This representation highlights which binaries are the most processed in the system. The panels for $t = t_1$ and t_2 are for times immediately before and after the bounce (cf. Fig. 7.1). The dynamical evolution within the clumps and during the collapse impacts preferentially light-primary binaries; binaries with a more massive primary (say, $> 5M_\odot$) survive better. We stress that the trends are indicative and at the $\sim 20\%$ level in all cases. Bearing this caveat in mind, inspection of the different cases does suggest that the results for low- N runs are more the result of the internal dynamics of clumps, where star-star interactions would favour the ejection/destruction of low-mass binaries. Note how the low- N models in fact form *additional* high-mass binaries during in-fall, since the binary fraction exceeds 100% at $t = t_1$ and t_2 . This is not so for the $N = 20k$ and $80k$ models, which we interpret as due to the stronger tidal fields in these models which stops new binaries from forming. It is interesting that despite the deeper infall achieved by these large- N models, the trend of increased survival with primary mass is not eradicated: this would have been the case had the external (global) tidal field clearly dominated the binary destruction. Instead, we find that the strong fields do not erase memory of the early evolution phase of the clumpy distribution.

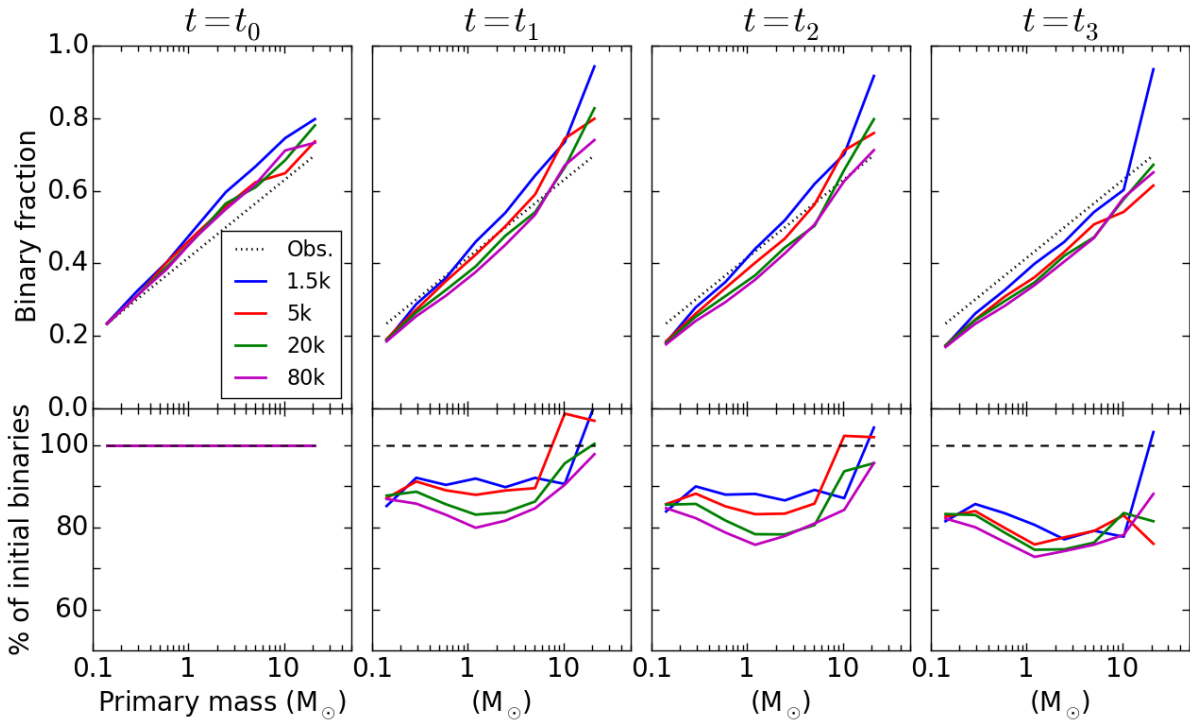


Figure 7.3: The data is from low density models. Top panels show the binary fraction in logarithmic bins for the primary masses. Dotted line show the linear fit to observations shown in Fig. 6.5. In bottom panels, the number of binaries in each primary mass bin is shown as a percentage of the initial number ($t=0$). The 100% value is shown as a horizontal dashed line.

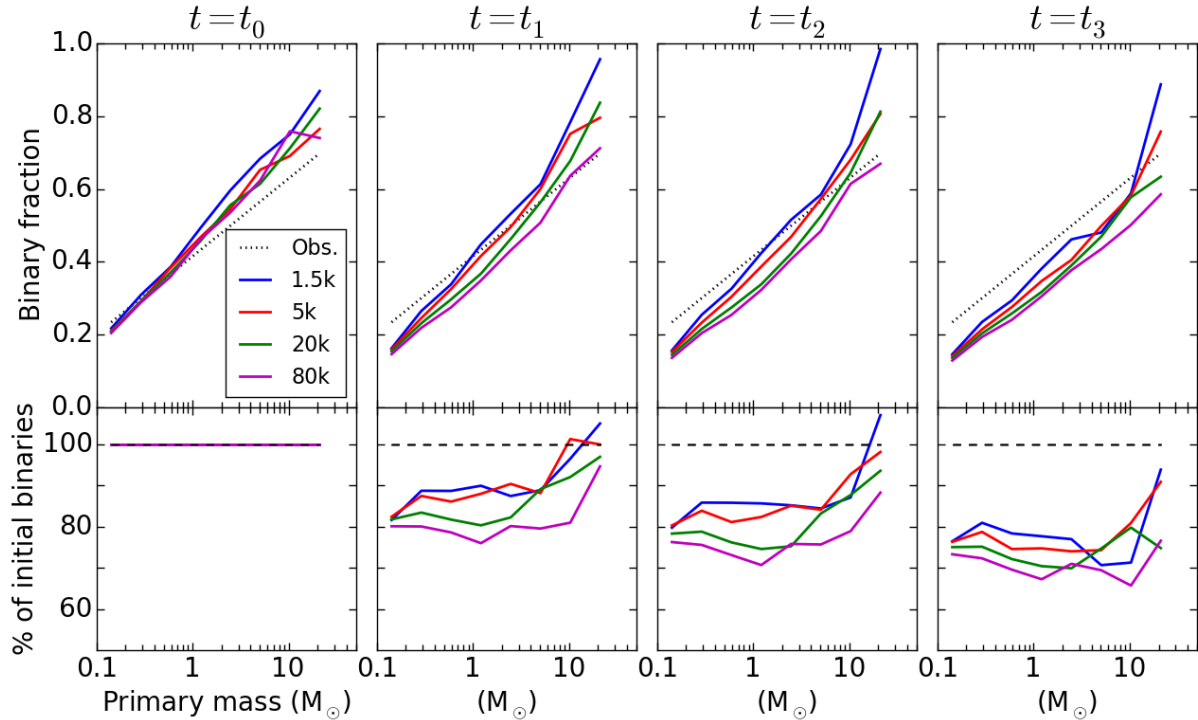


Figure 7.4: The data from high density models. Same key as Fig. 7.3.

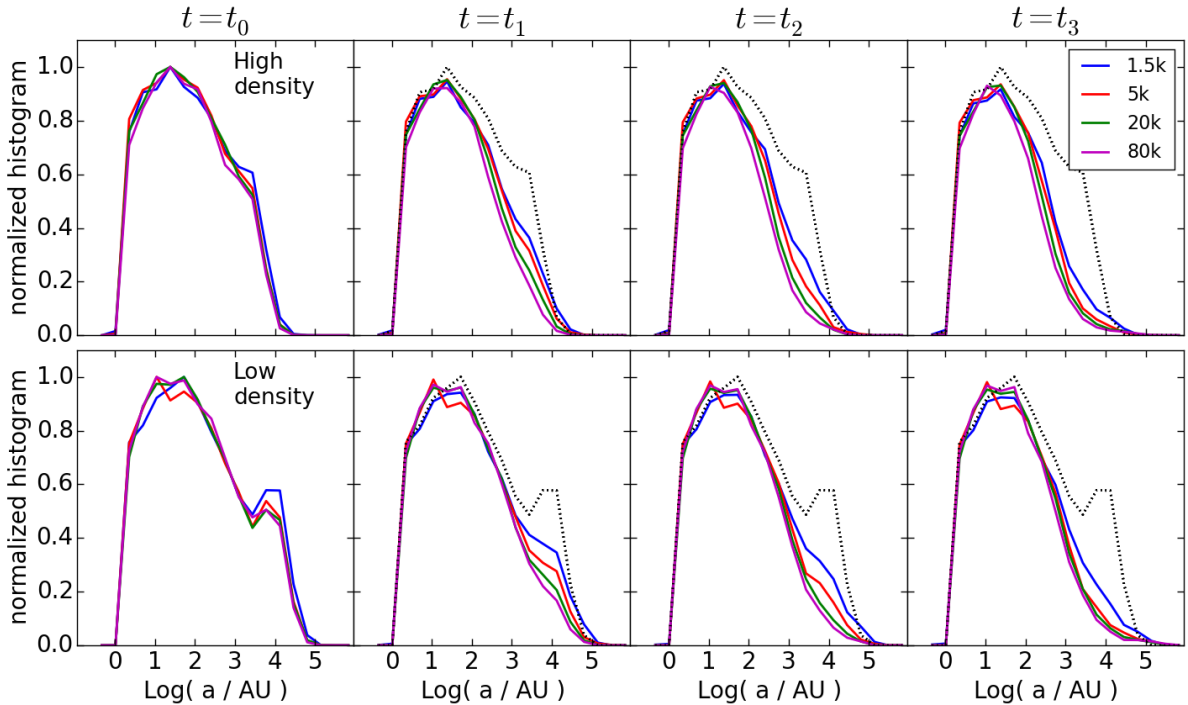


Figure 7.5: Histograms of semi-major axes for the binary population at four different times and for four different cluster membership. The dotted black line shows the distribution of $N = 1.5k$ models at $t = 0$ as a reference for the initial distributions. High density models are in the top row, while low density models are in the bottom row. The reference times are taken from Fig. 7.1.

The results for the later time $t = t_3$ displayed coincides with the end-time of the simulations. At that point all models have reached equilibrium and the binaries have been processed dynamically in such a way that the binary fraction decreased monotonically for all primary masses. It is worth noting that the low-density models (Fig. 7.3) have evolved for a physical time $t \approx 18$ Myr, while the high density ones (Fig. 7.4) up to $t \approx 3$ Myr only. This may explain the greater scatter among the different runs for these models (they have more intense tidal fields but have less time to act on the binaries). We also note that the peak at high primary mass, clearly visible at $t = t_2$, is still apparent at $t = t_3$, except for the case $N = 80k.$, which is the model with the highest density and the strongest tidal field. We interpret this as indicating that the wide binaries have had time to be split, while this process is yet incomplete in the other models. This view is backed up from inspection of the low-density runs at $t = t_3$ on Fig. 7.3, where all the peaks seen at $t = t_2$ have been flattened save the runs with $N = 1.5k$. We believe that the more stochastic low- N runs may have produced more wide-binary escapers due to their shallower potential well. These would therefore not be processed collisionally in the final cluster and survive in isolation.

7.1.3 Semi-major axis distributions

The evolution of the distribution of semi-major axes a in a binary population hinges on its dynamical environment. Several analytical and numerical studies (Heggie, 1975; Kroupa, 1995a,b; Heggie, Trenti & Hut, 2006; Parker et al., 2009; Parker, Goodwin & Allison, 2011) have shown that wide, weakly bound binaries are preferentially disrupted, so sculpting the distribution towards tighter, more bound binaries. This evolution is shown on Fig. 7.5 which graphs the

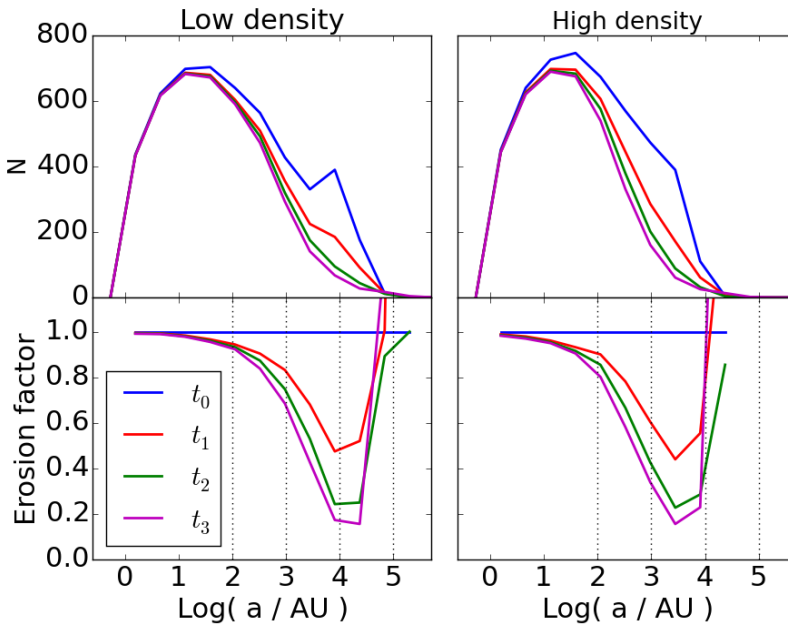


Figure 7.6: Top panels: histogram of semi-major axis at four different times for the $N = 20k$ models. Bottom panels shows the erosion factor, the ratio between the sizes of the initial binary population and the one at a given time, in each primary mass bin.

distribution histograms as a function of semi-major axis a . The distributions are plotted for four various times, membership N and both the values of initial density. The averaged distribution computed from the models with $N = 1.5k$ is shown as a dotted line and serves as reference. To ease the comparison between models with different N , all histograms were normalized to the reference initial profile at $t = 0$ (e.g., the area under the curve is the same for all the models).

We first distinguish between high- and low-density models. The overall behaviour of the models is the same, with a rapid dissolution of large semi-major axis binaries, $a \sim 10^3$ AU or more. This takes place prior to the bounce, when $t < t_1$ but is a continued trend from the start of the computations to the end. As anticipated, high density models (top row on Fig. 7.5) process the binary population more efficiently, reaching deeper in the short-axis range, down to $a \sim 20$ AU, compared to $a \sim 100$ AU for the low density models. This can be gauged qualitatively by the gap that opens up between the dotted line and the histograms.

The system mass (or membership N) has little influence on the evolution of the histograms, however, as the collapse factor C increases with N , the larger N models process significantly wider $a \sim 10^3$ AU binaries ; this is true regardless of the initial density (high or low). Note that, here too, the $N = 1.5k$ models stand out, in the sense that their wide binary population is less efficiently processed.

Having identified the mean initial density as the main driver for binary population evolution, we wish to compare the rate of survival of binaries with the analytical approach by [Marks, Kroupa & Oh \(2011\)](#). These authors introduced an analytic operator acting on a binary population to mimick its evolution in a host star cluster, dispensing with N-body simulations. [Marks & Kroupa \(2012\)](#) used this framework to reproduce the destruction of wide binaries, using the operator as an "erosion factor" applied to a birth semi-major axis distribution, selectively reducing the number of binaries in each semi-major axis bin (see their Fig. 1 for an illustration of their approach). The erosion factor is bound to the interval $[0, +1]$, and equals one when all binaries of a given semi-major axis a are retained (zero when they are all destroyed).

The erosion factors arising from $N = 20k$ simulations for the four reference times are dis-

played on Fig. 7.6 (bottom panels). The model with initially high density heats up and splits binaries of (relatively) shorter semi-major axis during the collapse, and beyond: the most dramatic phase of evolution between times t_0 and t_2 . During that interval, nearly 80% of binaries with $a > 100$ AU are split. There is comparatively little evolution from t_2 to t_3 , which covers the remaining *half* of the run time. The run of the erosion factor with a and its time-evolution are very similar when comparing the runs of models with high- and low initial density. The most striking difference is the shift of the minimum value of the erosion factor, from a semi-major axis $a \approx 3000$ AU, to larger axes $a \approx 10000$ AU in the case of low density models. The extent of the shift, a factor of 4, is consistent with the scaling of the mean separations between stars $l \propto \rho^{-1/3}$; we compute for high and low density systems

$$\frac{l_{low}}{l_{high}} = \left(\frac{\rho_{high}}{\rho_{low}} \right)^{1/3} = \sqrt[3]{\frac{400}{6}} \simeq 4. \quad (7.1)$$

This fact alone implies that the evolution of fragmented mass profiles through a relaxation phase is driven mostly by stellar encounters. The same conclusion applies for the evolution of the fractal models of Parker, Goodwin & Allison (2011). The late stages of cluster formation, post-bounce and nearly in virial equilibrium, compare well with the analytical operator of Marks & Kroupa (2012). One significant difference that this approach does not factor in is the formation of wide binaries in the post-bounce phase. The operator may still adequately compute the evolution of a binary population in a system in global equilibrium. Nevertheless, expanding low-density volumes and other phenomena related to the virialisation phase appear to be outside the scope of a cluster-wide binary-processing analytical operator.

7.1.4 Tidal shocks

We noted how larger- N simulations tend to iron out a larger fraction of binaries (see Fig. 7.5). The weak trend with increasing N implies that both star-star interactions (including multiple stars) and global tidal forces both boost the heating up and unbinding of binaries. The shift seen on Fig. 7.4 is small but systematic: from 15% for $N = 1.5k$, to 25% for $N = 80k$ of all binary stars are destroyed at the bounce ($t \approx 10$ units). To get a better appreciation for the trend (or lack thereof) with N , let us compute the energy transferred to a binary star by the tidal field. At the end of the collapse, the stars move on mostly radial orbits at high velocities. Since they cross a dense region in a short time, we make use of the tidal shock approximation developed by Spitzer (1958, see also Boily et al. 2004; Binney & Tremaine 2008).

Taking inspiration from the tidal shock suffered by a cluster crossing the galactic disk, we can get an estimation of tidal heating on a binary crossing the dense center of the system at the time of deepest collapse. Binney & Tremaine (2008) define the change of specific binding energy ΔE_s of a self-gravitating system of size r , mass μ , crossing a spherical volume of projected surface density $\Sigma \approx r\rho$ at radial velocity V_r , as:

$$\Delta E_s = \frac{14\pi^2 G^2 \Sigma^2 r^2}{3V_r^2}. \quad (7.2)$$

We seek out the scaling of this relation with the number of stars N , keeping the system initial mean density $\rho(0)$ constant. This implies that the total mass $M \propto N$. The expectation from the analysis of fragmentation modes is that the radius at the bounce $r = R_o/N^{1/3}$. The projected density at the bounce therefore scales as $\Sigma \approx M/\pi r^2$. Ignoring mass loss and the energy dissipated by binary disruption, we can estimate the magnitude of the square radial velocity V_r^2 from the relation

$$3V_r^2 \approx \frac{2GM}{r} \propto \frac{N}{N^{-1/3}R_o}. \quad (7.3)$$

Substituting in (7.2) and replacing r by the semi-major axis, we find

$$\Delta E_s = \frac{14\pi G^2 (M/\pi r^2)^2 a^2}{2GM/r} \propto \frac{GM a^2}{r^3} \propto \frac{GM}{R_o^3} N a^2. \quad (7.4)$$

The binding energy per unit mass of a binary star is $E_s = -G\mu/2a$. The relative energy imparted to the binary by the shock is therefore

$$\frac{\Delta E_s}{E_s} \approx \frac{7\pi M}{\mu R_o^3} a^3 N. \quad (7.5)$$

We chose to keep the initial mean system density constant, so that the ratio $M/(\mu R_o^3)$ is independent of N . The final scaling reads

$$\frac{\Delta E_s}{E_s} \propto a^3 N. \quad (7.6)$$

An increase in membership N implies more significant heating of the binary star. If we set $\Delta E_s/E_s = 1$, then an increase of $N \rightarrow 10 \times N$ should have the same relative effect on a binary of semi-major axis $a \rightarrow a/10^{1/3} \approx a/2.15$. By implication, the peak of the distributions seen on Fig. 7.5 should shift from $a \approx 40$ AU to $a \approx 40/3.76 = 10.64$ AU, as we work up from $N = 1.5k$ to $N = 80k$ calculations. This shift is not seen on the figure. What we see, on the other hand, is that large- N systems tend to deplete more efficiently the wide binaries, so that at the same stage of evolution, the richer systems have a binary distribution that falls off more quickly at large separations. We attribute the weak dependence on N to the approximation of a static background mass distribution¹. In reality, the whole structure moves on the same short dynamical time-scale of Eq. (1.5) and hence the effective surface density Σ is much reduced if the system as a whole begins to re-expand. We suspected that the choice of fixed initial density may be the reason for the undetectable shift of the peak on Fig. 7.5. Our choice of initial conditions imply that the system size $R_o \propto M^{1/3}$; had we chosen instead to use an empirical relation such as $R_o \propto M^{1/5}$ for stellar clusters (Larsen, 2004), then we would have found a scaling of $\Delta E_s/E_s \propto a^3 N^{7/5}$. The same rise in N as before would have produced a shift from ≈ 40 AU to 6.5 AU in the peak of the distribution, and this is still too large to go undetected.

7.2 Extreme tight- and wide binaries

As mentioned in § 6.2.2, Bate (2012) has found several examples of binaries reducing their separation over time through stellar encounters, from ~ 10 AU down to $\lesssim 0.5$ AU. Tighter systems were hindered by numerical resolution issues. The regularised treatment of close encounters (which allows to integrate up to machine precision) of the code NBODY6 means that the same collisional process will be at play in the calculations that we have performed. Since no binaries with semi-major axis a shorter than 1 AU was inserted in the initial conditions, we focus first on the statistics of binaries that evolved to $a < 1$ AU. In the second part of this section, we will explore the formation and the evolution of very wide ($a > 10^4$ AU) binaries, many of which end up loosely bound to the stellar cluster as a whole.

7.2.1 Tight binaries

Several binaries with $a < 1$ AU were detected at the end of the low-density simulations. By comparison, almost none developed in the high-density runs. Their properties are summarised in the left panel of Fig. 7.7. The data is taken from $N = 20k$ runs but similar statistics were obtained for the other setups. The top row shows the binary mass as a function of semi-major axis, while the bottom row on that figure graphs the distance of their barycentre to the center

¹The original treatment by Spitzer fixed a thin (vertically mixed) disc crossed by a stellar cluster at high speed.

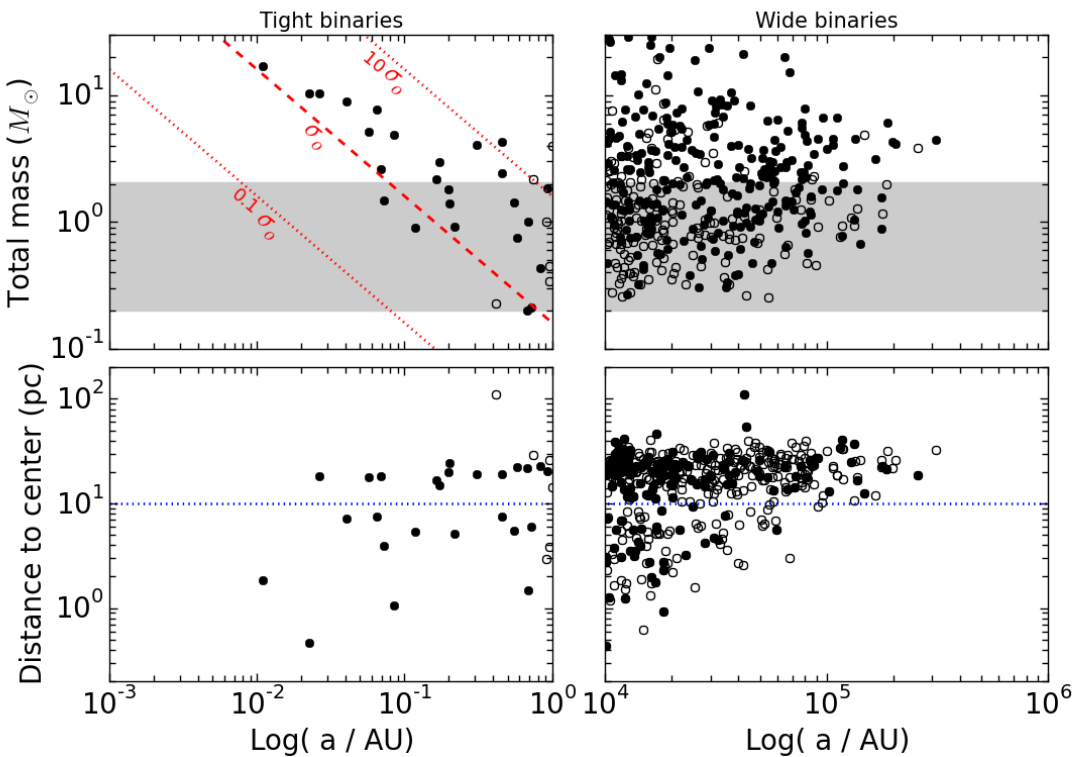


Figure 7.7: Left panels: Total binary mass (top) and distance to center of the cluster (bottom) versus the semi-major axis for binaries tighter than 1AU at the end of the simulation. Right panels: same layout for binaries wider than 10^4 AU. The greyed area in the top panels shows the 90% probability range of a binary total mass from random pairing given the present IMF. The red dashed line in the top left panel shows the relation for constant $v_{\infty}^2 \sigma_{\text{coll}} \equiv \sigma_0$; it is bounded by two dotted curves that have $10\sigma_0$ (above) and $0.1\sigma_0$ (below). The horizontal dotted line in the bottom panel indicates the boundary between the ejecta (distance to center > 10 pc) and the central system. Open circles are binaries which already existed at $t=0$. The data is from 10 simulations of $N = 20k$ stars with initial mean density of $6/\text{pc}^3$.

of the cluster. Open circles denote binaries that already existed at $t=0$, and became tighter over time, while filled circles are *new* binaries that formed in the course of the simulation. Inspection of these new, tight binaries shows that *both* of their components were part of binaries originally inserted in the system. Thus all new tight binaries shown on Fig. 7.7 are the results of strong binary-binary interactions leading to splitting or exchange. (None of the original binaries that survived to the end of the simulation had $a < 1/2$ AU.)

The statistics of these events should be compared with expectations based on estimated collision rates. The time-scale for direct collisions between particles in a self-gravitating system depends on the degree of gravitational focusing of the colliding bodies (Binney & Tremaine 2008, section 7.5.8, Eq. 7.195a). This is given quantitatively by the Safronov number $\Theta = v_*^2/4\sigma^2 = GM/(4\sigma^2a)$, where we have replaced the surface escape velocity v_* of a single star by the unbinding velocity $v^2 = GM/a$ of a binary of total mass M and separation a . To obtain an estimate of Θ , we looked at typical clump parameters from the $N = 20k$ R20l models: an average membership of $N_c \sim 50$ stars and mean half-mass radius $r_h \sim 0.2pc$ yield an internal velocity dispersion (subtracting the binaries' internal motion) $\sigma \sim 0.5 \text{ km.s}^{-1}$. Setting a binary mass $M > 2M_\odot$ and semi-major axis $a = 1 \text{ AU}$ yields $\Theta \simeq 3700 \gg 1$. The collisional rate τ_{coll}^{-1} for binary disruption is then:

$$\begin{aligned}\tau_{coll}^{-1} &= 16\sqrt{\pi}n\sigma a^2\Theta \\ &= 8 \times 10^{-4} \text{ Myr}^{-1} \frac{n}{700\text{pc}^{-3}} \frac{0.5\text{km.s}^{-1}}{\sigma} \frac{a}{\text{AU}} \frac{M}{2M_\odot}\end{aligned}\quad (7.7)$$

with n the stellar number density $\sim 700 \text{ pc}^{-3}$. This rough estimate of the collision rate should be interpreted as a lower limit because in practice $a > 1\text{AU}$ and many binaries have a total mass $> 2M_\odot$. We find $\tau_{coll}^{-1} \sim 8 \times 10^{-4}$ collisions per clump per Myr. Since on average $\simeq 150$ clumps formed in each R20l run, and assuming that the collision rate is constant throughout the 6 Myr in-fall time, then we expect of order $O(1)$ hard encounters per 10^4 stars. If most of these interactions lead to the disruption of the binaries, some others will result in exchange and tighter components.

These statistics are in good agreement with the identification in the ten $N = 20k$ runs of a total of 24 binaries with $a < 0.6 \text{ AU}$, for an average of $2.4/5000 \approx 0.05\%$ of all *binary* stars ($f_b \approx 1/3$ at $t = 0$). The very tight binaries each have a combined mass exceeding $2M_\odot$ with a low mass ratio q , ranging from 0.01 up to 0.2. It is important to mention that main sequence binary stars with a separation $a \lesssim 0.02 \text{ AU}$ would be *contact* binaries when both members are solar-type or more massive stars. Clearly the evolution of such object (and in fact their formation process) calls for hydrodynamical effects that were not included in our study. It is therefore remarkable that contact binaries should form strictly through gravitational scattering on such short timescales.

These results apply to runs with initial mean number density of $6/\text{pc}^3$. The same analysis carried out for the higher density models give a different outcome. For these models, the initial density is larger by a factor ~ 60 and the velocity dispersion by a factor ~ 2 , for all stars. From (7.8), we find a collisional rate ~ 30 times higher than previously. If direct collisions were the main channel for the formation of tight binaries, the number of events should increase in the same proportions. However, inspection of the simulations yielded only 4 tight binaries, each with a semi-major axis $a \gtrsim 0.1 \text{ AU}$. Thus the rate of formation of tight binaries drops to 0.4 per 5000 binaries, or 0.008%, a six-fold decrease. We argue that two factors hinder the formation of these objects in high density environment. First, Geller & Leigh (2015) pointed out that exchange encounters between single stars and binaries are not instantaneous (see also ?). The process can be perturbed by other stars, so modifying the outcome of the collisions. This is also true for binary-binary collisions: casual inspection of the time series of (tight) binary stars showed that their mean separation keeps evolving throughout the evolution of the model, which suggest

that the binaries are part of a small-N hierarchical system. It is reasonable to expect that more hierarchical systems will develop in a higher-density environment (involving more stars) and so the exchange process may never have time to take place.

Secondly, the binary exchange binary cross-section is sensitive to the impact velocity. The lack of a detailed theoretical framework on binary-binary collisions makes it difficult to pin down statistical expectations with precision. In the case of a disruptive encounter between a binary + single stars, extensive analytical work by [Mikkola \(1983, 1984a,b\)](#) and numerical scattering experiments (e.g., [Heggie, Hut & McMillan 1996; Fregeau et al. 2004](#)) lead to a rough estimate of the effective scattering cross section σ_{bin} in relation to the mass and separation of identical binaries:

$$\sigma_{coll} \propto \frac{m_t a}{v_\infty^2}. \quad (7.8)$$

In this equation, σ_{coll} is the effective collisional cross-section for disruption in binary-single interactions, and v_∞ is the relative velocity at infinity (prior to the collision) \approx the clump velocity dispersion. Taking $v_\infty \approx \sigma = \text{constant}$ independent of mass and binary separation, we may use (7.8) to relate binary mass M to separation a and cross-section σ_{coll} . [Hut & Bahcall \(1983\); Hut \(1983\)](#) gave analytical expressions for the *exchange* cross sections, which scales as the above scattering cross-section at low velocities, but becomes steeper for higher velocities:

$$\sigma_{ex} \propto \frac{m_t a}{v_\infty^6}. \quad (7.9)$$

As the encounter velocity increases, it becomes harder and harder to perform a successful exchange. The two initial mean densities that we picked may therefore cover the transition from low- to high-velocity regimes, and reduce the number of tight binaries created to just a handful.

Going back to Fig. 7.7, we plot the relation $v_\infty^2 \sigma_{coll} \equiv \sigma_0$ of (7.8) as straight red lines on the top-left panel. Two dashed curves bracket a curve in full type, each with a value of σ_{coll} differing by a multiplicative factor of ten (increasing from the lower curve, up). The large separations between the curves and the clustering of data points along the full curve indicate how a single value of σ_0 effectively cuts through the diagramme in two well-delimited regions. Thus the trend of binary mass increasing as $M \propto 1/a$ for the most tight binaries is consistent with a constant product of $\sigma_0 = v_\infty^2 \sigma_{coll}$ at the time of formation.

7.2.2 Wide binaries

The formation of wide ‘spontaneous’ binaries during the HL fragmentation process leads one naturally to expect that more wide binaries will form in the post-collapse evolution of the system, when expanding streams of stars emerge from the compact bounce to form a tenuous halo. We already noted how the erosion factor on Fig. 7.6 shoots up for large semi-major axes, exceeding unity at the later stages of evolution in both high- and low density calculations. This implies either that a sub-set of wide binaries got softer over time, or that new binaries of separation $> 10^4$ AU formed during the virialisation phase. If we compare the numbers for axes $a > 5.10^4$ AU $\simeq 0.25$ pc and for all ten $N = 20k$ models, then there were 120 binaries more in this range at the end of the simulations, then right after the bounce, at time $t = t_2$. Of those 120, some forty new binaries formed in the expanding volume, while eighty are soft binaries that became softer as a result of collisional evolution, the well-known Heggie law ([Heggie, 1975; Hills, 1975](#)). While these numbers of very wide binaries are very low indeed, a ratio of 120 per $10 \times 20k$ stars (0.06%), they are still significant because they would be associated with neighbouring star-forming regions, and may yet register as correlations in phase-space coordinates.

The right-hand panels of Fig. 7.7 graph the basic properties of this sub-set of extreme wide binaries. We selected all binaries with separations exceeding 10^4 AU, the largest semi-major axes that were found in the initial conditions. Hence all data points shown here are the result of some evolutionary mechanism. The horizontal dotted line on Fig. 7.7 marks a distance of

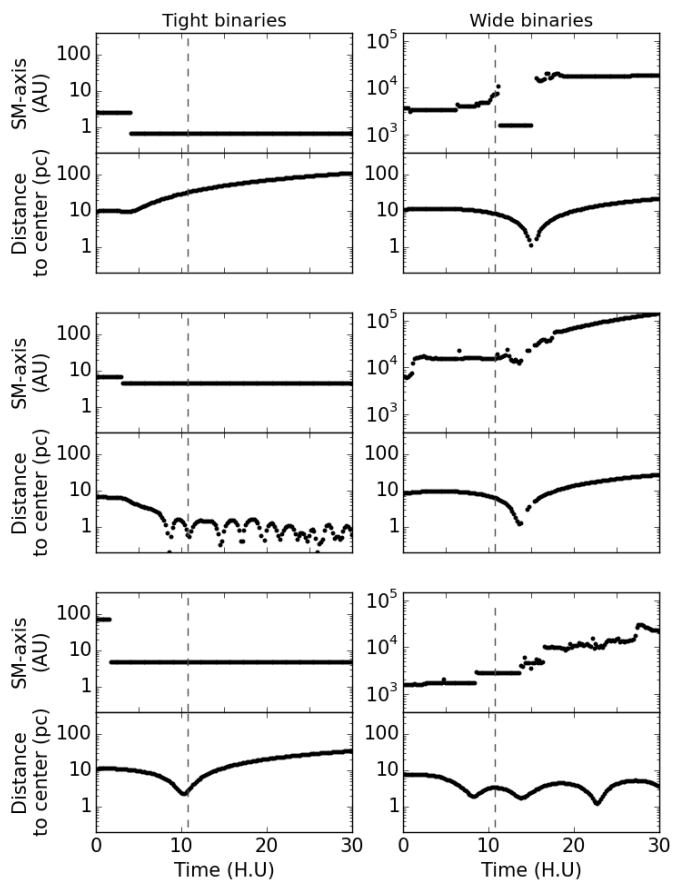


Figure 7.8: Evolution of individual binaries semi-major axis and distance to center over time in the low density 20k particles models. The vertical dashed line marks the moment of deepest collapse $t \simeq (t_1 + t_2)/2$.

10 pc as the separation between the central equilibrium cluster and the volume where weakly bound ejecta orbit. Close to $\approx 60\%$ of wide binaries are escaping the main clusters or are very weakly bound to it. Therefore most of them would be lost to the tidal field in a real cluster environment.

We stress that the semi-major axis a of an individual binary star is not a monotonous function of time. Fig. 7.8 graphs the evolution of six perturbed binaries, 3 tight and 3 wide binaries. Tight binaries mostly suffer strong interactions early on, before the collapse, inside a clump. This would take place most likely at the centre of the clump, where the density is higher. What happens next is hard to predict, as the pair can then be ejected from the system by this interaction (e.g. the first binary, top panel); or sink at the center of the cluster and remain there (second binary, middle frame); or follow the bulk of the ejecta, falling once through the core and then leaving the system without further strong interactions (third binary, bottom row). Most wide binaries experience several strong interactions. Many of these take place around the time of the collapse, as they orbit through the dense core of the cluster. These repeated strong interactions will lead to heating and result in binary splitting. That is also why no (spontaneous) wide binary was found in the dense clump cores of the initial HL configuration; instead, they form in the low-density inter-clump space. Practically all wide binaries had a first strong interaction during the densest phase of the in-fall ($t_1 < t < t_2$).

Part III

Perspectives and conclusions

CHAPTER 8

Perspectives

In this thesis we introduced the Hubble-Lemaître fragmentation model and applied to the dynamical evolution of substructured star clusters and the fate of their binary population. Interesting results have been obtained, though some assumptions were made. In this chapter, we review two of these assumptions: the absence of stellar evolution and the isolated nature of the cluster. We also present the outline of a comparison to observations and the possible inclusion of hydrodynamical processes.

8.1 Tidal field

In all our simulations, it was assumed the clusters were in isolation and no tidal field were applied. This allowed to study the mechanisms of violent relaxation and the erasure of substructure. However, in reality, star forming regions are shaped by the gravitational influence of their surroundings. We mentioned in section 3.4 that the galactic tidal field could prevent the collapse of the Hubble-Lemaître fragmented configuration and scatter the clumps, injecting them in the galactic cluster mass function. The fate of these clumps is uncertain, as some will disperse through two-body interactions, and other will merge, depending on the geometry imposed by the tidal field.

Numerical simulations will allow an exploration of the resulting clump mass function, which would be more directly comparable to the cluster mass function. NBODY6 has a built-in galactic tidal field module, which allows to model the tidal forces associated with the cluster orbiting a complex galactic potential, including a [Miyamoto & Nagai \(1975\)](#) potential, see [Aarseth \(2003b\)](#) for details. The tidal shock from a passing molecular cloud is also an option in NBODY6.

However, it is possible to go further in the inclusion of realistic tidal fields. [Renaud, Gieles & Boily \(2011\)](#) introduced a new version of NBODY6, [Nbody6tt](#), that can take an arbitrary tidal tensor as an input and apply it to the evolution of a star cluster. Specifically, Nbody6tt allows to extract the tidal environment of a cluster from a large-scale galactic simulation to obtain a time-dependant, self-consistent tidal field. The influence of different galactic environment, such as tidal arms, on the cluster can then be evaluated.

For example, [Renaud, Bournaud & Duc \(2015\)](#) reported the formation of massive clusters in their hydrodynamical simulation of a galaxy merger analog to the Antennas galaxies. Fig 8.1 show the merging of YMC fragments on large scales. This kind of event could be reproduced in Nbody6tt with a Hubble-Lemaître configuration and the tidal data from the simulation. Given the complex tidal fields in this kind of environment, the evolution of YMCs starting from a substructured initial conditions could shed light of their formation and disruption processes.

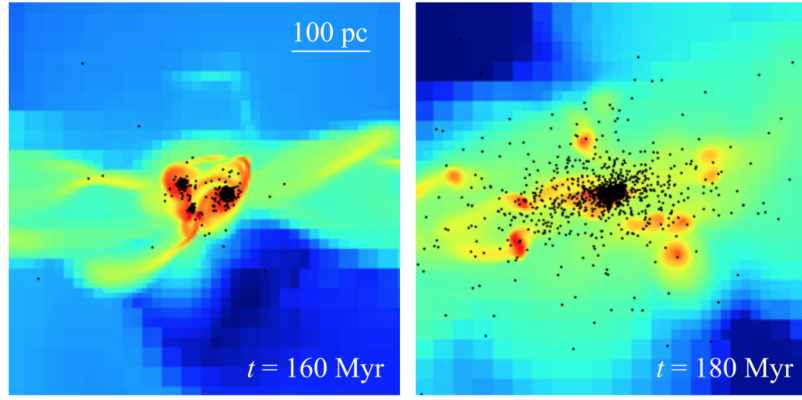


Figure 8.1: Cluster formation in a hydrodynamical simulation of the Antennae galaxies. The colormap indicates gas densities and newly formed stars are shown as black dots. Two epochs are shown, outlining the erasure of substructure. The figure was extracted from [Renaud, Bournaud & Duc \(2015\)](#)

8.2 Stellar evolution

In section 4.1.2 and TODO, we selected the mass ranges to apply to our models, which we justified by the duration of our simulations, arguing the death of our most massive stars would either not happen or not have a significant impact on the evolution. However, in section TODO, we remarked that the inclusion of even more massive stars could be of interest for the formation of new tight binaries.

It comes that one of the most straightforward ways to improve our models is the inclusion of stellar evolution. NBODY6 has a built-in stellar evolution module based on the analytical mode by [Hurley, Pols & Tout \(2000\)](#), including wind-driven mass loss, radii evolution, supernova event and stellar remnants. It was not used in this work for simplicity, but should be used for further research.

In section TODO, we computed free-fall times for models with several initial stellar densities. This corresponds to the lifetimes of clumps, as the collapse and relaxation erase substructure. We then ask to what extent the death of massive stars can affect the dynamics of a single clumps. From [Hurley, Pols & Tout \(2000\)](#), we get stellar lifetimes as a function of mass, shown on Fig 8.2. For low stellar density, clumps can barely outlive massive stars. We showed that for an initial stellar density of 6 stars/ pc^{-3} , the system collapses in 6 Myr, while stars with a mass $> 10M_{\odot}$ live up to 5 Myr.

However, if we include tidal fields, the clumps might survive far longer, and the mass-loss from stellar evolution could have a significant impact on their structures, their mass segregation, and on the overall clump mass function.

8.3 Anisotropic expansion

The Hubble-Lemaître expansion we used throughout this thesis was isotropic, the velocity field was expressed with $\mathbf{v} = H_0 \mathbf{r}$ with H_0 a scalar value. As a result, the fragmented configurations are roughly spherical and the net systemic angular momentum is null. This is a key difference between the method we have developed and the fractal approach of ?. Angular momentum may be significant in young clusters such as R136 ([Hénault-Brunet et al., 2012](#)). In a fractal model, the way the velocity field is built leaves a residual, global angular momentum whereas the Hubble approach starts off with strictly zero angular momentum.

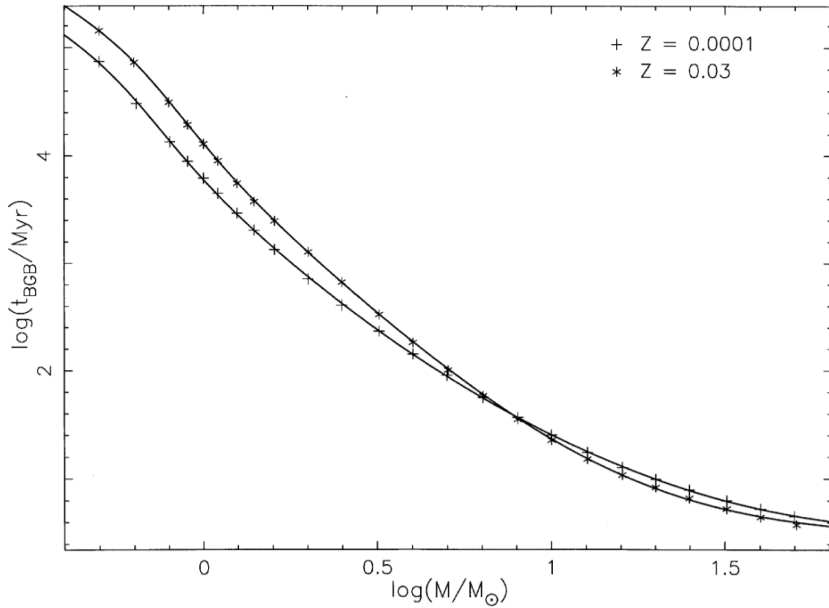


Figure 8.2: Time taken to reach the Base of the Giant Branch (BGB) as a function of initial stellar mass, for two metallicities, $Z = 0.0001$ and $Z = 0.03$. The figure was extracted from [Hurley, Pols & Tout \(2000\)](#)

A net angular momentum could be introduced in a Hubble model, for instance by setting

$$\mathbf{v} = \mathbf{H}_o \mathbf{r} + \boldsymbol{\Omega} \times \mathbf{r} \quad (8.1)$$

with $\boldsymbol{\Omega}$ a chosen angular velocity. One can actually go further and write in matrix form

$$\mathbf{v} = \mathbf{H} \mathbf{r}, \quad (8.2)$$

with \mathbf{H} now a 3×3 matrix, where the off-diagonal elements account for rotation and the elements on the diagonal H_{ii} control the three dimensional expansion. In this study, we have set $H_{ij, i \neq j} = 0$ and $H_{ii} = H_o$ otherwise. It is then a simple matter to study the fragmentation along a filament by setting, for example, $H_{xx} = H_{yy} = 0$ and $H_{zz} > 0$. The Hubble fragmentation process for young stellar cluster is a new method and many of its aspects remain to be explored.

As mentioned earlier, recent observations confirmed the prevalence of filamentary structure in star formation processes ([André et al., 2010](#)).

Bibliography

Bibliography

- Aarseth S. J., 1972, in BAAS, Vol. 4, Bulletin of the American Astronomical Society, p. 417
- Aarseth S. J., 1999, PASP, 111, 1333
- Aarseth S. J., 2003a, Ap&SS, 285, 367
- Aarseth S. J., 2003b, Gravitational N-Body Simulations. p. 430
- Aarseth S. J., 2012, MNRAS, 422, 841
- Aarseth S. J., Hénon M., Wielen R., 1974, A&A, 37, 183
- Aarseth S. J., Hoyle F., 1964, Astrophysica Norvegica, 9, 313
- Aarseth S. J., Lin D. N. C., Papaloizou J. C. B., 1988, ApJ, 324, 288
- Aarseth S. J., Turner E. L., Gott, III J. R., 1979, ApJ, 228, 664
- Aarseth S. J., Zare K., 1974, Celestial Mechanics, 10, 185
- Adams F. C., 2000, ApJ, 542, 964
- Ahmad A., Cohen L., 1973, Journal of Computational Physics, 12, 389
- Allison R. J., Goodwin S. P., Parker R. J., de Grijs R., Portegies Zwart S. F., Kouwenhoven M. B. N., 2009a, ApJ, 700, L99
- Allison R. J., Goodwin S. P., Parker R. J., Portegies Zwart S. F., de Grijs R., 2010, MNRAS, 407, 1098
- Allison R. J., Goodwin S. P., Parker R. J., Portegies Zwart S. F., de Grijs R., Kouwenhoven M. B. N., 2009b, MNRAS, 395, 1449
- Andersen M., Zinnecker H., Moneti A., McCaughrean M. J., Brandl B., Brandner W., Meylan G., Hunter D., 2009, ApJ, 707, 1347
- Anderson J., Piotto G., King I. R., Bedin L. R., Guhathakurta P., 2009, ApJ, 697, L58
- André P., Belloche A., Motte F., Peretto N., 2007, A&A, 472, 519
- André P. et al., 2010, A&A, 518, L102
- Ashman K. M., Zepf S. E., 1992, ApJ, 384, 50
- Bacon D., Sigurdsson S., Davies M. B., 1996, MNRAS, 281, 830
- Barker P., Dear P., Christianson J. R., Westman R. S., 2014, Metascience, 23, 203
- Barnes E. I., Lanzel P. A., Williams L. L. R., 2009, ApJ, 704, 372

-
- Barnes J., Hut P., 1986, Nature, 324, 446
- Barrow-Green J., 1997, Poincaré and the Three Body Problem, History of mathematics No. vol. 2. American Mathematical Society
- Basri G., Reiners A., 2006, AJ, 132, 663
- Bastian N., Covey K. R., Meyer M. R., 2010, ARA&A, 48, 339
- Bastian N., Goodwin S. P., 2006, MNRAS, 369, L9
- Bate M. R., 2009, MNRAS, 392, 590
- Bate M. R., 2012, MNRAS, 419, 3115
- Bate M. R., Bonnell I. A., Bromm V., 2003, MNRAS, 339, 577
- Bate M. R., Burkert A., 1997, MNRAS, 288, 1060
- Bate M. R., Tricco T. S., Price D. J., 2014, MNRAS, 437, 77
- Bédorf J., Portegies Zwart S., 2012, European Physical Journal Special Topics, 210, 201
- Belorizky D., 1930, Bulletin Astronomique, 6, 417
- Benhaiem D., Sylos Labini F., 2015, MNRAS, 448, 2634
- Binney J., Tremaine S., 2008, Galactic Dynamics (2nd ed.). Princeton Univ. Press, Princeton, NJ
- Boily C. M., Athanassoula E., Kroupa P., 2002, MNRAS, 332, 971
- Boily C. M., Kroupa P., 2003a, MNRAS, 338, 665
- Boily C. M., Kroupa P., 2003b, MNRAS, 338, 673
- Boily C. M., Nakasato N., Spurzem R., Tsuchiya T., 2004, ApJ, 614, 26
- Bonnell I. A., Bate M. R., Vine S. G., 2003, MNRAS, 343, 413
- Bonnell I. A., Vine S. G., Bate M. R., 2004, MNRAS, 349, 735
- Bressert E. et al., 2010, MNRAS, 409, L54
- Brodie J. P., Strader J., 2006, ARA&A, 44, 193
- Cambrésy L., 1999, A&A, 345, 965
- Caputo D. P., de Vries N., Portegies Zwart S., 2014, MNRAS, 445, 674
- Chabrier G., 2005, in Astr. & Space Sci., Vol. 327, The Initial Mass Function 50 Years Later, Corbelli E., Palla F., Zinnecker H., eds., p. 41
- Clagett M., 1959, The science of mechanics in the Middle Ages, University of Wisconsin publications in medieval science. University of Wisconsin Press
- Clarke C., 2012, in Astronomical Society of the Pacific Conference Series, Vol. 453, Advances in Computational Astrophysics: Methods, Tools, and Outcome, Capuzzo-Dolcetta R., Limongi M., Tornambè A., eds., p. 3
- Close L. M., Siegler N., Freed M., Biller B., 2003, ApJ, 587, 407

-
- Cohen I. B., Anne Whitman J. B., 1999, *The Principia: Mathematical Principles of Natural Philosophy*, 1st edn. University of California Press
- Cottaar M. et al., 2015, *ApJ*, 807, 27
- Czekaj M. A., Robin A. C., Figueras F., Luri X., Haywood M., 2014, *A&A*, 564, A102
- Dale J. E., Bonnell I., 2011, *MNRAS*, 414, 321
- Dale J. E., Ngoumou J., Ercolano B., Bonnell I. A., 2013, *MNRAS*, 436, 3430
- Davies B., Figer D. F., Kudritzki R.-P., Trombley C., Kouveliotou C., Wachter S., 2009, *ApJ*, 707, 844
- De Angelis A., Santo C. E., 2015, *Journal of Astronomical History and Heritage*, 18, 241
- de Wit W. J., Testi L., Palla F., Zinnecker H., 2005, *A&A*, 437, 247
- Dehnen W., 1993, *MNRAS*, 265, 250
- Dias W. S., Alessi B. S., Moitinho A., Lépine J. R. D., 2002, *A&A*, 389, 871
- Doppler C., 1842, *ber das farbige Licht der Doppelsterne und einiger anderer Gestirne des Himmels*. Verlag der Knigl. Bhm.
- D'Souza R., Rix H.-W., 2013, *MNRAS*, 429, 1887
- Duquennoy A., Mayor M., 1991, *A&A*, 248, 485
- Ebisuzaki T., Ito T., Makino J., Sugimoto D., 1990, *Astronomical Herald*, 83, 224
- Eddington A. S., 1916, *MNRAS*, 76, 572
- Ehlerova S., Palous J., Theis C., Hensler G., 1997, *A&A*, 328, 121
- Eisenstein D. J., Hut P., 1998, *ApJ*, 498, 137
- Elmegreen B. G., Falgarone E., 1996, *ApJ*, 471, 816
- Elsen E., Houston M., Vishal V., Darve E., Hanrahan P., V. P., 2006, "n-body simulation on gpus."
- Farias J. P., Smith R., Fellhauer M., Goodwin S., Candlish G. N., Blaña M., Dominguez R., 2015, *MNRAS*, 450, 2451
- Field G. B., Goldsmith D. W., Habing H. J., 1969, in BAAS, Vol. 1, Bulletin of the American Astronomical Society, p. 240
- Fischer D. A., Marcy G. W., 1992, *ApJ*, 396, 178
- Fleck J.-J., Boily C. M., Lançon A., Deiters S., 2006, *MNRAS*, 369, 1392
- Foster J. B. et al., 2015, *ApJ*, 799, 136
- Freeman K. C., Block D., Elmegreen B. G., Woolway M., 2015, *Lessons from the local group : a conference in honour of David Block and Bruce Elmegreen*. Springer
- Fregeau J. M., Cheung P., Portegies Zwart S. F., Rasio F. A., 2004, *MNRAS*, 352, 1
- Friedman J. L., Schutz B. F., 1978, *ApJ*, 221, 937

-
- Frisch U., Bec J., Villone B., 2001, Physica D Nonlinear Phenomena, 152, 620
- Fujii M. S., 2015, PASJ, 67, 59
- Fujii M. S., Portegies Zwart S., 2016, ApJ, 817, 4
- Gaczkowski B., Preibisch T., Ratzka T., Roccatagliata V., Ohlendorf H., Zinnecker H., 2013, A&A, 549, A67
- Galileo G., 1610, Sidereus nuncius. Thomas Baglioni
- Garcia M., Herrero A., Castro N., Corral L., Rosenberg A., 2010, A&A, 523, A23
- Geisler D., Lee M. G., Kim E., 1996, AJ, 111, 1529
- Geller A. M., de Grijs R., Li C., Hurley J. R., 2013, ApJ, 779, 30
- Geller A. M., Leigh N. W. C., 2015, ApJ, 808, L25
- Goodwin S. P., Bastian N., 2006, MNRAS, 373, 752
- Goodwin S. P., Whitworth A. P., 2004, A&A, 413, 929
- Goodwin S. P., Whitworth A. P., Ward-Thompson D., 2004, A&A, 423, 169
- Gunawardhana M. L. P. et al., 2011, MNRAS, 415, 1647
- Gutermuth R. A., Megeath S. T., Myers P. C., Allen L. E., Pipher J. L., Fazio G. G., 2009, ApJS, 184, 18
- Gutermuth R. A., Pipher J. L., Megeath S. T., Myers P. C., Allen L. E., Allen T. S., 2011, ApJ, 739, 84
- Haas M. R., Anders P., 2010, A&A, 512, A79
- Harris W. E., 1991, ARA&A, 29, 543
- Harris W. E., 1996, VizieR Online Data Catalog, 7195
- Hartmann L., 2002, ApJ, 578, 914
- Hayashi C., 1961, PASJ, 13
- Heggie D., Hut P., 2003, The Gravitational Million-Body Problem: A Multidisciplinary Approach to Star Cluster Dynamics
- Heggie D. C., 1975, MNRAS, 173, 729
- Heggie D. C., Aarseth S. J., 1992, MNRAS, 257, 513
- Heggie D. C., Hut P., McMillan S. L. W., 1996, ApJ, 467, 359
- Heggie D. C., Trenti M., Hut P., 2006, MNRAS, 368, 677
- Hénault-Brunet V. et al., 2012, A&A, 545, L1
- Hénon M. H., 1971, Ap&SS, 14, 151
- Hillenbrand L. A., Hartmann L. W., 1998, ApJ, 492, 540
- Hills J. G., 1975, AJ, 80, 809

-
- Hills J. G., 1980, ApJ, 235, 986
- Holmberg E., 1941, ApJ, 94, 385
- Houghton H. E., 1942, Monthly Notes of the Astronomical Society of South Africa, 1, 107
- Hoversten E. A., Glazebrook K., 2008, ApJ, 675, 163
- Hubber D. A., Whitworth A. P., 2005, A&A, 437, 113
- Hubble E., 1929, Contributions from the Mount Wilson Observatory, vol. 3, pp.23-28, 3, 23
- Hurley J. R., Pols O. R., Tout C. A., 2000, MNRAS, 315, 543
- Hut P., 1983, ApJ, 268, 342
- Hut P., Bahcall J. N., 1983, ApJ, 268, 319
- Ito T., Ebisuzaki T., Makino J., Sugimoto D., 1991, PASJ, 43, 547
- Jeans J. H., 1916, MNRAS, 76, 567
- Kandori R. et al., 2005, AJ, 130, 2166
- King I. R., 1981, QJRAS, 22, 227
- King R. R., Goodwin S. P., Parker R. J., Patience J., 2012, MNRAS, 427, 2636
- Kirk H., Myers P. C., 2011, ApJ, 727, 64
- Klessen R. S., Burkert A., 2000, ApJS, 128, 287
- Klessen R. S., Burkert A., 2001, ApJ, 549, 386
- Knigge C., Leigh N., Sills A., 2009, Nature, 457, 288
- Könyves V. et al., 2010, A&A, 518, L106
- Korntreff C., Kaczmarek T., Pfalzner S., 2012, A&A, 543, A126
- Kouwenhoven M. B. N., Brown A. G. A., Portegies Zwart S. F., Kaper L., 2007, A&A, 474, 77
- Kouwenhoven M. B. N., Goodwin S. P., Parker R. J., Davies M. B., Malmberg D., Kroupa P., 2010, MNRAS, 404, 1835
- Kragh H., Smith R. W., 2003, History of Science, 41, 141
- Kramer E., 1982, The Nature and Growth of Modern Mathematics, Princeton paperbacks. Princeton University Press
- Krause M. G. H., Charbonnel C., Bastian N., Diehl R., 2016, A&A, 587, A53
- Kroupa P., 1995a, MNRAS, 277
- Kroupa P., 1995b, MNRAS, 277
- Kroupa P., 2002, Science, 295, 82
- Kroupa P., Burkert A., 2001, ApJ, 555, 945
- Kruijssen J. M. D., Maschberger T., Moeckel N., Clarke C. J., Bastian N., Bonnell I. A., 2012, MNRAS, 419, 841

-
- Kuhn M. A., Feigelson E. D., Getman K. V., Sills A., Bate M. R., Borissova J., 2015, ApJ, 812, 131
- Kuhn M. A., Getman K. V., Feigelson E. D., 2015, ApJ, 802, 60
- Kustaanheimo P., Stiefel E., 1965, J. Reine Angew. Math, 218, 204
- Lada C. J., Lada E. A., 2003, ARA&A, 41, 57
- Lada C. J., Margulis M., Dearborn D., 1984, ApJ, 285, 141
- Larsen S. S., 2004, A&A, 416, 537
- Larson R. B., 1969, MNRAS, 145, 271
- Lemaître G., 1927, Annales de la Société Scientifique de Bruxelles, 47, 49
- Lomax O., Whitworth A. P., Hubber D. A., Stamatellos D., Walch S., 2014, MNRAS, 439, 3039
- Lomax O., Whitworth A. P., Hubber D. A., Stamatellos D., Walch S., 2015, MNRAS, 447, 1550
- Mac Low M.-M., Klessen R. S., 2004, Reviews of Modern Physics, 76, 125
- Makino J., 1991, ApJ, 369, 200
- Marks M., Kroupa P., 2012, A&A, 543, A8
- Marks M., Kroupa P., Oh S., 2011, MNRAS, 417, 1684
- Maschberger T., Clarke C. J., 2011, MNRAS, 416, 541
- Maschberger T., Clarke C. J., Bonnell I. A., Kroupa P., 2010, MNRAS, 404, 1061
- Mason B. D., Gies D. R., Hartkopf W. I., Bagnuolo, Jr. W. G., ten Brummelaar T., McAlister H. A., 1998, AJ, 115, 821
- Maury J., 1992, Newton: Understanding the Cosmos, New horizons in history series. Thames and Hudson
- McCrady N., Graham J. R., Vacca W. D., 2005, ApJ, 621, 278
- McKee C. F., Ostriker E. C., 2007, ARA&A, 45, 565
- McMillan S. L. W., Vesperini E., Portegies Zwart S. F., 2007, ApJ, 655, L45
- Merritt D., 2013, Dynamics and Evolution of Galactic Nuclei. Princeton Univ. Press, Princeton, NJ
- Meylan G., Heggie D. C., 1997, A&A Rev., 8, 1
- Mikkola S., 1983, MNRAS, 203, 1107
- Mikkola S., 1984a, MNRAS, 207, 115
- Mikkola S., 1984b, MNRAS, 208, 75
- Mikkola S., Aarseth S. J., 1993, Celestial Mechanics and Dynamical Astronomy, 57, 439
- Miller G. E., Scalo J. M., 1979, ApJS, 41, 513
- Miyamoto M., Nagai R., 1975, PASJ, 27, 533

-
- Moeckel N., Bate M. R., 2010, MNRAS, 404, 721
- Moeckel N., Clarke C. J., 2011, MNRAS, 415, 1179
- Moeckel N., Holland C., Clarke C. J., Bonnell I. A., 2012, MNRAS, 425, 450
- Myers A. T., Klein R. I., Krumholz M. R., McKee C. F., 2014, MNRAS, 439, 3420
- Newton S. I., 1687, Philosophiae Naturalis Principia Mathematica, Vol. 1
- Nitadori K., Aarseth S. J., 2012, MNRAS, 424, 545
- Nyland L., Harris M., Prins J., 2004, "the rapid evaluation of potential fields using programmable graphics hardware."
- Offner S. S. R., Hansen C. E., Krumholz M. R., 2009, ApJ, 704, L124
- Olczak C., Spurzem R., Henning T., 2011, A&A, 532, A119
- Parker R. J., Goodwin S. P., Allison R. J., 2011, MNRAS, 418, 2565
- Parker R. J., Goodwin S. P., Kroupa P., Kouwenhoven M. B. N., 2009, MNRAS, 397, 1577
- Parker R. J., Meyer M. R., 2014, MNRAS, 442, 3722
- Parker R. J., Wright N. J., 2016, MNRAS, 457, 3430
- Patience J., Ghez A. M., Reid I. N., Matthews K., 2002, AJ, 123, 1570
- Pavese F., 2015, ArXiv e-prints
- Peebles P. J. E., 1980, The large-scale structure of the universe. Princeton Univ. Press, Princeton, NJ
- Pelupessy F. I., Portegies Zwart S., 2012, MNRAS, 420, 1503
- Piotto G. et al., 2007, ApJ, 661, L53
- Poincaré H., 1906, Bulletin de la société astronomique de France, 20, 153
- Portegies Zwart S. F., Belleman R. G., Geldof P. M., 2007, New A, 12, 641
- Portegies Zwart S. F., McMillan S. L. W., Gieles M., 2010, ARA&A, 48, 431
- Preibisch T., Balega Y., Hofmann K.-H., Weigelt G., Zinnecker H., 1999, New A, 4, 531
- Press W. H., Teukolsky S. A., Vetterling W. T., Flannery B. P., 2007, Numerical Recipes 3rd Edition: The Art of Scientific Computing, 3rd edn. Cambridge University Press, New York, NY, USA
- Raghavan D. et al., 2010, ApJS, 190, 1
- Ramasubramanian K., 1998, Bulletin of the Astronomical Society of India, 26, 11
- Reipurth B., 2008, Handbook of Star Forming Regions
- Renaud F., Bournaud F., Duc P.-A., 2015, MNRAS, 446, 2038
- Renaud F., Gieles M., 2015, MNRAS, 448, 3416
- Renaud F., Gieles M., Boily C. M., 2011, MNRAS, 418, 759

-
- Rubenstein E. P., Bailyn C. D., 1997, ApJ, 474, 701
- Rybicki J., Just A., 2015, MNRAS, 447, 3880
- Salpeter E. E., 1955, ApJ, 121, 161
- Scalo J., Vázquez-Semadeni E., Chappell D., Passot T., 1998, ApJ, 504, 835
- Schneider S., Elmegreen B. G., 1979, ApJS, 41, 87
- Skory S., Turk M. J., Norman M. L., Coil A. L., 2010, ApJS, 191, 43
- Spitzer L., 1987, Dynamical evolution of globular clusters
- Spitzer, Jr. L., 1958, ApJ, 127, 17
- Springel V. et al., 2005, Nature, 435, 629
- Spurzem R., 1999, Journal of Computational and Applied Mathematics, 109, 407
- Stahler S. W., 2010, MNRAS, 402, 1758
- Strömgren E., 1909, Astronomische Nachrichten, 182, 181
- Sundman K. F., 1912, Acta Mathematica, 36, 105
- Tailo M. et al., 2015, Nature, 523, 318
- Terlevich E., 1980, in IAU Symposium, Vol. 85, Star Clusters, Hesser J. E., ed., p. 165
- Teyssier R., 2002, A&A, 385, 337
- Theis C., Spurzem R., 1999, A&A, 341, 361
- Turner J. A., Chapman S. J., Bhattal A. S., Disney M. J., Pongracic H., Whitworth A. P., 1995, MNRAS, 277, 705
- Tutukov A. V., 1978, A&A, 70, 57
- van Albada T. S., 1968a, Bull. Astron. Inst. Netherlands, 20, 57
- van Albada T. S., 1968b, Bull. Astron. Inst. Netherlands, 20, 40
- van den Bergh S., 2011, JRASC, 105, 197
- von Hoerner S., 1960, ZAp, 50, 184
- von Hoerner S., 1963, ZAp, 57
- von Hoerner S., 2001, in Astronomical Society of the Pacific Conference Series, Vol. 228, Dynamics of Star Clusters and the Milky Way, Deiters S., Fuchs B., Just A., Spurzem R., Wielen R., eds., p. 11
- Wang L. et al., 2016, MNRAS, 458, 1450
- Wang L., Spurzem R., Aarseth S., Nitadori K., Berczik P., Kouwenhoven M. B. N., Naab T., 2015, MNRAS, 450, 4070
- Ward-Duong K. et al., 2015, MNRAS, 449, 2618
- Weidner C., Kroupa P., Bonnell I. A. D., 2010, MNRAS, 401, 275

-
- Weidner C., Kroupa P., Pflamm-Altenburg J., 2013, MNRAS, 434, 84
- White S. D. M., Rees M. J., 1978, MNRAS, 183, 341
- Whitmore B. C. et al., 2010, AJ, 140, 75
- Whitmore B. C., Schweizer F., 1995, AJ, 109, 960
- Wright N. J., Parker R. J., Goodwin S. P., Drake J. J., 2014, MNRAS, 438, 639
- Wünsch R., Dale J. E., Palouš J., Whitworth A. P., 2010, MNRAS, 407, 1963
- Yoccoz J. C., 2010, La Lettre du Collège de France, 28, 38
- Zepf S. E., Ashman K. M., 1993, MNRAS, 264, 611

APPENDIX A

NBODY6

NBODY6 is the second youngest iteration of the NBODY family, a suite of n-body integrators created by Sverre Aarseth. It can compute the gravitational interaction between up to 128,000 stars in a collisional fashion, meaning there is no softening of the potential, at any scale. This allows for very close binaries to form and remain in the system. To achieve its impressive performances, NBODY6 relies on several optimization technique which have been first developed in the 1960s and 1970s, and improved ever since. Here will be developped four major features of NBODY6, in chronological order of their implementation: block time-step, KS-regularization, Hermite scheme and Ahmad-Cohen neighbour scheme. A full description can be found in Sverre Aarseth's book ([Aarseth, 2003b](#)). Inspiration for this section should be credited to the user manual of NBODY6++, written by Emil Khalisi and Rainer Spurzem.

A.1 Block time-step

In the first Nbody simulations, the system was integrated with an universal time-step, determined by the most accelerated star. A star in the outer regions of the cluster with a small velocity did not need to be updated that often. One of the first improvement was the introduction of individual time-step: each star is attributed its own time-step, depending on the force that is applied to it and its derivatives:

$$\Delta t_i = \eta \sqrt{\frac{|\mathbf{F}_i||\mathbf{F}_i^{(2)}| + |\mathbf{F}_i^{(1)}|^2}{|\mathbf{F}_i^{(1)}||\mathbf{F}_i^{(3)}| + |\mathbf{F}_i^{(2)}|^2}} \quad (\text{A.1})$$

With $\mathbf{F}_i^{(j)}$ begin the j-th derivative of the force applied to particle i and η a user-defined accuracy parameter. Such a complex formulation is the result of extensive tests and is quite robust for many special cases. Individual time-steps leads to desynchronized particles, hence the need to interpolate the positions of other particles to compute \mathbf{F}_i , which was achieved through fourth-order polynoms.

To limit the amount of desynchronization, block-time steps were introduced. Instead of having as many time steps as particles, one only allows quantized power of 2 of an initial time step. $\Delta t_0, \frac{\Delta t_0}{2}, \frac{\Delta t_0}{4}, \frac{\Delta t_0}{2^i}$. All time steps are then commensurate and regularly fall back on the same time steps, minimizing the amount of interpolation during the force calculations. The concept is illustrated on Fig [A.1](#).

A.2 KS-regularization

Close binaries are extremely problematic in N-body simulations. They require a small time step as both binary components are much more accelerated than any other stars in the system, while

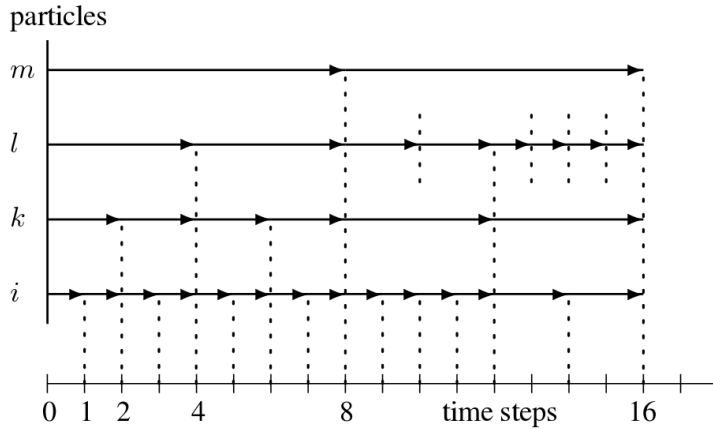


Figure A.1: Illustration of block time steps on 4 particles. Particles get their positions updated for each arrow symbol, common time steps are shown as vertical dotted lines. Figure from NB6++ User Manual.

the rest of the system is unaffected. Block time-step mitigate this problem, but the binary system still requires a lot of integration for an orbit that is essentially already known. Regularization is an answer to this problem. The essence of regularization is to decouple the integration of a sufficiently isolated sub-system, changing its coordinates to make integration easier, and including perturbations from external bodies. Several regularization scheme exist, NBODY6 implemented the Kustaanheimo-Stiefel method, or KS ([Kustaanheimo & Stiefel, 1965](#)).

Two bodies are candidates for regularization when their impact parameter is lower than the one needed for an orthogonal deviation, wherein their trajectory are deviated of 90° :

$$b_{\perp} = 2G \frac{m_1 + m_2}{v_{\infty}^2} \quad (\text{A.2})$$

with m_i components masses and v_{∞} relative velocity before encounter. This impact parameter can be converted to a time step computed through equation [A.1](#):

$$dt_{min} = \kappa \frac{\eta}{0.03} \left(\frac{r_{min}^3}{\langle m \rangle} \right)^{\frac{1}{2}}. \quad (\text{A.3})$$

To be actually regularized, two bodies have to have a mutual time step lower than dt_{min} and fulfill two conditions:

$$\mathbf{R}_r \cdot \mathbf{V}_r > 0.1 \sqrt{G(m_1 + m_2) R_r} \quad (\text{A.4})$$

$$\frac{|\Delta \mathbf{F}_r| \cdot R_r^2}{G(m_1 + m_2)} < 0.25. \quad (\text{A.5})$$

\mathbf{R}_r and \mathbf{V}_r being the relative velocities and positions of the particles and $|\Delta \mathbf{F}_r|$ the differential force applied to them, or perturbation. These conditions mean the subsystem is dynamically decoupled from external influence, but not unperturbed. When they are satisfied, the subsystem is regularized: components are fused in a single particle at the system's center of mass in the global system, while the internal dynamics of the pair are computed separately, with a set of changed coordinates. These coordinates are tailored for binary motion and close approach, they are well behaved when $R_r \rightarrow 0$. The influence of perturbers is taken into account when necessary. When the perturbation ratio (left hand side of equation [A.5](#)) drops below a certain value, the system is considered isolated and it is not computed anymore, its parameters being stored until the perturbation is strong enough to warrant integration.

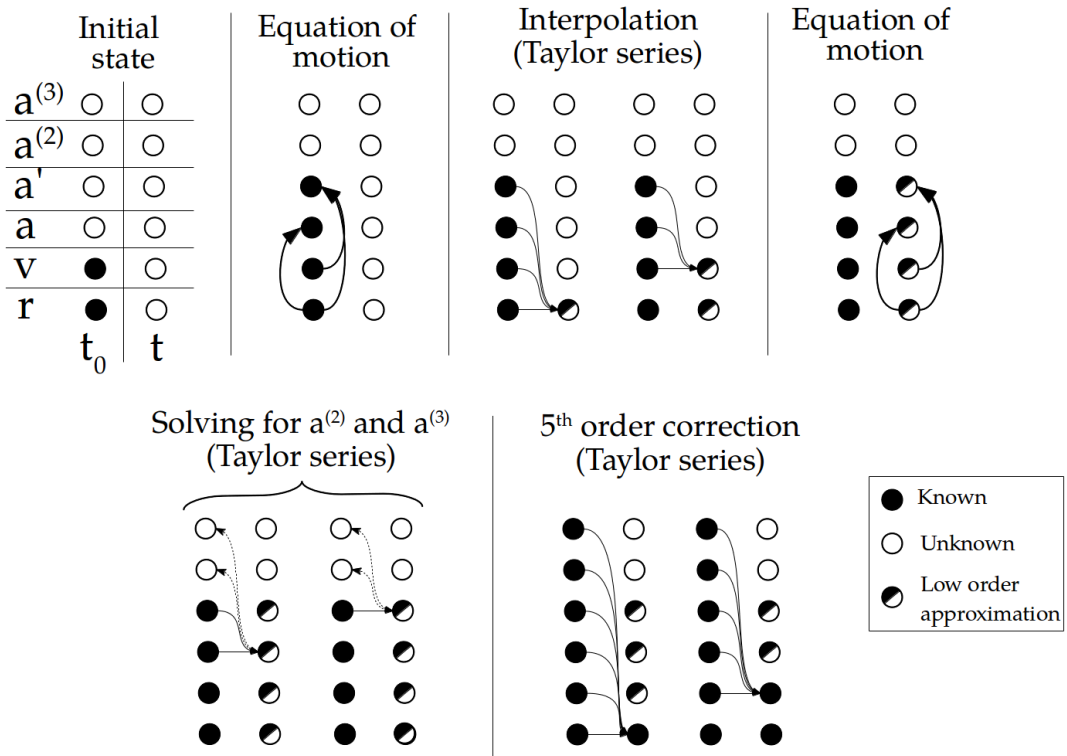


Figure A.2: Summary of the Hermite scheme starting from known positions and velocities at t_0 to obtain 5th order values at t .

Regularisation have been extended to 3 and 4 bodies in hierarchical subsystems. NBODY6 can handle the regularization of a small-n non-hierarchical subsystem following the chain algorithm, see [Mikkola & Aarseth \(1993\)](#).

A.3 Hermite integration scheme

On the appropriate time-scales, the accelerations of the particles in a nbody system vary smoothly. It is therefore possible to predict the future acceleration then to correct the prediction, achieving high order integration with limited computational cost. The Hermite integration scheme was first introduced by [Makino \(1991\)](#) and has since been implemented within NBODY6 ([Aarseth, 2003b](#); [Nitadori & Aarseth, 2012](#)).

The first step is to compute the acceleration and its derivative at $t = t_0$, for all particles i :

$$\mathbf{a}_{0,i} = - \sum_{i \neq j} Gm_j \frac{\mathbf{R}}{R^3} \quad (\text{A.6})$$

$$\dot{\mathbf{a}}_{0,i} = - \sum_{i \neq j} Gm_j \left[\frac{\mathbf{V}}{R^3} + \frac{3\mathbf{R}(\mathbf{V} \cdot \mathbf{R})}{R^3} \right] \quad (\text{A.7})$$

with $\mathbf{R} = \mathbf{r}_{0,i} - \mathbf{r}_{0,j}$ and $\mathbf{V} = \mathbf{v}_{0,i} - \mathbf{v}_{0,j}$. Using these quantities, it is now possible to predict the positions and velocities at t through a Taylor serie, again for all particles i :

$$\mathbf{r}_{p,i}(t) = \mathbf{r}_0 + \mathbf{v}_0(t - t_0) + \mathbf{a}_{0,i} \frac{(t - t_0)^2}{2!} + \dot{\mathbf{a}}_{0,i} \frac{(t - t_0)^3}{3!} \quad (\text{A.8})$$

$$\mathbf{v}_{p,i}(t) = \mathbf{v}_0 + \mathbf{a}_{0,i}(t - t_0) + \dot{\mathbf{a}}_{0,i} \frac{(t - t_0)^2}{2!} \quad (\text{A.9})$$

The predicted accelerations and their derivatives $\mathbf{a}_{p,i}(t)$, $\dot{\mathbf{a}}_{p,i}(t)$ are computed by injecting $\mathbf{r}_{p,i}(t)$ and $\mathbf{v}_{p,i}(t)$ into equations A.6 and A.7. The accelerations at t , of which predicted values have just been computed, can also be obtained through Taylor series:

$$\mathbf{a}_i(t) = \mathbf{a}_{0,i} + \dot{\mathbf{a}}_{0,i}(t - t_0) + \mathbf{a}_{0,i}^{(2)} \frac{(t - t_0)^2}{2!} + \mathbf{a}_{0,i}^{(3)} \frac{(t - t_0)^3}{3!} \quad (\text{A.10})$$

$$\dot{\mathbf{a}}_i(t) = \dot{\mathbf{a}}_{0,i} + \mathbf{a}_{0,i}^{(2)}(t - t_0) + \mathbf{a}_{0,i}^{(3)} \frac{(t - t_0)^2}{2!} \quad (\text{A.11})$$

with $\mathbf{a}_{0,i}^{(2)}, \mathbf{a}_{0,i}^{(3)}$ the third and fourth derivative of the acceleration at $t = 0$. Note that these quantities are unknown for now. To take the derivatives of equation A.7 would be too computationnaly expansive. Instead, $\mathbf{a}_{p,i}(t)$ and $\dot{\mathbf{a}}_{p,i}(t)$ are injected in the left hand side of equations A.10 and A.11 and solved for $\mathbf{a}_{0,i}^{(2)}$ and $\mathbf{a}_{0,i}^{(3)}$. This leads to the expressions:

$$\mathbf{a}_{0,i}^{(3)} = 12 \frac{\mathbf{a}_{0,i} - \mathbf{a}_{p,i}}{(t - t_0)^3} + 6 \frac{\dot{\mathbf{a}}_{0,i} - \dot{\mathbf{a}}_{p,i}}{(t - t_0)^3} \quad (\text{A.12})$$

$$\mathbf{a}_{0,i}^{(2)} = -6 \frac{\mathbf{a}_{0,i} - \mathbf{a}_{p,i}}{(t - t_0)^2} - 2 \frac{2\dot{\mathbf{a}}_{0,i} + \dot{\mathbf{a}}_{p,i}}{t - t_0}. \quad (\text{A.13})$$

The predicted values of positions and velocities are then corrected using the second and third order derivatives of acceleration, yeilding fifth order accurate values.

$$\mathbf{r}_{c,i}(t) = \mathbf{r}_{p,i}(t) + \mathbf{a}_{0,i}^{(2)} \frac{(t - t_0)^4}{4!} + \mathbf{a}_{0,i}^{(3)} \frac{(t - t_0)^5}{5!} \quad (\text{A.14})$$

$$\mathbf{v}_{c,i}(t) = \mathbf{v}_{p,i}(t) + \mathbf{a}_{0,i}^{(2)} \frac{(t - t_0)^3}{3!} + \mathbf{a}_{0,i}^{(3)} \frac{(t - t_0)^4}{4!} \quad (\text{A.15})$$

$$(\text{A.16})$$

In a nutshell, the Hermite scheme is a way to obtain 5th order terms with limited cost. The steps are summarised in figure A.2. First $r_0^{(2)}$ and $r_0^{(3)}$ are computed, then used to obtain predictions of $r_t^{(0)}$ and $r_t^{(1)}$, transformed with the equations of motions into predictions of $r_t^{(3)}$ and $r_t^{(4)}$. These last two can be expressed through Taylor series as functions of $r_0^{(3)}, r_0^{(4)}$ and $r_0^{(5)}$, which are solved for these last two terms. The predicted values of $r_t^{(0)}$ and $r_t^{(1)}$ are then corrected to the fifth order with $r_0^{(4)}$ and $r_0^{(5)}$.

The error for a single time step scales as $O(\Delta t^6)$. The Hermite scheme has shown itself very well suited for the block time step method, as the synchronization of particles limit the amount of prediction to be made, many positions at a given time being already known and computed with maximum accuracy.

A.4 Ahmad-Cohen neighbour scheme

For a given particle in an nbody system, the influence of direct neighbours changes on shorter timescales than the smooth potential from distant particles. The essence of the Ahmad-Cohen neighbour scheme is to decouple the two for computational efficiency (Ahmad & Cohen, 1973). The acceleration is split into two components:

$$\mathbf{a}_i = \mathbf{a}_{i,reg} + \mathbf{a}_{i,irr} \quad (\text{A.17})$$

$\mathbf{a}_{i,irr}$ is the acceleration from particles inside a given "neighbour sphere" around particle i , while $\mathbf{a}_{i,reg}$ is the acceleration from all other, more distant, particles. Integration within the

neighbours sphere, *irregular* integration, is decoupled from the global, *regular*, integration. Regular time steps, where complete force summation are performed over all particles with eq A.6, are subdivided into irregular time steps, where regular acceleration is predicted and irregular acceleration is computed through a force summation on the $N_{i,nb}$ neighbours. The list of neighbours of i is updated every regular time step and contains the particles within a sphere of radius $R_{i,s}$ centered on i . Also added to the neighbour list are the particles within $2^{\frac{1}{3}}R_{i,s}$ that satisfy the condition

$$\mathbf{R} \cdot \mathbf{V} < 0.1 \frac{R_s^2}{\Delta T_{reg}} \quad (\text{A.18})$$

with ΔT_{reg} the regular time step. This ensures that fast approaching particles are selected before they enter the actual neighbour sphere. $R_{i,s}$ is determined through local number density contrast and optimisation of the resulting $N_{i,nb}$.

When $N_{nb} \ll N$ for most particles, there is a great performance improvement and a minimal loss of accuracy.

APPENDIX B

Binary completion algorithm

The Hubble-Lemaître expansion gives rise to a spontaneous binary population detailed in section ???. This population has a deficit of low-mass primary binaries compared to observed binary populations. Moreover, the semi-major axis of spontaneous binaries are too large compared to the canonical period/semi-major axis distribution from [Raghavan et al. \(2010\)](#).

We aim at injecting new binaries in the system to reproduce the characteristics of observed populations. The injected population should be designed to "fill" the discrepancy spontaneous/observed for low-mass primaries and short separations. In most cluster models, the binary injection procedure is straightforward: a normal model is generated, with some stars bearing the mass of both components of a binary. The binaries are then split with internal positions and velocities suiting the semi-major axis and eccentricity.

This cannot be directly applied to Hubble-Lemaître models, as the star coordinates are not generated on the spot from a known distribution function, they are the product of the expansion. The binaries cannot be introduced into the initial uniform sphere, as such specific dynamical environment could have unexpected effects on the injected population, as could the expansion. The idea is then to introduce the fused binaries in the uniform sphere, let the expansion happen until apex, *then* split the binaries.

However, the number of spontaneous binaries is function of the total number of stars in the system, and introducing fused binaries lowers the effective number of spontaneous binaries. The population we injected in the uniform sphere is no longer appropriate to the current distribution of spontaneous. Moreover, many spontaneous binaries formed with one or two components being to-be-split fused binaries. Splitting the pairs will destroy them, further altering the spontaneous distribution.

Actually, the picture is even more complex if one looks at the binary fractions in several primary-mass bins. A given primary star with a mass falling in the bin i , when merged with its secondary for the expansion, might fall into the bin $i + 1$ and participate to the binary fraction in this bin. To converge towards a final population consistent with observations, we need to take into account the effects of injection, inter-bin transfers and splitting.

B.1 "Theoretical" population

Let us consider N_{bin} primary mass bins $[m_i; m_{i+1}]$. We label *theoretical* binary fraction f_i^{th} the observed binary fraction in each of those bins. It is expressed:

$$f_i^{th} = \frac{n_i^{th}}{N_i^{s,th} + n_i^{th}}. \quad (\text{B.1})$$

with n_i^{th} the theoretical number of binaries with a primary mass in the i th bin and $N_i^{s,th}$ the theoretical number of single stars falling into the i th bin. Given a total number of stars N , these

have unique values as f_i^{th} values are fixed. To inject an appropriate compensating population, we aim at obtaining n_i^{th} binaries in each bins after splitting. To obtain these values is not straightforward, as though f_i^{th} is known, $N_i^{s,th}$ depends on how much of the N_i stars in the i th bins are part of a binary, be it as a primary (n_i^{th}) or a secondary, which depends on the number of binaries in all bins superiors or equal to i , as they cannot be secondary to a lighter star.

We express $n_{i,j}^{th}$ the number of theoretical binaries with a primary in mass bin i and a secondary in mass bin j , as the number of primaries in i times the proportion of stars available to be secondaries in bin j compared to all other possible bins $k \leq i$, considering full random pairing. The available secondaries in j are simply $N_j - n_j^{th}$, and $n_{i,j}^{th}$ writes

$$n_{i,j}^{th} = n_i^{th} \times \frac{N_j - n_j^{th}}{\sum_{k \leq i} (N_k - n_k^{th})} \quad (\text{B.2})$$

We can now write the theoretical number of single stars in bin i as the total number of stars in said bin N_i minus

- two times the number of binaries with primary *and* secondary in i , as this removes two single stars;
- the number of binaries with a primary in i and a secondary in $j < i$;
- the number of binaries with a primary in $j > i$ and a secondary in i ;

which writes

$$N_i^{s,th} = N_i - 2n_{i,i}^{th} - \sum_{j < i} n_{i,j}^{th} - \sum_{j > i} n_{j,i}^{th} \quad (\text{B.3})$$

Substituting in Eq. B.1, we get

$$0 = n_i^{th} \left(1 - f_i^{th} \right) - f_i^{th} \left(N_i - 2n_{i,i}^{th} - \sum_{j < i} n_{i,j}^{th} - \sum_{j > i} n_{j,i}^{th} \right) \quad (\text{B.4})$$

which is a system of N_{bin} non linear equations with N_{bin} unknown variables n_i^{th} . It can be numerically solved to obtain the appropriate number of binaries with primaries in each bins to have a system exhibiting the theoretical binary fraction distribution.

B.2 Injected and effective population

We consider a minimum mass of $0.1M_\odot$, a maximum mass of $30M_\odot$ and a total number of logarithmic mass bins $N_{bin} = 10$. This gives a bin width of $\simeq 0.24 < \log(2)$, meaning that the sum of two masses from the same bin systematically falls in the next bin¹. With this in mind, we turn to the number of effective stars. As we inject binaries before the expansion as single objects, to be later split, the expansion happens with an effective total number of stars $\tilde{N} = N - n^{in}$ with n^{in} the total number of injected binaries. On a single bin, n_i^{in} expresses the number of injected binaries with a primary in i . As in previous section, we define the number of injected binaries with a primary in mass bin i and a secondary in mass bin j as:

$$n_{i,j}^{in} = n_i^{in} \times \frac{N_j - n_j^{in}}{\sum_{k \leq i} (N_k - n_k^{in})} \quad (\text{B.5})$$

With this, we can express the number of effective stars in each bins (this number counts fused binaries as single stars) as the total number of stars in i , N_i ,

¹The smallest possible outcome, the lowest mass in the bin paired with itself, still falls in the next bin.

-
- minus two times the number of injected binaries with both primaries and secondaries in i , as the merged object changes bins;
 - minus the number of binaries with a secondary in i and a primary in $j > i$, as the merged object cannot be in bin i ;
 - plus the number of injected binaries with both primaries and secondaries in $i - 1$, as the merged objects from the lower bins count as single stars in the present bin.

The number of injected binaries with a primary in i and secondary in $j < i$ has no effect on \tilde{N}_i as the merged object still falls into i . The expression writes

$$\tilde{N}_i = N_i - 2n_{i,i}^{in} - \sum_{j>i} n_{j,i}^{in} + n_{i-1,i-1}^{in} \quad (\text{B.6})$$

This effective stellar population will experience the Hubble-Lemaître expansion and form a spontaneous binary population. The spontaneous binary fraction f_i^{sp} was obtained from several Hubble-Lemaître fragmentation runs and did not significantly vary with N or H_0 . The presence of fused binaries slightly modifies the mass function of the system but we assume this does not affect the value of f_i^{sp} . We can write

$$f_i^{sp} = \frac{\tilde{n}_i^{sp}}{\tilde{N}_i^s + \tilde{n}_i^{sp}}. \quad (\text{B.7})$$

with \tilde{n}_i^{sp} the number of spontaneous binaries with a primary mass in i and \tilde{N}_i^s the number of single stars in i , both in the effective population, in which a fused binary count as one star. Following previous notations, we write the number of spontaneous binaries with a primary in i and secondary in j as

$$\tilde{n}_{i,j}^{sp} = \tilde{n}_i^{in} \times \frac{\tilde{N}_j - \tilde{n}_j^{sp}}{\sum_{k \leq i} (\tilde{N}_k - \tilde{n}_k^{sp})} \quad (\text{B.8})$$

and the number of single stars in the effective population as

$$\tilde{N}_i^s = \tilde{N}_i - 2\tilde{n}_{i,i}^{sp} - \sum_{j < i} \tilde{n}_{i,j}^{sp} - \sum_{j > i} \tilde{n}_{j,i}^{sp}. \quad (\text{B.9})$$

Substituting in Eq. B.7, we get

$$0 = \tilde{n}_i^{sp} (1 - f_i^{sp}) - f_i^{sp} \left(\tilde{N}_i - 2\tilde{n}_{i,i}^{sp} - \sum_{j < i} \tilde{n}_{i,j}^{sp} - \sum_{j > i} \tilde{n}_{j,i}^{sp} \right) \quad (\text{B.10})$$

B.3 Stable spontaneous

Some spontaneous binaries have one or two components that are fused binaries, we consider they do not survive splitting, as the algorithm will no longer register a bound pair. This can produce triple or quadruple hierarchical systems if the spontaneous pair semi-major axis is sufficiently larger than the one(s) from the fused binary component(s), but we do not consider them here, the algorithm will only detect the inner pairs.

Of the spontaneous binaries that arose in the effective population, \tilde{n}_i^{sp} , only those without fused binaries as components survive. We assume this is a necessary and sufficient condition for survival. We can obtain the number of *stable* spontaneous binaries with a primary in i and secondary in j by multiplying the number of spontaneous binaries $\tilde{n}_{i,j}^{sp}$ by the proportions of

effective stars in i and j that are *not* fused binaries. Fused binaries in a given bin k are the ones with primary and secondary both in $k - 1$ and all binaries with a primary in k and a secondary in any $l < k$. This writes

$$\tilde{n}_{i,j}^{sp,stable} = \tilde{n}_{i,j}^{sp} \times \left(\frac{\tilde{N}_i - \tilde{n}_{i-1,i-1}^{sp} - \sum_{k < i} \tilde{n}_{i,k}^{sp}}{\tilde{N}_i} \right) \times \left(\frac{\tilde{N}_j - \tilde{n}_{j-1,j-1}^{sp} - \sum_{k < j} \tilde{n}_{j,k}^{sp}}{\tilde{N}_j} \right). \quad (\text{B.11})$$

Which translates, when talking about all stable spontaneous binaries with the primary in i , as

$$\tilde{n}_i^{sp,stable} = \sum_{j \leq i} \tilde{n}_{i,j}^{sp,stable} \quad (\text{B.12})$$

We assume any injected binary survives when split, regardless of their final semi-major axis and the density of their environment, we will handle this later and it has no bearing on the present calculations. We can then finally writes the number of total surviving binaries

Finally, we can write the number of surviving binaries in the system, both from the injected and stable spontaneous populations, and equate it to the target theoretical number so the system follows the theoretical binary fraction distribution:

$$n_i^{th} = n_i^{in} + \tilde{n}_i^{sp,stable}. \quad (\text{B.13})$$

Since n_i^{th} is known from section B.1, we have two sets of N_{bin} unknown values, n_i^{in} and \tilde{n}_i^{sp} , and two sets of N_{bin} non-linear equations, Eq. B.10 and Eq. B.13. This can be numerically solved to obtain the values of n_i^{in} .

B.4 Random pairing

List of Figures

1	(a): depiction of the Ptolemaic geocentric system, the equant is not shown. (b): Copernicus illustration of his own heliocentric system, from <i>De revolutionibus</i>	2
2	(a) and (b): drawings by the hand of Galileo of his astronomical observations.	3
3	(a) a supposedly descendant from Newton's apple tree in Cambridge. The drawing in (b) illustrates the common mechanics of cannonballs and satellites.	4
4	The observer and the theorist, a century apart.	6
5	The Siemens 2002, seen here on (a) at the computer museum in Kiel, could perform 2000 operations a second. The Hydra cluster, on (b), at the Max Planck Computing & Data Facility in Garching is made of 83,000 cores and 676 GPUs for a total of 10^{15} operations per seconds, a billion millions.	7
6	The evolution of the number of particles in N-body simulations. Solid line shows the Moore law. The figure was taken from Bédorf & Portegies Zwart (2012).	8
1.1	Composite picture (visible and infrared) of the merging Antennae galaxies (NGC 4038 and 4039). Very active star forming regions are seen in infrared as the gas is heated by newborn stars. Bright blue points are the hot OB stars found in the numerous Young Massive Clusters (YMCs) in the system. <i>Credits: NASA, ESA, and B. Whitmore (STScI)</i>	10
1.2	Examples of various types of cluster. White bars at the lower left of each pictures show 1 parsec length scale. The dust present in the young Pleiades open cluster scatters starlight, producing this blue haze. The globular cluster ω Centauri contains one million stars and is the largest known star cluster in the Milky Way. <i>Credits: NASA, ESA, AURA/Caltech; ESO/INAF-VST/OmegaCAM</i>	12
1.3	Examples of various types of cluster. White bars show 1pc. The young massive cluster R136 is surrounded by its primordial nebula while the embedded cluster NGC 1333 is still inside it. (b) is a composite of visible and infra-red light. <i>Credits: NASA, ESA, F. Paresce; T. Rector (U. Alaska Anchorage), H. Schweiker</i>	13
1.4	Radius-Mass Diagram for Milky Way clusters. Blue dots are open clusters, red dots Globular clusters and purple squares show Young Massive Clusters. Dashed lines show constant density within half-mass radius $\rho_h = 3M/8\pi r_{hm}^3$ and dotted lines show constant half-mass relaxation time. The plot was taken from the review Portegies Zwart, McMillan & Gieles (2010).	14
1.5	Comparison of King and Plummer models density as a function of radius, for similar core radiiuses.	17
1.6	Visible light and infrared view of a part of the Orion star forming complex. Horsehead nebula is visible on the right, as well as the very bright star Alnitak, part of the Orion belt. NGC 2071 and 2068 are visible on the left. Pink infrared coloring shows radiation from very bright young massive stars forming in the cloud. Colder filaments are visible all around. White bar on lower right of visible shows 1 parsec. <i>Credits: Digitized Sky Survey; ESA/Herschel/PACS</i>	18

1.7	Stages of stellar birth. (a) is just cold molecular gas and contains no central source yet. (b) is more advanced, though hidden in visible light, its central protostar shines in infrared. The protostar in (c) is actively accreting its disk and produces jets. (d) is a pre main-sequence star, free from its envelope and surrounded by primordial gas. (e) is the mature stellar stage: the main sequence. <i>Credits: Kandori et al. (2005); NASA/JPL-Caltech/Evans,N; Burrows,C/HST-NASA; ESA/Hubble & NASA; DSS</i>	19
1.8	Herschel IR 70m observations of the Carina Nebula, with YSOs as red points and diamonds. Cyan crosses show OB stars. Both the gas and prestellar objects follow a substructured distribution. The figure was extracted from Gaczkowski et al. (2013).	20
1.9	(a): hydrodynamical simulation of wind-induced gas expulsion around a small cluster, the figure was extracted from Dale et al. (2013). (b) virial parameter of stellar clumps in a star forming hydrodynamical simulation, ignoring the potential of the gas to predict their post-expulsion fate. The solid line is the cumulated distribution of clumps over all snapshots; the shaded histogram shows the final distribution. The figure was extracted from Kruijssen et al. (2012).	21
1.10	Comparison of star formation hydrodynamical simulation from Bate (2012) (a) and Herschel infrared observations of the Aquila star forming complex, extracted from Könyves et al. (2010) (b). Gas column density is shown as levels of red and yellow on the left and as levels of blue and red on the right. The simulation spans 0.6 parsecs while the observations, with the distance estimate from the authors, span 7 parsecs. We inserted the simulation into the observation to compare the scales.	22
1.11	Representation of four methods to generate substructures. (a) is extracted from Kruijssen et al. (2012), constructed with data from Bonnell, Bate & Vine (2003), (b) is extracted from Fujii (2015). (c) and (d) were generated for this work.	24
2.1	Theoretical values of the apex time, at which the system stops expanding, as a function of initial HL parameter, which tunes the strength of the initial expansion.	33
2.2	Schematic illustration of a sinewave density perturbation (red line) applied to an uniform distribution of matter (blue dots) and the resulting distribution (red dots). The mode displayed here has $m = 10$ and its amplitude was exaggerated.	36
2.3	(a): growth of perturbation ξ_* over dimensionless time τ until the end of expansion at $\tau = 3.84$. An overdensity seeded with a wavelength λ_* begins its collisional evolution when ξ_* reaches $\frac{\lambda_*}{2}$. These regimes are illustrated for $\lambda_* = 0.04$ and $\lambda_* = 0.08$. The overdensities have to evolve collisionally for at least τ_{ms} to mass-segregate. This time-scale is also shown for each case. The blue case evolve collisionally for several τ_{ms} and will end up mass-segregated, while the red case visibly don't have time to segregate. Modes of large wavelength tend to produce less mass-segregated clumps. (b) for a given number of nodes m , a model on the right of the corresponding line (arrow for $m = 10$) will have mass-segregated overdensities at the end of the expansion, will on the left, the collisional evolution is too short for segregation to sets in. The red crosses show the minimum N below which the modes cannot be resolved.	39
3.1	Progressive fragmentation through the Hubble expansion. The left panel shows the initial uniform sphere; the middle panel, an intermediate step, slightly fragmented with a slowed down expansion; the right panel is the final stage, when the expansion has stopped and the fragmentation is fully developed. $N=10000$ particles were used in this N-body model, with $H_0 = 1.0$. Time and coordinates are in Hénon units.	42

3.2	Visualization of the StarFiddle API. Squared boxes are data storing classes while rounded boxes are modules.	44
3.3	Illustration of a Minimum Spanning Tree and its use to isolate subgroups, using a cutting length d_{cut}	46
3.4	Two different methods to identify the critical d_{cut} for clump detection. Both methods give the same value. For this 80k model, the value is 0.023 in Hénon units. The red linear fit on (b) was made on the linear portion with sufficient data points, discarding the seven further points departing from the tendency.	47
3.5	Example of detected clumps for three cutting length, 0.014 (top panel), 0.024 (middle panel), 0.034 (bottom panel), which were labeled A,B,C in Fig. 3.4a. A cube within a 80k particles fragmented model was extracted and projected. Empty circles are stars which do not belong to any clump, black circles are clump members, and blue squares are stars that are identified as a single large clump. Tick marks are spaced by 0.05 length units for a box size of 0.35 units.	47
3.6	Analytical and simulated apex times as a function of H_0	49
3.7	Clump mass function for several memberships and two H_0 . Masses in the top panels are in Hénon units, the x-axis was scaled with a factor 100 to get a percentage of the total mass of the system. Bottom panel masses are in physical units. In each panel, top sub-panel shows actual clump count in each bin (averaged over sampling), while bottom sub-panel normalize the count by the model membership.	50
3.8	Clump mass function (real mass) for several H_0 and two memberships.	51
3.9	Mass function of the clumps identified with the MST algorithm. The calculations all had $N = 15000$ stars, and we have averaged over 30 realisations for each configuration. The results for three stellar mass functions are displayed : a model with equal-mass stars (green dashed line) ; a Salpeter distribution function truncated at $20M_\odot$ (solid red line, left) ; a Salpeter distribution function truncated at $100M_\odot$ (solid red line, right). (a) The clumps mass function for equal-mass models shows a trend with mass roughly in agreement with an M^{-4} power-law. By comparison, the results for an Salpeter stellar distribution function truncated at $20M_\odot$ has a bell-shaped profile, with a peak around $M = 20.5M_\odot$; only the tail-end shows marginal agreement with an $\propto M^{-1.7}$ power-law (dotted line on the figure) ; (b) another Salpeter distribution function but with the upper-mass truncation set at $100M_\odot$. The tail at large clump mass is now much flatter, with a slope $\approx M^{-1}$, (dotted line on the figure as well). The bins used had constant logarithmic mass intervals.	53
3.10	(a) Distribution of the one-dimensional velocity field for the whole cluster as the thick solid black line, in the simulation labelled as R40h20 at the apex time ($H=0$). The red dashed distribution matches clump members and thin solid blue the field particles. (b) The distribution for three different values of H_0 : when $H_0 = 0$, the distribution is a Dirac- δ around $v = 0$. The central distribution broadens as H_0 increases to 0.3 and 1. Observe the exponential profiles at large $ v $. Velocities are in H.u	54
3.11	Top panel : Mass function of all stars belonging to a detected clump (solid red). The expectation drawn from a Salpeter distribution function for the same total number of stars in dotted black ; the grey shade are 1σ uncertainties. The green dashed line is the distribution for the full cluster. Bottom panel : same data normalised to the Salpeter expectation.	57

3.12	(a) Mass of the heavier star in each clump, shown as white dots, as a function of clump mass. The color map shows the likelihood for the maximum mass if all clump members were sampled from a Salpeter IMF ; the orange crest gives the maximum likelihood. The red dashed line shows the relation $m_{clump} = 2m_{max}$ (see. section 3.2.2). The data was taken from the R40h100 run. (b) is a similar distribution from Weidner, Kroupa & Pflamm-Altenburg (2013), built with data about young embedded star clusters from Weidner, Kroupa & Bonnell (2010). The black frame notes the range of masses displayed in (a).	58
3.13	Illustration of the radial ranking method. Stars marked 1,2 and 3 are the first, second and third most massive stars in the clump. Distances to the geometrical center are computed then sorted. The position in the sorted list is converted to a number, the radial rank.	59
3.14	Histograms of radial ranking of first, second and third most massive star in each clump for a model with $N = 40\,000$ stars (R40h100).	60
4.1	Distance to origin for 750 stars from run Ru20 (see Table 3.1). Red lines show the trajectory of stars that are considered ejected according to our criterion.	66
4.2	Half-mass radius as function of time for two systems undergoing collapse : a uniform-density sphere (thin red solid curve) and a clumpy Hubble model (thick blue solid curve). Half-mass radii are in H.u, as well as the time axis, where $t_{Hénon} = 1\text{unit} = 0.13\text{Myr}$. Dashed lines are the half-mass radii of the same systems for the same systems but including only the bound stars.	67
4.3	The ten-percentile mass radii (10% to 90%) as function of time. Radii and time axis are in H.u, with $t_{Hénon} = 1\text{unit} = 0.13\text{Myr}$. Left panels show the Uniform model and right panels show the Hubble fragmented models. Panels a and b show the evolution of the whole systems, while panels c and d shows the same radii computed for the bound stars only. Panel e shows the Uniform bound model (Ru20b) for which radius and time were rescaled to compensate the difference of initial kinetic energy (see text for details). Panel f shows the same information as panel d with smoothed data. 10% and 90% radii are labelled in the top right panel.	69
4.4	Half-mass radii of stars selected by mass as function of time. Each bin identified with 0-10%, 10-20% .. 90-100%, contains ten percent of the total system mass. The stars were sorted by mass in decreasing order, and used to fill each ten-percent mass bin in order. Hence the first ten-percentile contains the most massive stars, the next ten-percentile the second group of massive stars, and so on until the 90-percent bin which contains the least massive stars in the model and is the most populated. Half-mass radius and time are in H.u, with $t_{Hénon} = 1\text{ unit} = 0.13\text{Myr}$. Left panels show the evolution of the Uniform model (Ru20, Ru20b) and right panels do the same for the Hubble model (Rh20, Rh20b). The organization of panels follows the same layout than figure 4.3 with a different factor for the rescaling of the uniform system.	71
5.1	(a) Hubble observation of the binary star Albireo, fifth brightest star in the Cygnus constellation. Albireo A, the red star, is a close binary system itself (not represented on (b) for simplicity). The pair has a period of 213 years and a semi-major axis $a \simeq 66$ AU.	78

5.2	(a) shows the observed distribution of period and semi-major axis observed in the field. Different hatchings show different observation techniques: horizontal lines show unobserved companions detected by the proper-motion acceleration of components, positively sloped lines show spectroscopic binaries, negatively sloped lines visual binaries, cross hatching show objects found with both, and vertical lines are objects with common proper motions. (b) was compiled from several surveys, detailed in Fig 4.? (to come later). Both figures were extracted from Raghavan et al. (2010).	79
5.3	(a): total binary fraction over time in a subvirial fractal system. Corresponding models for the solid, dashed, dot-dashed and dotted are respectively 100% initial binary fraction with log-normal distribution, 100% fraction with Kroupa distribution, field-like fraction with log-normal distribution and field and 75% fraction with log-normal distribution. (b): 100% initial binary fraction with an initial log-normal distribution (open histogram) and the evolved distribution after 1Myr (hashed histogram). Solid red and dashed blue lines are fits for, respectively, the G-dwarf and M-dwarf populations. Both figures were extracted from Parker, Goodwin & Allison (2011).	80
6.1	Illustration of a kd-tree for a random two-dimensional distribution (blue dots).	84
6.2	Illustration of the density threshold method. The central blue stars and the red bound neighbour describe a two-body orbit shown on the figure while the green bar indicates the major-axis of the system. This defines the binary density, green sphere, while the local density is defined with the grey stars, the other neighbours. Here, N_{nb} was set to 7.	85
6.3	Semi-major axis histograms for various value of the density ratio D at $t=0$ and 10 H.u for a 10k star King model and a binary fraction $f_b = 0.3$. The injected log-normal population is shown as a black solid line.	85
6.4	Visualization of the wide ($a > 1000$ AU) binary population in a King model over time. Large upper panel show the evolution of all binaries detected for a density ratio $D = 2000$, ordered by time of first detection. Each lower sub-panel show the new binaries detected with the new, lower, value of D compared to the previous one.	87
6.5	Observational data of binary fractions (dots with uncertainties) as a function of primary mass. The data are taken from (in increasing primary mass): Close et al. (2003); Basri & Reiners (2006); Fischer & Marcy (1992); Ward-Duong et al. (2015); Raghavan et al. (2010); Patience et al. (2002); Preibisch et al. (1999); Mason et al. (1998). The red line is a best-fit linear relation. The thin curves and $1-\sigma$ dispersion shaded area are the results for a population of spontaneous binaries obtained from HL models.	88
6.6	Distribution of semi-majors axis of spontaneous binary populations for two values of stellar number density. Green curve show the canonic separation distribution from Raghavan et al. (2010).	89
6.7	Binary fraction as a function of primary mass. The results displayed are the average of twenty realisations for 20k particles models; the shade indicates $1-\sigma$ deviations. Short semi-major axis binaries were injected to complete the spontaneous population (compare with Fig ??).	91
6.8	Distributions of binary separations for the completion of a population in low and high density models. Spontaneous binaries before splitting are shown in short-dashed red, the population injected in the system in long-dashed blue and the resulting measured distribution in the completed system in green. The observational separation distribution from Raghavan et al. (2010) is shown as a grey area, taking into account Poisson dispersion.	92

7.1	Left panel: spatial distribution of a Hubble-Lemaître fragmented model. Right panel: evolution of the half-mass radius over time. The times labelled as t_0 to t_3 are the system configurations used in §4 for analysis.	94
7.2	Top panels: total binary fraction over time for different cluster memberships. Lower panels: total number of binary over time compared to initial number in each system, in percentage. The vertical dashed line indicates the time of deepest collapse.	95
7.3	The data is from low density models. Top panels show the binary fraction in logarithmic bins for the primary masses. Dotted line show the linear fit to observations shown in Fig. 6.5. In bottom panels, the number of binaries in each primary mass bin is shown as a percentage of the initial number ($t=0$). The 100% value is shown as a horizontal dashed line.	97
7.4	The data from high density models. Same key as Fig. 7.3.	97
7.5	Histograms of semi-major axes for the binary population at four different times and for four different cluster membership. The dotted black line shows the distribution of $N = 1.5k$ models at $t = 0$ as a reference for the initial distributions. High density models are in the top row, while low density models are in the bottom row. The reference times are taken from Fig. 7.1.	98
7.6	Top panels: histogram of semi-major axis at four different times for the $N = 20k$ models. Bottom panels shows the erosion factor, the ratio between the sizes of the initial binary population and the one at a given time, in each primary mass bin.	99
7.7	Left panels: Total binary mass (top) and distance to center of the cluster (bottom) versus the semi-major axis for binaries tighter than 1AU at the end of the simulation. Right panels: same layout for binaries wider than 10^4 AU. The greyed area in the top panels shows the 90% probability range of a binary total mass from random pairing given the present IMF. The red dashed line in the top left panel shows the relation for constant $v_\infty^2 \sigma_{coll} \equiv \sigma_0$; it is bounded by two dotted curves that have $10\sigma_0$ (above) and $0.1\sigma_0$ (below). The horizontal dotted line in the bottom panel indicates the boundary between the ejecta (distance to center $> 10\text{pc}$) and the central system. Open circles are binaries which already existed at $t=0$. The data is from 10 simulations of $N = 20k$ stars with initial mean density of $6/\text{pc}^3$	102
7.8	Evolution of individual binaries semi-major axis and distance to center over time in the low density 20k particles models. The vertical dashed line marks the moment of deepest collapse $t \simeq (t_1 + t_2)/2$	105
8.1	Cluster formation in a hydrodynamical simulation of the Antennae galaxies. The colormap indicates gas densities and newly formed stars are shown as black dots. Two epochs are shown, outlining the erasure of substructure. The figure was extracted from Renaud, Bournaud & Duc (2015)	110
8.2	Time taken to reach the Base of the Giant Branch (BGB) as a function of initial stellar mass, for two metallicities, $Z = 0.0001$ and $Z = 0.03$. The figure was extracted from Hurley, Pols & Tout (2000)	111
A.1	Illustration of block time steps on 4 particles. Particles get their positions updated for each arrow symbol, common time steps are shown as vertical dotted lines. Figure from NB6++ User Manual.	126
A.2	Summary of the Hermite scheme starting from known positions and velocities at t_0 to obtain 5th order values at t	127

List of Tables

2.1	Summary of main variables.	34
3.1	Summary of fragmentation models and their characteristics. These simulations, performed with NBODY6, started from an uniform sphere and were stopped at the apex time, t_a , when the expansion halts. The third column shows the number of independent computations for each model. Stars are drawn from an Salpeter distribution with truncation values shown in the fourth column. All mass ranges preserve an average stellar mass of $1M_\odot$. Models that stops at 40 H.u starts from already fragmented configuration. The RunsHN runs are detailed in the two lower tables.	48
4.1	Values of half-mass radii and their ratio to that of the most massive stars. The mass categories are labelled X%-X+10%, with the percent symbol ommitted for brevity. The results are for the rescaled bound uniform model (rescaled Ru20b) and the bound Hubble model (Rh20b), after the collapse, and before dynamical mass segregation sets in.	72
7.1	Summary of simulations. Starting from an HL fragmented configuration, a binary population was injected to complete the spontaneous binaries, reaching an overall binary fraction of 0.42. Densities withing half-mass radius are shown at t=0 and time of deepest collapse.	94